

Molecular dynamics simulations of nucleation and phase transition in halide perovskites

Présentée le 8 avril 2022

Faculté des sciences de base
Laboratoire de chimie et biochimie computationnelles
Programme doctoral en chimie et génie chimique

pour l'obtention du grade de Docteur ès Sciences

par

Paramvir AHLAWAT

Acceptée sur proposition du jury

Prof. B. Smit, président du jury
Prof. U. Röthlisberger, directrice de thèse
Prof. C. Vega de las Heras, rapporteur
Prof. M. Salvalaglio, rapporteur
Prof. M. Ceriotti, rapporteur

Take up one idea. Make that one idea your life - think of it, dream of it, live on that idea. Let the brain, muscles, nerves, every part of your body, be full of that idea, and just leave every other idea alone. This is the way to success. — Swami Vivekanand

Arise, awake and stop not till the goal is reached. — Swami Vivekanand

To my parents and grandmother

Acknowledgements

I thank Professors Michele Parrinello and Michael Graetzel for their continuous encouragement and support during my Ph.D. I would like to thank Professor Ursula Rothlisberger for this opportunity. I thank Professors Anders Hagfeldt, Frank Schreiber, Lyndon Emsley, Jin Young Kim, Dong Suk Kim and Shaik M. Zakeeruddin for the crucial collaborative help in my Ph.D. research.

I thank my friends and collaborators Pablo Piaggi, Michele Invernizzi, Haiyang Niu, Omar Valsson, Claudio Perego, Luigi Bonati, M. Ibrahim Dar, Alexander Hinderhofer, Haizhou Lu, Jaeki Jeong, Amita Ummadisingu, Jovana Milic, Hong Zhang, Aditya Mishra, Essa A. Alharbi, Matthaues Babler, Vladimir Rybkin, Zoran Bjelobrk, Swarnendu Bhattacharyya, Polydefkis Diamantis, Viacheslav Bolnykh, Daniele Narzi, Michael Hope, Dominik Kubicki, Minjin Kim, Li Hong and Andrej Antalík for stimulating discussions and invaluable support. I thank Daniela Wirz and Karin Pasche for the kind help over the years.

I want to express my gratitude to my parents, brother, and Anjali. Their tremendous understanding and encouragement helped me to overcome obstacles in the past few years.

I also want to acknowledge the financial support by the Swiss National Science Foundation through NCCR-MARVEL and NCCR-MUST.

Abstract

Perovskite solar cells have emerged as the most promising cheaper photovoltaic technology. Besides solar cells, halide perovskites have a wide range of applications due to their remarkable optoelectronic properties. Starting from $\sim 3.8\%$ in 2009, solar to the power conversion efficiency of perovskite solar cells is now $>25\%$, exceeding market leader polycrystalline silicon. These advancements are mainly due to the improvement in their manufacturing process targeted to make better morphology. To this objective, tens of thousands of experimental studies are conducted where a wide range of additives, compositions, and processing conditions are optimized based on a trial and error methodology. Although this approach increased the efficiency, however, perovskite electronics suffer from the problem of stability and reproducibility. Therefore, to industrialize highly efficient perovskite electronics, one needs to understand better and rationalize their fabrication process, i.e., crystallization of halide perovskites. In this thesis, I perform molecular simulations to understand the formation process of halide perovskites. First, I try to lay out the atomic details of the nucleation process of perovskite from the solution. I find that nucleation proceeds in a two-step manner where an intermediate phase forms before the emergence of perovskite crystals from the solution. I observe that monovalent cations can play an essential role in the nucleation process. On this information, simulation-driven experiments are performed from experimental collaborators to demonstrate that the grain size and crystallinity can be tuned by only varying the concentration of monovalent cations in solution. I also attempted to study the effects of different solvents and pseudo-halide additives used to make high-efficiency solar cells. I calculated that by modulating the solute-solvent interactions, one could minimize raw material losses during the coating process. In comparison, pseudo-halide additives are found to passivate the ionic defects and may slow down the growth process that helps to improve the final morphology. Second, I study the solid-solid phase transition in the popular two-step process. I discover a new path to the low-temperature formation of highly efficient metastable cubic phase of formamidinium lead iodide perovskite. I first validate my simulations with *in-situ* experiments performed by experimental collaborators. Then simulations are employed to design a practical methodology to successfully make thin films of phase pure cubic formamidinium lead iodide at lower temperatures. Moreover, I study the intrinsic stability of this material. I calculate the energy barrier between the metastable photo-active phase and its photo-inactive thermodynamically stable hexagonal phase. I find that once formed; the photo-active phase might be

kinetically stable. Additionally, I identify new polymorphs (perovskitoids) of halide perovskites and also study the structural insights of low-dimensional halide perovskites. Overall, I present a fundamental understanding of the crystallization of perovskites which is helpful to design better experiments to make high efficiency and stable perovskite electronics.

Key words: Halide perovskites, Nucleation, Molecular dynamics simulations, Enhanced sampling, Solid-solid phase transition, Perovskite solar cell

Contents

Acknowledgements	i
Abstract	iii
List of figures	vii
List of tables	xvii
1 Introduction	1
2 Crystallization in the single-step process	7
2.1 Atomistic mechanism	7
2.1.1 Introduction	7
2.1.2 Results	8
2.1.3 Experimental results and discussion	17
2.1.4 Conclusions	20
2.1.5 Methods	20
2.1.6 Clustering at the first stage	22
2.1.7 Edge-sharing octahedra	23
2.1.8 Perovskite corner-sharing octahedra	24
2.1.9 Experimental Methods	25
2.2 Effect of different solvents	26
2.2.1 Introduction	26
2.2.2 Results	26
2.2.3 Methods	28
2.3 Effect of pseudo-halides	30
2.3.1 Introduction	30
2.3.2 Results	30
2.3.3 Methods	32
3 Phase transitions in the two-step process	37
3.1 Sequential deposition	37
3.1.1 Introduction	38
3.1.2 WTmetaD simulations	39
3.1.3 Experiments	45

3.1.4	Thin-film experiments on formation of phase-pure α -FAPbI ₃	47
3.1.5	Discussion	48
3.1.6	Conclusions	49
3.1.7	Methods	49
3.2	Two-step phase transition from δ -FAPbI ₃ to α -FAPbI ₃ via vapor treatment . . .	52
3.2.1	Introduction	52
3.2.2	Results	53
3.2.3	Kinetic stability of α -FAPbI ₃	56
3.2.4	Methods	58
4	Structure prediction of low-dimensional perovskites	61
4.1	Introduction	62
4.2	Structure prediction with constraints	62
4.3	Guanine-based low-dimensional halide perovskite	63
4.3.1	Proton transfer	63
4.4	1,4-phenylenedimethan ammonium (PDMA)	65
4.5	(1-adamantyl)methan ammonium (A) and 1-adamantyl ammonium (A')	67
4.6	Mixture of 2-phenylethyl ammonium and 2-(perfluorophenyl)ethyl ammonium	69
5	General Conclusions	73
A	An appendix	77
A.1	Single-step process	78
A.2	Two-step process	85
A.3	Quasi-2D perovskites	85
A.3.1	Guanine	85
A.3.2	PDMA	90
A.3.3	(1-adamantyl)methan ammonium (A) & 1-adamantyl ammonium (A') . .	91
A.3.4	PEA and FEA mixtures	92
	Bibliography	111
	Curriculum Vitae	113

List of Figures

2.1	Full nucleation pathway illustrated with representative snapshots. Pb-I complexes are shown as golden and blue polyhedra with Pb^{2+} in the center and I^- in the corners. Free I^- is shown as pink spheres. Crystalline MA^+ ions are shown in green. (a) initial solution of MA^+ , I^- and Pb^{2+} in GBL. MA^+ and GBL are shown semi-transparent to visualize the random distribution of Pb^{2+} and I^- in solution. (b) the initial cluster formation of Pb^{2+} and I^- surrounded by MA^+ ions. c) shows only edge-sharing $[\text{PbI}_6]^{4-}$ octahedra. (d) the first perovskite nucleus observed in the solution. (e) illustrate the growth of the initial nucleus. (f) the largest perovskite crystal in the simulations. All of the images were generated with VMD [119].	9
2.2	Illustration of the full nucleation pathway for a large simulation system-(C): Pb-I complexes are shown as green and blue polyhedra with Pb^{2+} in the center and I^- on the corners. I^- is shown as pink spheres. MA^+ ions are shown with ball and sticks in the initial homogeneous solutions and yellow balls in perovskite crystals. Snapshot (a) represents the initial solution of MA^+ , I^- and Pb^{2+} in GBL. GBL molecules are respresented with balls and stick model and shown as semi-transparent. Snapshot (b) shows the intermediate edge-sharing chains of $[\text{PbI}_6]^{4-}$ octahedra. Images (c) and (d) are the perovskite crystals observed in the simulations. Image (d) is the side view of image (c). All the images of these snapshots are generated with VMD-1.9.2.[119]	10
2.3	Perovskite CV employed to drive the nucleation process. In order to guide the eye, the running average (over 1ns interval) of the CV is shown as a thick black line. The stages into which the simulation is divided for the purpose of analysis are shown with different colors (see text for details). Time on x-axis is WTmetaD time.	11
2.4	Analysis of the first stage in which cluster formation is observed. Top panel (a) displays the number of $[\text{PbI}_6]^{4-}$ complexes divided by the total number of Pb^{2+} ions in our simulation. The bottom panel (b) shows the size of the largest cluster as a function of simulation time. Here we represent the size of the cluster as the fraction of Pb^{2+} ions in the cluster out of the total of Pb^{2+} ions in the simulation box.	12

- 2.5 **Analysis of the second stage with representative images.** Time evolution of edge-sharing and perovskite corner-sharing octahedra. Thick lines are the running average (over 1ns interval) of the data and are shown in order to guide the eye. (a) the initial cluster at ~ 140 ns. (b) the configuration of the part of the cluster that evolves into the first perovskite nucleus at ~ 161 ns. (c) represents the evolution of the same cluster at ~ 175 ns. (d) the first perovskite nucleus in our simulation at ~ 180 ns. Time on x-axis is WTmetaD time 13
- 2.6 **Visualization of intermediate phases:** The picture in the middle represents the clusters of edge-sharing octahedra in our simulation (A) at ~ 161 ns. Pb-I complexes are shown as blue octahedra with Pb^{2+} in the middle and I^- on corners. I^- is shown as pink spheres. Individually arranged structures within edge-sharing clusters are displayed separately. All the images of these snapshots are generated with VMD-1.9.2 [119] 14
- 2.7 Left panel (a) shows the configuration of edge-sharing octahedra at ~ 161 ns. Here we have excluded MA^+ ions and solvent molecules. Pb-I geometry is shown with blue octahedra with Pb^{2+} in the center and I^- on the corners. I^- is shown in pink spheres. Right panel (b) shows the configuration of the same species at ~ 327 ns. Pb-I geometry is shown with golden octahedra with Pb^{2+} in the center and I^- on the corners. 15
- 2.8 **Diffusion analysis of the subset of MA^+ ions.** Time evolution of (a) mean square displacement and (b) diffusion coefficient of MA^+ ions that take part in the formation of the first perovskite nucleus. 16
- 2.9 **Analysis of the growth.** Left panel shows the change in number density of MA^+ and Pb^{2+} ions around the center of the first perovskite nucleus. Right panel displays the temporal evolution of perovskite corner-sharing octahedra. The thick black line in the right panel is the running average (over 1ns interval) of the data and is shown to guide the eye. Time on x-axis is WTmetaD time. 17
- 2.10 **Morphological characterization of thin films:** (a) shows the top view SEM micrographs acquired from 0.75M MAPbI_3 films with 1:1 ratio of PbI_2 and MAI in the precursor solution. (b) shows the top view SEM micrographs acquired from the addition of extra 0.25 moles of MAI and (c) displays the top view SEM micrographs acquired from the addition of extra 0.50 moles of MAI. Left panel and right panel in (b) and (c) are the low and high magnification data from the SEM micrographs and also indicated in the respective figures. Figures (d), (e) and (f) show the grain size distribution of the final perovskite thin films prepared from solution-(A), solution-(B) and solution-(C) respectively. Further details are provided in the Methods section. We majorly considered large-sized grains for histograms owing to the presence of polydisperse grains. 18

- 2.11 **Experimental results and analysis of homogeneous nucleation:** Figure (a) shows the crystallisation of MAPI crystals in three different vials with three different concentrations of MAI in each vial. The respective concentrations in each vial are depicted in the picture itself. From left to right crystals grown in test tubes display the distinct black color of MAPI perovskite structure. Figure (b) displays the crystal of MAPI in GBL from simulations at the same experimental conditions of 1M concentration and 170°C. Pb-I octahedra are shown in blue color. MA⁺ are shown as yellow spheres. I⁻ are represented with pink spheres. 19
- 2.12 **Perovskite corner-sharing octahedra.** The two snapshots (a) and (b) on the left shows the configurations of perovskite corner-sharing octahedra. The picture (c) on the right is the histogram of Pb-I-Pb angles in the cubic perovskite structure of MAPI. 24
- 2.13 **Prototypical tetracoordinated Pb²⁺ clusters with different solvents:**(a) DMSO, (b) DME, (c) THF, (d) mixtures of DMSO and THF, and (e) mixtures of DME, DMSO and THF. All the atoms are labeled with their element symbols. All species are shown with balls and sticks representations. 27
- 2.14 **Solvent-solute interactions:** Average binding energies of Pb²⁺ ions with solvents and their mixtures (evaluated on the tetracoordinated complexes shown in **Fig. 2.13**). b-c *Ab initio* MD simulations of perovskites precursors in (b) DMSO and (c) THF/DMSO mixture after ~15 ps. All species are shown with balls and sticks representations. Pb ions are shown with golden color, I with pink color, Cs with greenish-blue, Br with orange, C with light blue, N with dark blue, O with red, S with yellow and H atoms with white color. In the (b) and (c) panels, lead coordination polyhedra are shown within a 3.6 Å cutoff. 27
- 2.15 ***Ab-initio* MD of precursor solution:** (A) MD snapshot showing the coordination of Pb²⁺ ions with HCOO⁻ anions. To guide the eyes, we only highlight Pb²⁺ and HCOO⁻ ions. Rest of the ions and solvent molecules are shown with transparent color. All ions are shown with balls and sticks representation. Pb²⁺ ions are shown with yellow balls, oxygen with red balls, carbon with light blue, nitrogen with dark blue, sulfur with light yellow and hydrogen atoms are represented with white balls. (B) The radial distribution function g(r) between the oxygen atoms of HCOO⁻ around Pb²⁺ over the full *ab-initio* MD trajectory of ~11 ps. 30
- 2.16 ***Ab-initio* MD of formate anions on the surface:**(a) Initial configuration with surface iodide replaced by formate anions. All ions are shown with balls and sticks representation. Pb²⁺ ions are shown with yellow balls, iodides with light pink, oxygen with red, carbon with light blue, nitrogen with dark blue and hydrogen atoms are represented with white balls. (b) The top view of the surface atoms on the Pb²⁺ terminated side. (c) The top view of surface atoms on the FA⁺ terminated side. Pb²⁺-HCOO⁻ and FA⁺-HCOO⁻ bonding networks are illustrated with red colored bonds in (b) and with magenta colored bonds in (c). 31

2.17	Binding affinities: (a) Calculated structure illustrating the passivation of an I^- vacancy at the $FAPbI_3$ surface by a $HCOO^-$ anion. All chemical species are shown in balls and sticks representation. (b) The relative interaction strengths of different anions with the I^- vacancy at the surface.	32
3.1	Phase transition via intermediate phases: Images a and b show the intercalation process. Images (b) to (e) display the phase transition from quasi-2D intercalated structure (b) to perovskite phase of $MAPbI_3$ (e). Pb-I complexes are shown as golden polyhedra with Pb^{2+} in the center and I^- as dark orange balls on the corners. MA^+ cations are shown with balls and sticks with carbon as light blue, nitrogen as dark blue and hydrogens being white. Similar structures have been observed for other materials such as $MgSiO_3$, $CsIrO_3$, $AgTaS_3$, $NaMgF_3$, $MgGeO_3$, $UFeS_3$ [178].	39
3.2	Simulated XRD spectra of intercalated phase and PbI_2: Comparison of the first peak of powder diffraction patterns of DFT-D3 optimized PbI_2 and intercalated structure. We use VESTA software to calculate the powder diffraction patterns.	40
3.3	Free energy profile for smaller supercell: Free energy profile between intermediate phase and full perovskite structure for smaller supercell. The error bars show the standard error of the free energy difference at each CV value in the final free energy profile.	41
3.4	Free energy profile for larger supercell: Free energy profile between intermediate phase and full perovskite structure for larger supercell. The error bars show the standard error of the free energy difference at each CV value in the final free energy profile.	41
3.5	Structure factor for larger cell: Evolution of first peak of structure factor of Pb^{2+} ions (S_{Pb1}) with WtmetaD simulation at 370K. Inset is a zoom of S_{Pb1} for the first transition from quasi-2D to 3D.	42
3.6	Structure factor for smaller supercell: Here we show metadynamics time evolution of first peak of structure factor for Pb^{2+} ions with their corresponding observed structures. Pb-I complexes are shown as blue polyhedra with Pb^{2+} in the center and I^- on the corners. I^- is shown as pink spheres. To guide eyes, monovalent cations are represented with green spheres.	43
3.7	Different polymorphs: Pb-I complexes are shown as golden polyhedra with Pb^{2+} in the center and I^- on the corners. Free I^- is shown as pink spheres. MA^+ and FA^+ cations are shown with ball and sticks with carbon as light blue, nitrogen as dark blue and hydrogens being white.	43
3.8	Illustration of crystal structures from two-step $FAPbI_3$ simulations: Figure (a) is the crystal structure of PbI_2 (b) shows intercalated structure (c and d) are the crystal structures of $FAPbI_3$ perovskite oriented at 35° and 90° , respectively.	44
3.9	XRD spectra of $FAPbI_3$ samples at room temperature: Top panel is the XRD spectrum of PbI_2 deposited film and bottom panel shows the corresponding data after the FAI loaded onto PbI_2 at room temperature	45

- 3.10 **From edge-sharing to face-sharing:** This figure shows that removing FAI from the intercalated structure leads to the formation of face-sharing octahedra. Left figure is the DFT relaxed intercalated structures and right hand side shows the DFT relaxed structure after removal of one stoichiometric unit of FAI. 46
- 3.11 **Analysis of WTmetaD trajectories:** This figure shows the angle between 001 plane of PbI_2 and metadynamics trajectory of the formation of 100 plane α - FAPbI_3 46
- 3.12 **Thin-film experiments of sequential deposition of FAPbI_3 :** Figures (a) to (c) are the SEM images showing the surface topography and figures (d) to (e) are the corresponding XRD spectra of thin-films before and after conversion to FAPbI_3 48
- 3.13 **Calculated structure factor from Equation 3.1:** Debye structure factor of Pb^{2+} ions in cubic phase of MAPbI_3 . MA^+ have a similar profile due to the symmetry of the cubic phase. 50
- 3.14 **A schematics of experiment and simulations of phase transition from δ - FAPbI_3 to α - FAPbI_3** 53
- 3.15 **Simulation setup of classical MD:** A large slab of δ - FAPbI_3 with MA^+ and SCN^- on top. This image was generated with Visual Molecular Dynamics (VMD). Pb-I octahedra are shown with golden color with iodide as orange balls at the corners of the octahedra. FA^+ , MA^+ , and SCN^- ions are shown with balls and sticks representation. Nitrogen is dark blue, carbon is light blue, hydrogen is white, and sulfur is yellow. 53
- 3.16 **Top view of the adsorption of SCN^- ions on top of δ - FAPbI_3 :** (a) Top view of the simulations. (b) A zoomed-in version of a small part of the top view to clearly show the adsorption of SCN^- ions on top. 54
- 3.17 **MD simulations showing a structural conversion:** Representative snapshots from the MD simulations showing a structural conversion of (A) the initial face-sharing octahedra and (B) the corner-sharing octahedra. Pb-I octahedra are shown in green; iodide is shown as orange balls on corners. To highlight the structural transformation, red was chosen for octahedra on the interface. FA^+ and MA^+ ions are not shown for clarity. Selected SCN^- ions are shown as ball and stick representations: sulfur is yellow, carbon is light blue, and nitrogen is dark blue (the other SCN^- ions are not shown for clarity). 55
- 3.18 **Illustration of a possible phase transition path induced by SCN^- anions:**(a) δ -phase FAPbI_3 structure. The mixtures of δ and α -phases of FAPbI_3 with the increasing number of corner-sharing structures from (b) to (e). (f) α -phase FAPbI_3 structure. SCN^- ions are adsorbed on the top of the respective structures. Pb^{2+} octahedra are portrayed with light blue colour with iodide as pink balls on corners. FA^+ and SCN^- ions are represented with balls and sticks representation. All the images were generated with the VESTA software. 56

- 3.19 **Energy diagram along a transition from δ -FAPbI₃ and α -FAPbI₃:** Each point on the energy plot represent a different DFT optimized structure along the path. A Gaussian fit of these points is included as guide to the eyes. For better visualization of the pathway, we have illustrated some of the intermediate phases. Pb-I octahedra are represented with light green colour with iodide on corners with pink balls. FA⁺ cations are shown with ball and sticks representation. . . . 58
- 3.20 **Configuration for the δ -FAPbI₃ with SCN⁻ on top:** (a) The starting configuration (at t=0) and (b) the configuration at t = ~10 ps for the δ -FAPbI₃ with SCN⁻ on top. We show the dimensions of the supercell to display the empty space used to treat the SCN⁻ ions as vapor between periodic slabs. Pb²⁺ ions and octahedron are shown with blue colour with iodide as light pink balls. FA⁺ and SCN⁻ ions are shown with balls and sticks representation. 59
- 4.1 **Predicted structures:** Images (a) and (b) are front and side view of an initially estimated supercell for n=1. (c) and (d) show the front and side view of final structure. (e) and (f) illustrate the structure and hydrogen bonding of guanine molecules in the final structure. Lead (Pb²⁺) ions are shown with golden balls, iodide (I⁻) ions are displayed with pink spheres. Pb-I polyhedra are displayed in golden color. Guanine ions are illustrated with balls and sticks. 64
- 4.2 **Full pathway of proton transfer in n=1:** (a) shows the initial configuration. Image (b) is the snapshot where hydrogens are shared between guanine molecules. (c) and (d) are the zoomed imaged from (a) and (b) respectively. Snapshot (e) is the final optimized geometry and illustrate that hydrogens are transferred . . . 65
- 4.3 **Change in structure with increasing temperature:** Image on the left is the initial geometry, middle one is the intermediate phase and image on the right is the final relaxed structure. Lead (Pb²⁺) ions are shown with golden balls, iodide (I⁻) ions are displayed with pink spheres. Pb-I octahedra are displayed in golden color. Ligand B is illustrated with balls and sticks. The images are generated with VMD. 66
- 4.4 **Time dependent autocorrelation function of the unit C1-C5 vectors of ligand B:** Image (a) display the behavior of ACF at different temperatures from 200-400K for n=1 and (b) is the comparison between n=1 and n=2 at 300K. 67
- 4.5 **Time dependent autocorrelation function of the unit C3-C8 vectors of ligand A:** Image displays the behavior of ACF at different temperatures: 300K, 350K and 400K for n=1. 68
- 4.6 **Comparison of equilibrated structures for 2D perovskite (n=1) with ligand-A and ligand-A'.** Lead (Pb²⁺) ions are shown with golden balls, iodide (I⁻) ions are displayed with pink spheres. Pb-I octahedra are displayed in golden color. Ligand A and A' are illustrated with balls and sticks. The images are generated with VMD. 68

4.7	Trial structures of layered perovskites: Top panel shows the twisted and parallel relative orientations of the aromatic rings in adjacent layers. Bottom panel is a schematics of different possible arrangements (1–5) of PEA ⁺ and FEA ⁺ molecules on the two opposing lattices representing the spacer bilayer within the layered perovskite.	70
A.1	Illustration of the full nucleation pathway for simulation-(B): Pb-I complexes are shown as golden and blue polyhedra with Pb ²⁺ in the center and I ⁻ on the corners. I ⁻ is shown as pink spheres. MA ⁺ ions are shown with ball and sticks. Snapshot (a) represents the initial solution of MA ⁺ , I ⁻ and Pb ²⁺ in GBL. GBL molecules are respresented with ball and stick model and shown as semi-transparent to visualize the random distribution of Pb ²⁺ , I ⁻ and MA ⁺ in solution. Snapshot (b) represents the intermediate cluster formation of edge-sharing [PbI ₆] ⁴⁻ octahedra. Snapshot (c) shows the first perovskite nucleus observed in the solution. Snapshot (d) shows the largest perovskite crystal in this simulations. All the images of these snapshots are generated with VMD-1.9.2.[119]	78
A.2	Analysis of edge-sharing octahedra: Number of edge-sharing octahedra as a function of simulation time in simulation (A)	79
A.3	Top panel is the g(r) of Pb ²⁺ -Pb ²⁺ in MAPi cubic perovskite and bottom panel is the g(r) of Pb ²⁺ -Pb ²⁺ in crystalline PbI ₂	80
A.4	DFT relaxed slabs of FAPbI₃ with different anions adsorbed at the iodide vacancy site on the surface: (a) pure FAPbI ₃ slab structure with Pb-I terminated surface on top and FA-I terminated surface on bottom side, (b) front view of the Cl ⁻ passivated surface, (c) Br ⁻ passivated surface, (d) BF ₄ ⁻ passivated surface, (e) HCOO ⁻ passivated. (f) illustrates the iodide vacancy passivation with HCOO ⁻ . All chemical species are shown with balls and sticks representation. Pb ²⁺ ions are shown with the large brown coloured spheres, I ⁻ with violet, oxygen atoms with red, carbon atoms with dark brown, nitrogen atoms with light blue, Br ⁻ with reddish brown, Cl ⁻ with light green, boron atoms with dark green, fluorine atoms with yellow and hydrogen atoms are represented with white spheres.	81
A.5	DFT relaxed FAPbI₃ slab HCOO⁻ adsorbed at the iodide vacancy site on the Pb-I terminated surface. All chemical species are shown with balls and sticks representation. Pb ²⁺ ions are shown with the large brown coloured spheres, I ⁻ with violet, oxygen atoms with red, carbon atoms with dark brown, nitrogen atoms with light blue and hydrogen atoms are represented with white spheres.	82
A.6	DFT relaxed FAPbI₃ slab HCOO⁻ adsorbed at the iodide vacancy site on with FA-I terminated surface. All chemical species are shown with balls and sticks representation.	83

A.7	DFT relaxed slabs of FAPbI₃ with different anions on the surface: (a) pure FAPbI ₃ slab structure with FA-I termination on top and Pb-I termination on bottom side, (b) front view of the COOH ⁻ passivated surface, (c) side view of the COOH ⁻ passivated surface, (d) Cl ⁻ passivated surface, (e) Br ⁻ passivated and (f) BF ₄ ⁻ passivated surface.	84
A.8	Desorption energies of FA⁺ cations on different passivated surfaces.	84
A.9	Surface structures: A zoomed-in view of the final configuration of corner-sharing structures on the interface.	85
A.10	Structure trial 1: Images (a) and (b) are front and side view of initially estimated supercell for n=1. (c) illustrated the immediate structure after a few step after the start of classical MD simulations. (d) is the final structure. Lead (Pb ²⁺) ions are shown with golden balls, iodide (I ⁻) ions are displayed with pink spheres. Pb-I polyhedra are displayed in golden color. Guanine cations are illustrated with ball and sticks. Here we use the Gaussian optimized geometry of ligand.	86
A.11	Structure trial 2: Images (a) and (b) are front and side view of initially estimated supercell for n=2. (c) illustrated the immediate structure after a few step after the start of classical MD simulations. (d) is the final structure. Lead (Pb ²⁺) ions are shown with golden balls, iodide (I ⁻) ions are displayed with pink spheres. Pb-I polyhedra are displayed in golden color.	87
A.12	Structure trial 3: Images (a) and (b) are front and side view of initially estimated supercell for n=2. (c) illustrated the immediate structure after a few step after the start of classical MD simulations. (d) is the final structure. Lead (Pb ²⁺) ions are shown with golden balls, iodide (I ⁻) ions are displayed with pink spheres. Pb-I polyhedra are displayed in golden color. Guanine and formamidinium cations are illustrated with ball and sticks.	88
A.13	Predicted structure: (a) is the initially estimated supercell for n=2. (b) and (c) shows the finally optimized structure. Lead (Pb ²⁺) ions are shown with golden balls, iodide (I ⁻) ions are displayed with pink spheres. Pb-I polyhedra are displayed in golden color. Guanine and formamidinium cations are illustrated with ball and sticks.	88
A.14	DFT optimized structure for n=1: Images (a) and (b) are front and side view of structures extracted from classical MD simulations. (c) and (d) show the front and side view of DFT optimized structures. Lead (Pb ²⁺) ions are shown with golden balls, iodide (I ⁻) ions are displayed with pink spheres. Guanine ions are illustrated with ball and sticks.	89
A.15	DFT optimized structure for n=2: Images (a) and (b) are front and side view of structures extracted from classical MD simulations. (c) and (d) show the front and side view of DFT optimized structures. Lead (Pb ²⁺) ions are shown with golden balls, iodide (I ⁻) ions are displayed with pink spheres. Guanine and formamidinium ions are illustrated with ball and sticks.	89

- A.16 **Tautomers in DFT optimized structure for n=1:** Both molecules are illustrated with ball and sticks. Color coding of the balls is following: oxygen is red, carbons is greenish blue, nitrogens are dark blue and hydrogen are represented with white color smaller balls 90
- A.17 **Structrual analysis for ligand B:** (a) is the equilibrated geometry for n=1 (b) shows the arrangement of ligands between 2 layers. Image (c) highlights the T-shaped configuration in one of the layers in the 2D supercell. Ligand B is illustrated with balls and sticks. The images are generated with VMD. 90
- A.18 **Initial DJ structures with Ligand A:** Left panel shows the supercell for n=1 and right panel shows the initially build supercell for n=2. Lead (Pb^{2+}) ions are shown with golden balls, iodide (I^-) ions are displayed with pink spheres. Pb-I octahedra are displayed in golden color. Ligand A and formamidinium (FA^+) ions are illustrated with balls and sticks. The geometry for ligand A was obtained from DFT optimization with Gaussian software. Images are generated with VMD software. 91
- A.19 **Change in structure with increasing temperature:** Images (a) to (e) for n=1. Image (f) is the side view of image (e). Lead (Pb^{2+}) ions are shown with golden balls, iodide (I^-) ions are displayed with pink spheres. Pb-I octahedra are displayed in golden color. Ligand A is illustrated with balls and sticks. The images are generated with VMD. 91

List of Tables

2.1	Values for the switching functions used in S_P	22
4.1	DFT energy comparison of twisted and parallel structures for $(\text{FEA})_2\text{PbI}_4$, $(\text{PEA})_2\text{PbI}_4$, and configurations 1–5 of $(\text{PF})_2\text{PbI}_4$ ($\text{PF} = 1:1 \text{ PEA}^+:\text{FEA}^+$; shown in Figure 5 in the main text). The energy of the segregated model is the average of the lowest energy $(\text{FEA})_2\text{PbI}_4$ and $(\text{PEA})_2\text{PbI}_4$ structures.	71

1 Introduction

Hybrid organic-inorganic perovskites have the generic formula ABX_3 where A is the organic cation, i.e. methylammonium (MA^+), formamidinium (FA^+) or Cesiums (Cs^+), B is a metal cation such as Pb^{2+} or Sn^{2+} , and X is a halide anion I^- , Br^- or Cl^- . They are currently at the forefront of the materials' research with applications ranging from cheaper high-efficiency solar cells [1–7], light-emitting diodes [8–11], transistors [12, 13], photocatalysts [14–16], and photodetectors [17, 18]. These materials show remarkable optoelectronic properties including a highly tunable band gap, i.e., this family of compounds can absorb a wide range of the light spectrum, high charge carrier mobility, long charge carrier life times and small-exciton binding energy. Over the past decade, solar to power conversion efficiencies (PCEs) of perovskite solar cells (PSCs) have increased from 3.8% to 25.5% [19–21] surpassing the market leader polycrystalline silicon. The external quantum efficiency of perovskite light-emitting diodes (PLEDs) has reached to $\sim 23.4\%$ [22] which is comparable to the highest efficiencies of conventional III-V and II-VI quantum dot LEDs.

The meteoric rise of halide perovskites is also a result of simple manufacturing processes. High efficiency perovskite electronics PSCs and PLEDs are typically made via solution deposition techniques which are generally categorized into two types: single-step processes [3, 23–28] and two-step processes [29, 30]. In the single-step process, perovskite electronics are manufactured by mixing precursor salts of BX_2 (for example, PbI_2 , $PbBr_2$) and AX (for example, MAI, FAI, CsBr) in polar aprotic solvents on conducting substrates such as titanium dioxide (TiO_2) or tin oxide (SnO_2). Typically used solvents are γ -butyrolactone (GBL), dimethylformamide (DMF), dimethyl sulfoxide (DMSO), N-methyl-2-pyrrolidone (NMP), 2-Methoxyethanol (2-ME), chlorobenzene (CB), isopropanol (IPA) and toluene (TL). In the two-step process, BX_2 is deposited first and then converted to perovskite via exposure to AX either by dipping in AX solution in IPA or treating BX_2 films with AX vapors. Both processes are normally followed by annealing at high temperatures mainly to remove the left-over solvents and additives. Other deposition techniques like multi-source vacuum evaporation [31–34] can also be used to make perovskites. For example, thermal evaporation of PbI_2 , FAI_2 , CsBr have been employed to fabricate PSCs. However, PCEs of these devices are generally lower compared to solution

processed PSCs. Taking into account the high-efficiencies, simplicity and cost-effectiveness, industrial scale production of perovskites is expected via solution processing. However, several problems associated with this method have to be addressed for the commercialization of halide perovskites.

Over the years, many experiments established that the efficiency and stability of PSCs [35–39] and PLEDs [40, 41] depends crucially on the morphology of the material [42–45]. The lack of precise control over the manufacturing process [46] creates a risk of forming unwanted defects [47] such as iodide vacancies, photo-inactive structures, pinholes, random stacking of grains, and grain boundaries. These defects accelerate the light-induced [48] and moisture induced [49, 50] degradation of PSCs. For example, water and oxygen [51] can diffuse into the perovskite lattice through the iodide vacancies or grain boundaries. Both are highly reactive towards under-coordinated divalent metal cation eg. Pb^{2+} and can either cause irreversible conversion to water-intercalated photo-inactive phases (eg. $\text{MA}_4\text{PbI}_6 \cdot 2\text{H}_2\text{O}$) [52] or activates phase transition from photo-active metastable (eg. cubic- CsPbI_3) to photo-inactive stable phases (e.g. hexagonal- CsPbI_3). In particular, ionic defects migrate [53] under constant illumination [54] and heat corresponding to PSCs working conditions. The mobile ions/vacancies [55] can produce hysteresis [56] in devices, photo-induced phase separation [57] and promote the formation of highly reactive I_2 [58, 59] which can rapidly disintegrate the perovskite (eg. MAPbI_3) to PbI_2 . Moreover, accumulated defects on interfaces [60] between perovskite thin-films and their contact materials, can even diffuse into hole-transport materials giving rise to unstable devices. Recent experiments revealed that smaller grain sizes present lower energy barriers for ionic migration than larger ones. Therefore perovskite thin-films with smaller grain size distribution could degrade faster than thin-films with larger grain size distribution. Additionally, random stacking of grains results in poor device performances [61]. Apart from these issues, a key problem in PSCs originates from the fact that the high-efficiency PSCs are made from meta-stable phases of FAPbI_3 and CsPbI_3 . Experimentalists utilize solution processing for kinetically driven synthesis of the meta-stable forms of FAPbI_3 and CsPbI_3 . However, at the same time, structures of different intermediates and the thermodynamically stable [61, 62] photo-inactive phases can also form during this process which is harmful to PSCs.

Hence, control over perovskite micro-structure is essential to achieve high performance, long-term stability and commercialization of PSCs.

To achieve this objective, a wide range of deposition methodologies and recipes have been designed and new ones continue to emerge day by day. These involve the use of molecular additives [37, 63–66], polymers [67], ionic-liquids [68], polyiodides [69], pseudo-halides [21], controlling humidity, different anti-solvents [70], mixing various cations [71], and anions [20, 72], variations in the reaction temperature [73], vapor treatment [74], and even the use of visible light [75, 76]. However, in the race for increasing efficiencies, many engineering efforts have been confined to purely empirical trial-and-error strategies. Due to a serious lack of fundamental understanding of the atomistic mechanisms underlying the chemical synthesis

of halide perovskites. Nucleation and growth processes dictate the microstructure evolution. An accurate and detailed understanding of the fundamental aspects of crystallization will enable a more rational control over the perovskite microstructure and thereby devices with improved optoelectronic and physical properties. Therefore it is imperative to comprehend the molecular mechanism of the crystallization of perovskites.

Despite the fact that crystallization plays the main role in controlling the crystal morphology, very little is known about the nucleation and growth of halide perovskites.

To this aim, several experiments have been performed by employing X-ray diffraction (XRD)[77], transmission electron microscopy (TEM) and different spectroscopic techniques[78]. Earlier studies [79–82] investigated the precursor chemistry and their effects on final morphology. These studies suggested that crystallization proceeds via the formation of different complex intermediates. An interesting insight emerged that metal halide complexes [81, 83] (such as $[\text{PbI}_3]^{-1}$, $[\text{PbI}_4]^{-2}$, $[\text{PbI}_5]^{-3}$ and $[\text{PbI}_6]^{-4}$) dominate the pre-nucleation stage and form colloidal clusters [84, 85]. The concentration of $[\text{PbI}_4]^{2-}$ was found to be directly related to the formation of defects. Moreover, frequently used additives (eg. Cl^-) and solvents (eg. DMSO, NMP) [86] coordinate strongly with divalent cations (eg. Pb^{2+}) and promote the formation of meta-stable or stable low-dimensional intermediate structures [87–89] (eg. PbI_2 -DMSO). Further studies [90–95] have been focused on revealing structural insights of these intermediates and attempted to layout the complex pathway of the crystallization process. A recent *in-situ* XRD experiment surprisingly found that similar type of layered structures can also form on modified SnO_2 interfaces. Notably, a study from Paul *et al.* [96] revealed the structure of possible polytypes that could precipitate during the nucleation of FA based perovskites.

In contrast, experimental techniques have not yet revealed the dynamical details, thermodynamics and kinetics (rates) of the nucleation and phase transition of halide perovskite. For example, the atomic origin and formation of the pre-nucleation clusters, intermediate phases and their conversion into the perovskite structure have not been established. This is because nucleation, growth and solid-solid phase transitions are dynamical processes occurring on very short time and length scales. Nanoscopic length and time scales that characterize nucleation make this a challenging problem for experiments. Thus it is challenging to obtain microscopic-level insights on nucleation from state-of-the-art experimental techniques. An alternate approach of molecular dynamics (MD) simulations can complement experiments by providing atomic-level information on the phase transitions, therefore can help design better synthesis protocols for highly efficient and stable perovskite electronics.

In this thesis, I decided to perform MD simulations to address different aspects of crystallization of halide perovskites.

In principle, molecular simulations can outline a complete atomistic picture of the crystallization process. A straightforward way is to perform brute-force MD simulations, i.e., first set up a simulation similar to the initial/precursor solutions in experiments and evolve with time in an isothermal-isobaric ensemble at experimental pressure and temperature conditions. In

this way, one can directly observe the temporal evolution of the system. However, although nucleation is ubiquitous in nature and industries, it is tough for conventional MD simulations. This is mainly because it is a rare event that often happens on a time-scale that can be hopeless to produce from direct brute-force simulations. Many works have devoted to studying and developing new methodologies to understand the crystallization from solution. One technique is seeded simulations[97–99], where a crystalline seed is placed in the saturated solution, and then the system is evolved with time to investigate the crystallization and growth processes. Although practical and vital information about the nucleation process can be obtained in this way, seeded simulations do not allow for the direct observation of nucleation from solution.

Several enhanced sampling methods have been utilized to observe nucleation from solute-solvent mixtures in reasonable times directly. Such techniques like umbrella sampling[100–102], path sampling[103, 104], metadynamics[105], Wang-Landau[106] sampling and many other speed up the exploration of configurational space to overcome the time-scale problem in regular simulations. Despite a plethora of available methods, it is well known that every method has its constraints, especially for complex systems such as multi-component nucleation from solution. Many path sampling methods have shown promising results for understanding nucleation mechanisms from solution and rate calculations. Despite meticulous, they are often computationally expensive. On the other hand, biasing methods where sampling of low-probability microstates is increased by adding an external potential (bias) to the potential energy surface of the system. Bias potential is constructed as a function of configuration-dependent reaction coordinates. The choice of reaction coordinates is crucial and of utmost importance to the success of biased methods. The underlying principle in constructing good reaction coordinates is that they should strictly differentiate between reactant and product states and provide useful information on the reaction paths. Moreover, it is beneficial to avoid using many reaction coordinates, which increases the dimensionality of the exploration space and makes simulations harder to converge.

Different methods have been applied to systems like nucleation of urea from solution[99, 107], sodium chloride[108–111] from water, calcium carbonate[112] from water and silver bromide from solution[113]. The earlier works on nucleation simulations have been pivotal to establishing fundamental methodologies that can be modified and advanced to simulate complex problems such as mine. Most of these earlier simulation studies on crystallization were focused on relatively simpler systems like mine. Simulating the phase transitions of organic-inorganic lead halide perovskites is an equally intimidating problem and has not been attempted before. For one thing, due to the presence of several chemical species, competing crystalline phases may exist, and nucleation and growth pathways can be highly non-trivial. To overcome these challenges, I decided to adopt the following strategies:

- First, I studied nucleation and growth in the single-step process. I built necessary simulation methodologies to perform and analyze the enhanced MD simulations of crystallization of perovskites from solution. This led to the understanding of the formation of intermediate colloidal structures and the effect of monovalent cations on

the nucleation of perovskites. Atomic-level details from this study resulted in developing a new experimental methodology for a rational control over the grain size of perovskites crystals in thin-films. After realizing the importance of the intermediate clusters, further questions arose about their final impact on thin-film morphology. This is why I collaborated with experimentalists and first studied the effect of different solvents on the pre-nucleation stage. I calculated the binding energies of varying solvent molecules with Pb^{2+} and performed density functional theory (DFT) based *ab-initio* MD (AIMD) of precursor solute-solvent mixtures. I found that the binding affinities of solute-solvent clusters directly impact the size of intermediate colloidal structures, which can be tuned by mixing weaker binding solvents (in our case: tetrahydrofuran (THF)) with commonly used higher binding affinity DMSO solvent. These results were employed to develop an efficient and economical experimental recipe to make >18% PCE solar modules. I also studied the possible impacts of pseudo-halide (HCOO^-) on the crystallization process. First-principles electronic structure calculations revealed that the pseudo-halides strongly coordinate with Pb^{2+} and FA^+ cations, which could slow down the growth process. I also compared their binding affinities to the iodide vacancy site. I found they could effectively passivate I^- vacancies, therefore improving PCE over 25%.

- Secondly, I studied the two-step crystallization processes. I started with the sequential deposition where PbI_2 is deposited first and later converted to perovskite. I designed the fundamental simulation methodology and performed simulations of the two-step process. I found that the two-step proceeds via Ostwald-ripening, where an intercalated metastable structure could form at the initial stages of the phase transition, which is later converted to cubic-perovskite via a solid-solid phase transition. Once again, molecular simulations established that monovalent cations play an important role in crystallization. Moreover, I discovered new polymorphs of halide perovskites containing mixtures of edge-sharing and corner-sharing Pb-I octahedra. Studying this process, I found a new path for the low-temperature synthesis of the highly efficient metastable cubic phase of FAPbI_3 . I collaborated with experimentalists and substantiated my theoretical findings via *in-situ* X-ray and Raman spectroscopy experiments. To bring these fundamental insights to practical use, I worked with experimentalists, and we designed a new synthesis recipe to make thin-films of phase pure cubic- FAPbI_3 . Moreover, I also studied and disclosed the atomic level understanding of another two-step process, where methylammonium/formamidinium thiocyanate ($\text{MASCN}/\text{FASCN}$) vapors are used to convert the photo-inactive hexagonal phase of FAPbI_3 to the photo-active cubic phase of FAPbI_3 . I found that due to their strong affinity towards Pb^{2+} , SCN^- anions break the face-sharing Pb-I octahedra and form a metastable intermediate corner-sharing structure in access of monovalent cations. This corner-sharing structure provides a templating driving force for a low-temperature conversion from hexagonal to cubic phase. From these collaborative studies, I lay out atomic-level details of new routes for the formation of high-efficiency cubic- FAPbI_3 based PSCs. However, a fundamental question emerged: is metastable cubic- FAPbI_3 at least kinetically stable? For this, I

studied the phase transition between hexagonal and cubic FAPbI₃. From simulations, I estimated an energy barrier of ~ 0.7 eV/f.u. Between cubic and hexagonal FAPbI₃, therefore understanding the kinetic stability of cubic-FAPbI₃.

- Moreover, I studied the effect of molecular additives on the final morphology of halide perovskites. These compounds are usually added to passivate surface defects and mixed in during or after crystallization of perovskite thin-films. These additives tend to form low-dimensional perovskites, and their final structures influence the electronic properties of the PSCs. Here I focused on the crystal structure prediction of these low-dimensional materials. By using classical MD and DFT simulations, I am able to predict the crystal structures for a wide range of molecular additives. Lastly, I collaborated with experimentalists and verified these structures by comparing their chemical and physical properties with the experimental collaborators' experimental data obtained from X-ray crystallography and solid-state nuclear magnetic resonance (ssNMR) spectroscopy measurements. Lastly, I was also able to develop new inter-atomic potentials for a wide range of halide perovskites.

2 Crystallization in the single-step process

This chapter was adopted from the following articles:

Postprint version of the article: P. Ahlawat, M. I. Dar, P. Piaggi, M. Graetzel, M. Parrinello, U. Rothlisberger. "Atomistic mechanism of the nucleation of methylammonium lead iodide perovskite from solution." *Chemistry of Materials* 2020, 32 (1) 529–536, (doi: 10.1021/acs.chemmater.9b04259)

My contribution: Partially conceived and conceptualized the study. Designed, performed, analyzed all simulations and wrote the manuscript. Experimental part was carried out by Dr. Ibrahim Dar.

Postprint version of the article: J. Jeong, M. Kim, J. Seo, H. Lu, P. Ahlawat, A. Mishra, Y. Yang, M. A. Hope, F. T. Eickemeyer, M. Kim, Y. J. Yoon, I. W. Choi, B. P. Darwich, S. J. Choi, Y. Jo, J. H. Lee, B. Walker, S. M. Zakeeruddin, L. Emsley, U. Rothlisberger, A. Hagfeldt, D. S. Kim, M. Graetzel, J. Y. Kim, "Pseudo-halide anion engineering for α -FAPbI₃ perovskite solar cells." *Nature* 592, no. 7854 (2021): 381-385. (doi: 10.1038/s41586-021-03406-5)

My contribution: Conceived, conceptualized, designed, performed and analyzed all simulations in this study. I wrote the simulations part.

Postprint version of the article: H. Zhang, K. Darabi, N. Y. Nia, A. Krishna, P. Ahlawat, B. Guo, M. H. S. Almalki, T-S. Su, V. Bolnykh, L. A. Castriotta, D. Ren, M. Zendejdel, L. Pan, S. S. Alonso, R. Li, S. M. Zakeeruddin, A. Hagfeldt, U. Rothlisberger, A. D. Carlo, A. Amassian, M. Graetzel, "A universal co-solvent dilution strategy enables facile, eco-friendly and cost-effective fabrication of perovskite photovoltaics." *Nature Communications* 13, 89 (2022). (doi: 10.1038/s41467-021-27740-4)

My contribution: Conceived, conceptualized, designed, performed and analyzed all simulations. I wrote the simulations part.

2.1 Atomistic mechanism

2.1.1 Introduction

In the ongoing intense quest to increase the performance of PSCs, optimizing the morphology of perovskite materials has become imperative to achieve high PCE. MAPbI₃ has been the champion of halide perovskite semiconductors and is presently the most studied light-absorber among this class of materials. Here, in order to unravel the atomistic details of

perovskite crystallization, I perform well-tempered metadynamics (WTMetaD) simulations to study the nucleation mechanism of MAPbI₃ from a γ -butyrolactone (GBL) solution which is one of the most commonly used solvents for the crystallization of lead halide perovskites [3, 70, 114–117]. The WTMetaD simulations demonstrate that nucleation of MAPbI₃ from solution is a multi-step process. I describe the mechanism of the individual stages and present the atomistic details about the formation of intermediate phases and their conversion to the perovskite crystal. Initially, dense amorphous clusters mainly consisting of lead and iodide appear from the homogeneous solution. These clusters evolve into lead iodide (PbI₂) like structures. Subsequently, MA⁺ ions diffuse into these PbI₂-like aggregates triggering the transformation into a perovskite crystal through a solid-solid transformation. These enticing results allowed to design new experimental strategies to rationally control the dimensions of grains using spin-coating and to engineer homogeneous nucleation and growth of MAPbI₃ single crystals. Moreover, our experimental collaborator perform experiments to understand the morphological evolution of the MAPbI₃ from GBL in both: (a) homogeneous nucleation to grow single crystals from solution and (b) heterogeneous nucleation for depositing thin films using spin-coating. These MD simulation results supported with experiments allowed us to reveal insights of the evolution of the perovskite microstructure. The experimental results amply support our unprecedented observations related to the critical role of monovalent cations in inducing the nucleation process in lead halide perovskites. These insights could help in a better understanding of the crystallization process, which is essential to fabricate highly efficient PSCs and other optoelectronic devices.

2.1.2 Results

I start from a well equilibrated solution where the MA⁺, Pb²⁺ and I⁻ ions are initially homogeneously distributed in GBL. We have prepared three different simulation setups and will refer to them as simulation (A), (B) and (C), the latter two having lower concentrations of solute species. Further details are provided in the Methods section. In all cases different Pb-I complexes, such as [PbI₂], [PbI₃]⁻ and [PbI₄]²⁻ are formed spontaneously in solution with a uniform distribution. These initial configurations are shown in **Fig. 2.1a**, **Fig. A.1a** and **Fig. 2.2b** for simulations (A), (B) and (C). As expected, during the course of standard (unbiased) MD simulations, no formation of a perovskite phase is observed due to the presence of a high free energy barrier for nucleation. This free energy barrier can be rationalized on the basis of classical nucleation theory, which portrays the formation of crystalline clusters as an interplay between volume and surface contributions. In a macroscopic system, this leads to a free energy barrier for the formation of a cluster of a critical size. Before the critical cluster forms, the system undergoes order and density fluctuations that can be described as clusters of relatively small size. Eventually, a critical size cluster is formed and the system is able to surmount the barrier. Further increase in the cluster size is spontaneous. At variance with this picture, in a confined system as the one used in our simulations, the solution becomes depleted of solute atoms as the cluster grows thus decreasing the supersaturation with time. As a consequence, a finite size cluster is not stable. However, this unwanted effect does not distort

the crystallization path as previous experience has shown [107, 118]. To accelerate the rare nucleation process in such a way that it can be observed within our limited simulation time of the order of microseconds, I employ WTMetaD which constructs an external bias potential as a function of a few collective coordinates also known as collective variables (CVs). This bias potential discourages the re-visiting of frequently visited configurations thus enhancing the fluctuations of the CVs and helping the system to overcome free energy barriers.

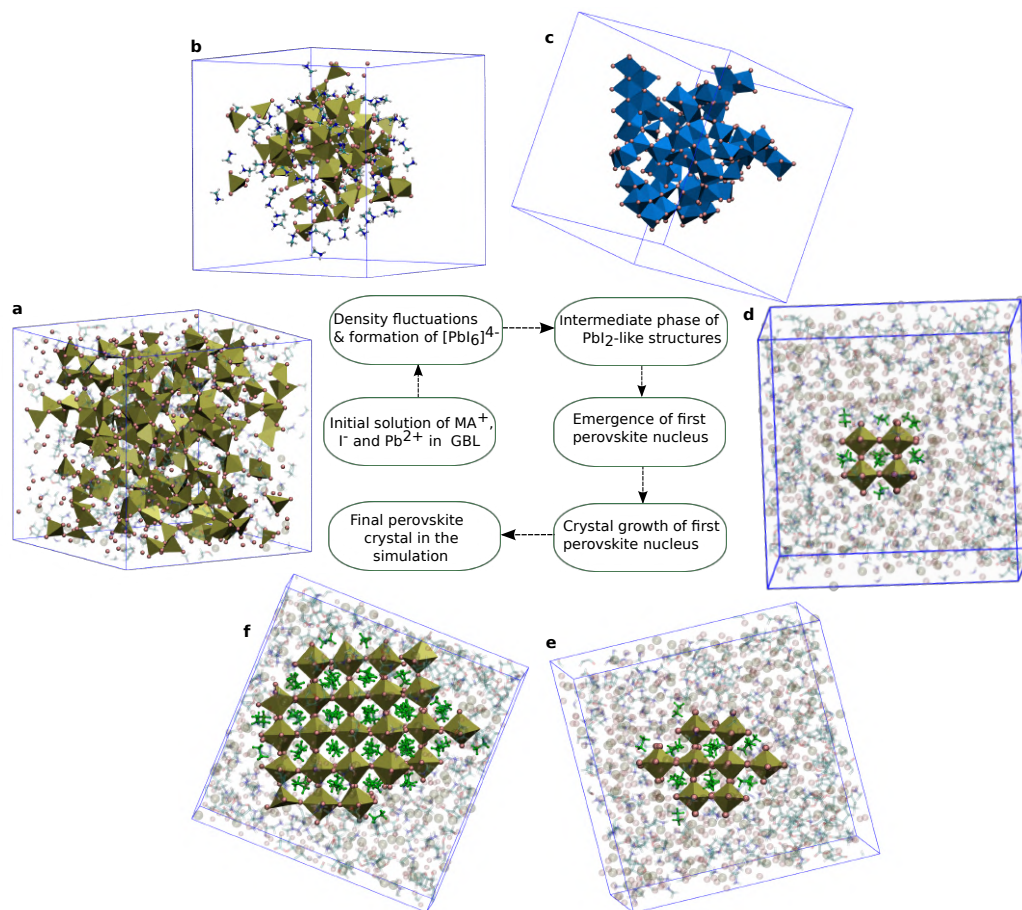


Figure 2.1 – Full nucleation pathway illustrated with representative snapshots. Pb-I complexes are shown as golden and blue polyhedra with Pb^{2+} in the center and I^- in the corners. Free I^- is shown as pink spheres. Crystalline MA^+ ions are shown in green. (a) initial solution of MA^+ , I^- and Pb^{2+} in GBL. MA^+ and GBL are shown semi-transparent to visualize the random distribution of Pb^{2+} and I^- in solution. (b) the initial cluster formation of Pb^{2+} and I^- surrounded by MA^+ ions. (c) shows only edge-sharing $[\text{PbI}_6]^{4-}$ octahedra. (d) the first perovskite nucleus observed in the solution. (e) illustrate the growth of the initial nucleus. (f) the largest perovskite crystal in the simulations. All of the images were generated with VMD [119].

An appropriate choice of CVs is essential to the success of WTMetaD simulations. I have chosen two CVs to describe the nucleation process. The first (S_p) is the number of MA^+ ions

that have a coordination with MA^+ , Pb^{2+} and I^- which is compatible with the perovskite phase. I also use S_p to represent the degree of crystallinity in the system. The second one (S_{PbI_6}) is the number of Pb^{2+} ions coordinated by six I^- .

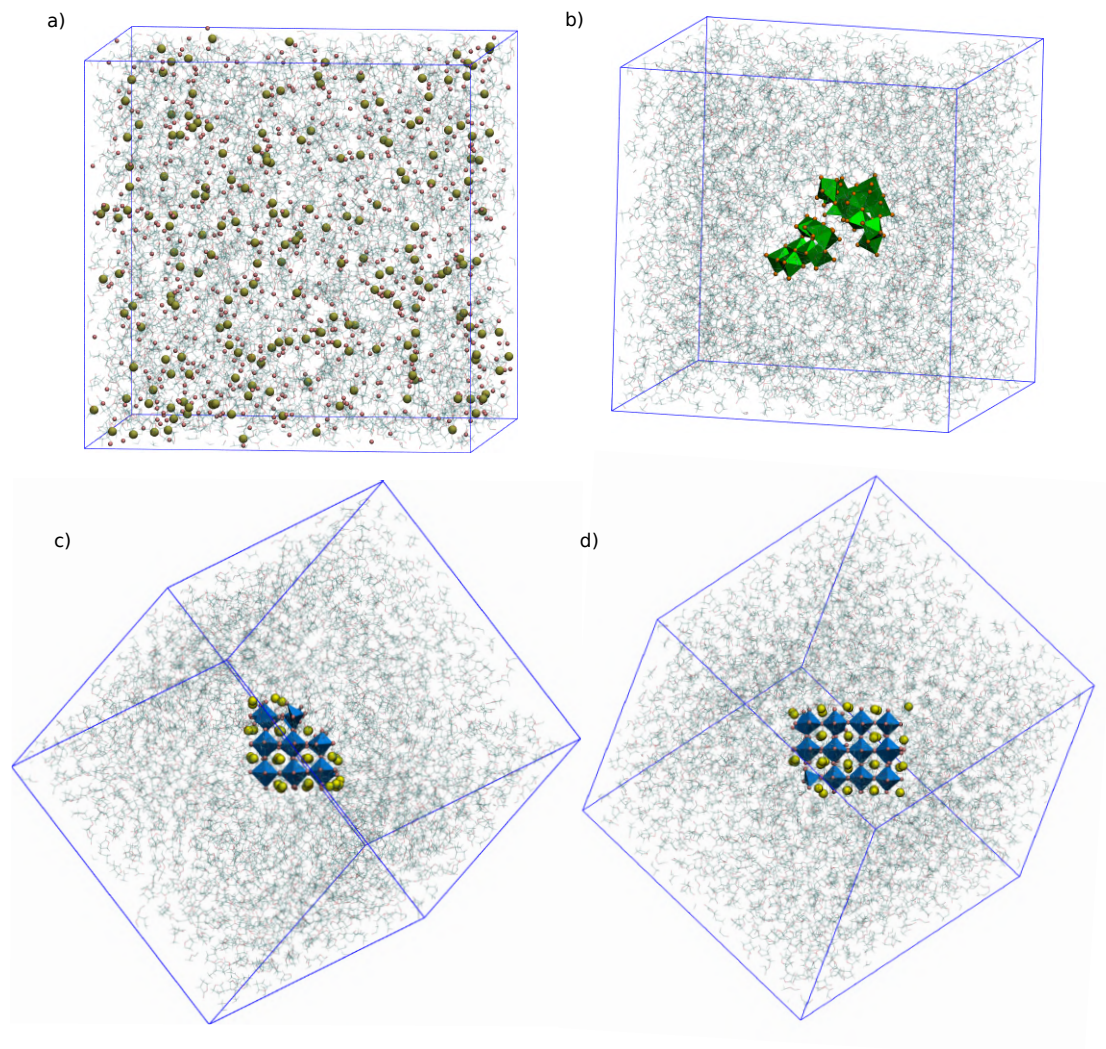


Figure 2.2 – Illustration of the full nucleation pathway for a large simulation system-(C): Pb-I complexes are shown as green and blue polyhedra with Pb^{2+} in the center and I^- on the corners. I^- is shown as pink spheres. MA^+ ions are shown with ball and sticks in the initial homogeneous solutions and yellow balls in perovskite crystals. Snapshot (a) represents the initial solution of MA^+ , I^- and Pb^{2+} in GBL. GBL molecules are represented with balls and stick model and shown as semi-transparent. Snapshot (b) shows the intermediate edge-sharing chains of $[\text{PbI}_6]^{4-}$ octahedra. Images (c) and (d) are the perovskite crystals observed in the simulations. Image (d) is the side view of image (c). All the images of these snapshots are generated with VMD-1.9.2.[119]

Further details about the CVs are described in the Methods section. During the course of the WTMetaD simulations, perovskite crystals ultimately form in all simulations. The formation

of these large crystals is shown in **Fig. 2.1f** for simulation (A), in the **Fig. A.1d** and **Fig. 2.2d** for simulation (B) and (C). I have observed a similar qualitative nucleation mechanism in all simulations. I have identified three different stages of the biased WTmetaD simulation trajectories that correspond to different steps during the nucleation and crystallization process as depicted in **Fig. 2.3**. At the first stage, amorphous clusters of Pb-I complexes emerge from the solution. In the second stage, the amorphous clusters partially transform into the perovskite structure. In the last stage of our trajectories, the crystal grows by sequential addition and arrangement of ions around the initial nucleus. In the next paragraphs, I describe each stage in detail.

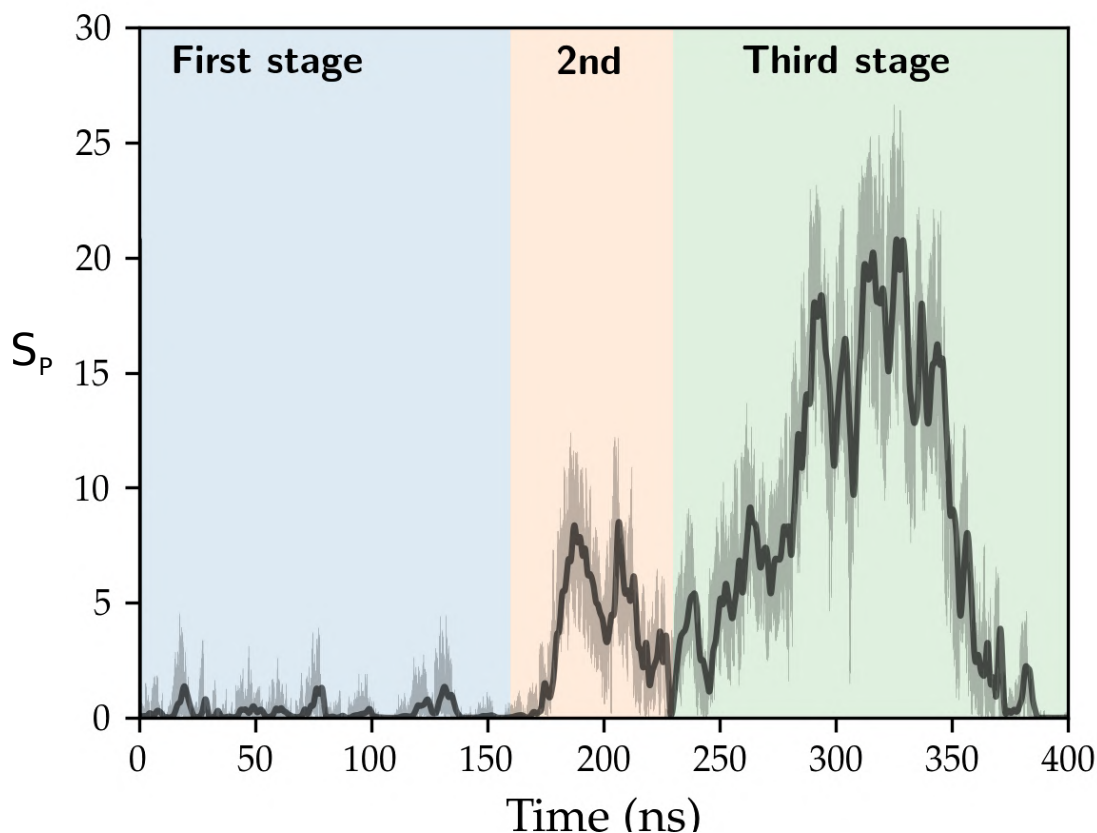


Figure 2.3 – Perovskite CV employed to drive the nucleation process. In order to guide the eye, the running average (over 1ns interval) of the CV is shown as a thick black line. The stages into which the simulation is divided for the purpose of analysis are shown with different colors (see text for details). Time on x-axis is WTmetaD time.

At the first stage, I observe increased fluctuations in the number of $[\text{PbI}_6]^{4-}$ octahedra as shown in **Fig. 2.4**. The relative increase in the coordination of Pb^{2+} with I^- is achieved by two or more Pb^{2+} sharing the same I^- . As a result, clusters made from face or edge-sharing $[\text{PbI}_6]^{4-}$ octahedra are formed. The time evolution of edge-sharing octahedra is presented in **Fig. A.2**. This is in contrast to the network of corner sharing $[\text{PbI}_6]^{4-}$ octahedra that is characteristic for the final perovskite structure. MA^+ ions surround the $[\text{PbI}_6]^{4-}$ clusters to compensate the

large negative charge. These processes increase the local density of solute species. I observe that $[\text{PbI}_6]^{4-}$ can eventually transform back to lower order iodoplumbates but the high local density of solute species is preserved.

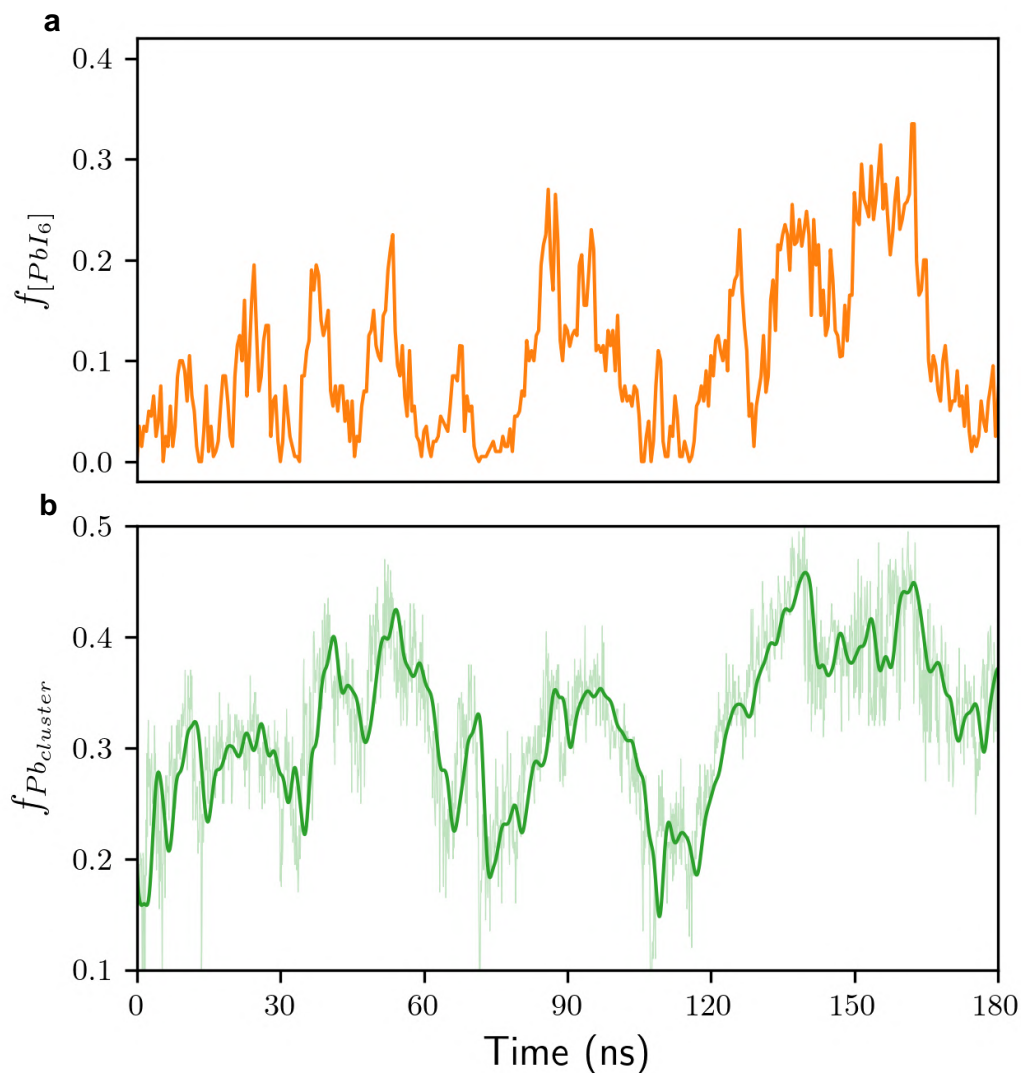


Figure 2.4 – **Analysis of the first stage in which cluster formation is observed.** Top panel (a) displays the number of $[\text{PbI}_6]^{4-}$ complexes divided by the total number of Pb^{2+} ions in our simulation. The bottom panel (b) shows the size of the largest cluster as a function of simulation time. Here we represent the size of the cluster as the fraction of Pb^{2+} ions in the cluster out of the total of Pb^{2+} ions in the simulation box.

In order to quantify the local density fluctuations, I have performed a clustering of Pb^{2+} ions

that are coordinated by at least three I^- ions within a radial cutoff of 0.40 nm. Further details on the calculations of the size of these clusters are presented in the methods section. At the end of this stage, after ~ 140 ns, Pb^{2+} and I^- ions have formed relatively large amorphous clusters as depicted in **Fig. 2.1b**.

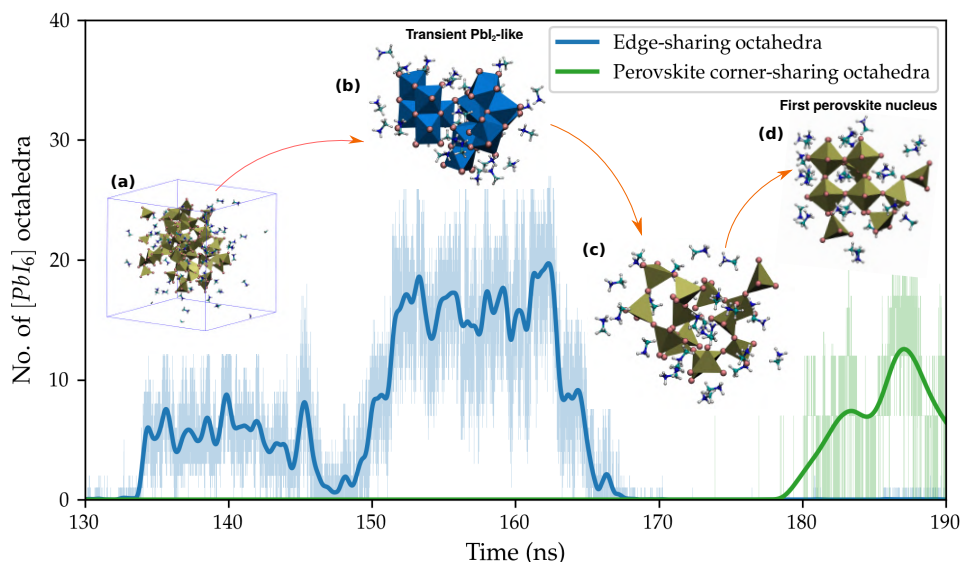


Figure 2.5 – Analysis of the second stage with representative images. Time evolution of edge-sharing and perovskite corner-sharing octahedra. Thick lines are the running average (over 1 ns interval) of the data and are shown in order to guide the eye. (a) the initial cluster at ~ 140 ns. (b) the configuration of the part of the cluster that evolves into the first perovskite nucleus at ~ 161 ns. (c) represents the evolution of the same cluster at ~ 175 ns. (d) the first perovskite nucleus in our simulation at ~ 180 ns. Time on x-axis is WTmetaD time

In the next stage, a part of the amorphous clusters transforms into perovskite. It has been shown that PbI_2 -like structures can be important intermediates (or byproducts) in the crystallization of MAPI [70, 120, 121]. Therefore, I quantify the formation of PbI_2 -like structures in terms of the number of edge-sharing $[\text{PbI}_6]^{4-}$ octahedra that share at least three edges with neighbouring $[\text{PbI}_6]^{4-}$ octahedra. I also assess the amount of perovskite formed in the solution. To do so, I calculate the number of corner-sharing $[\text{PbI}_6]^{4-}$ octahedra that share all six corners with neighbouring $[\text{PbI}_6]^{4-}$ and Pb-I-Pb angles between them that are consistent with the cubic perovskite structure of MAPI at high temperature. Further details on selecting the angle cutoff and calculations of corner-sharing octahedra are provided in the methods section. In **Fig. 2.5**, I show the number of edge-sharing and corner-sharing perovskite octahedra as a function of simulation time. Initially, the number of edge-sharing octahedra increases and attains a maximum value at ~ 161 ns. The configuration of edge-sharing octahedra at this time is shown in **Fig. 2.1c**, **Fig. 2.5** and **Fig. 2.6**

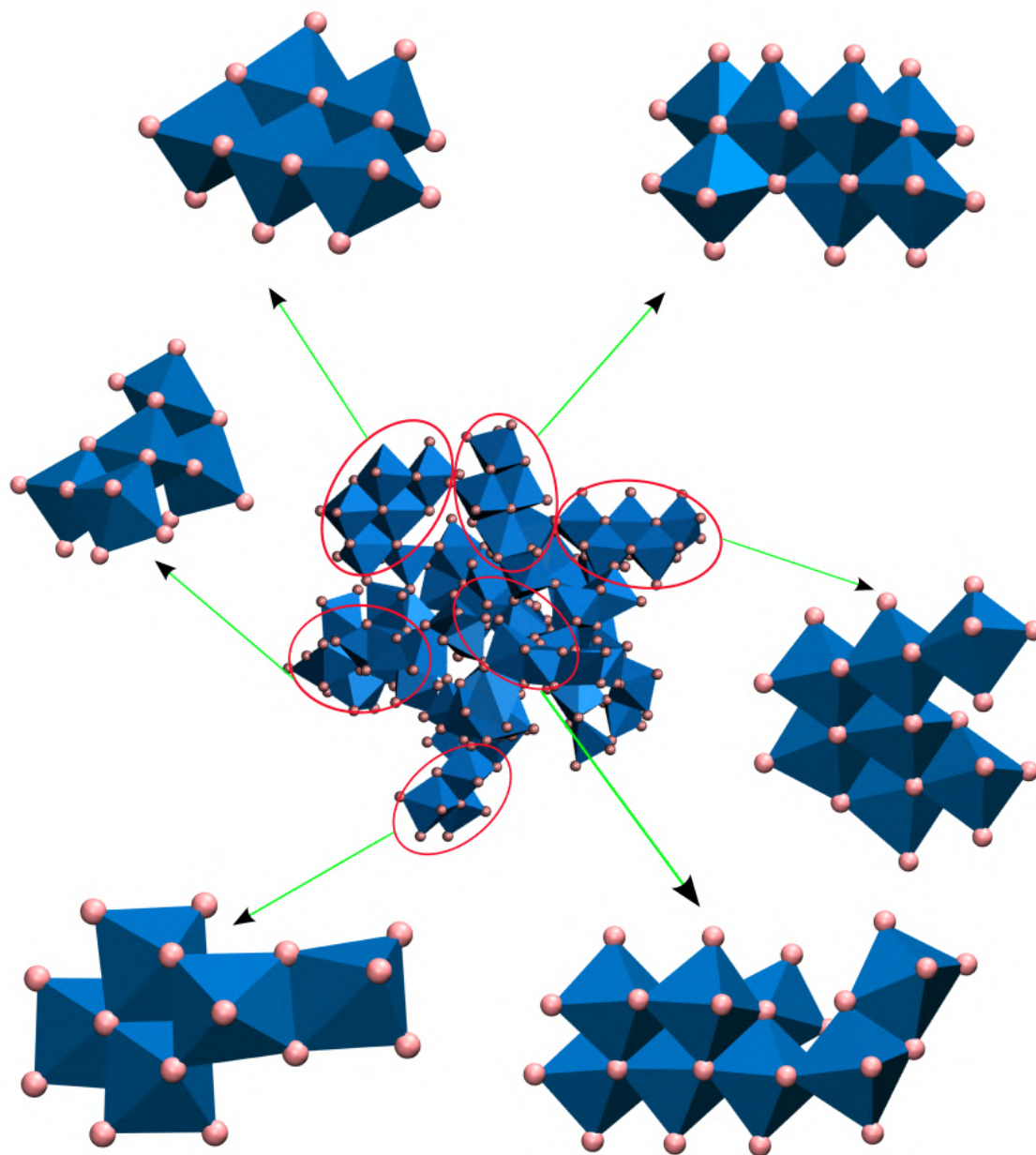


Figure 2.6 – **Visualization of intermediate phases:** The picture in the middle represents the clusters of edge-sharing octahedra in our simulation (A) at ~ 161 ns. Pb-I complexes are shown as blue octahedra with Pb^{2+} in the middle and I^- on corners. I^- is shown as pink spheres. Individually arranged structures within edge-sharing clusters are displayed separately. All the images of these snapshots are generated with VMD-1.9.2 [119]

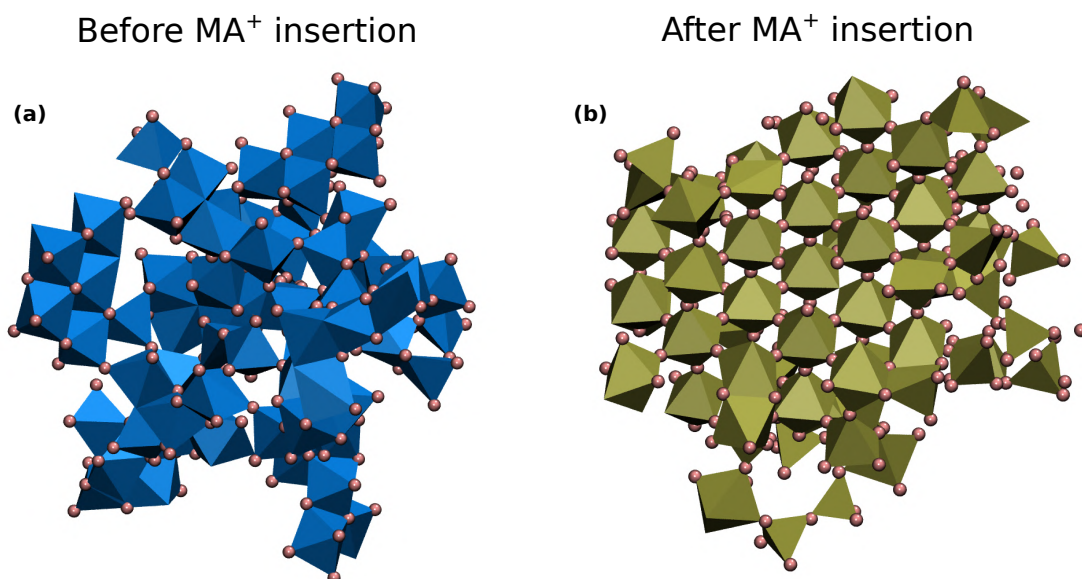


Figure 2.7 – Left panel (a) shows the configuration of edge-sharing octahedra at ~ 161 ns. Here we have excluded MA⁺ ions and solvent molecules. Pb-I geometry is shown with blue octahedra with Pb²⁺ in the center and I⁻ on the corners. I⁻ is shown in pink spheres. Right panel (b) shows the configuration of the same species at ~ 327 ns. Pb-I geometry is shown with golden octahedra with Pb²⁺ in the center and I⁻ on the corners.

From **Fig. 2.6** one can see that individual parts of these configurations show a remarkable resemblance to the rocksalt crystal structure. However, these clusters are not big and are arranged in a way that leaves of PbI₂ space between them, therefore I qualitatively name this a PbI₂-like structure. Therefore, a detailed pictorial distribution of the clusters of PbI₂-like structures of edge-sharing octahedra is shown in **Fig. 2.6**. From the analysis presented in **Fig. 2.7**, it is evident that 95% of the edge-sharing octahedra later convert to the perovskite structure. In the snapshots of Fig. 2.5, the time evolution of the ions that form the first perovskite structure is shown.

Moving further along the trajectory the PbI₂-like structure starts to transform into [PbI₄]²⁻ tetrahedra. This can be seen in **Fig. 2.5** where the number of edge-sharing octahedra decreases. Since the PbI₂-like structure opens up, space is created between Pb-I complexes. During this process, MA⁺ ions diffuse into these spaces. This mechanism can be observed in the snapshots of **Fig. 2.5**. To quantify the diffusion of MA⁺ ions, I have calculated the self diffusion coefficient (D) of the subset of MA⁺ ions that form the first perovskite crystal. From **Fig. 2.8**, a sharp increase in the diffusion of MA⁺ ions from ~ 155 to ~ 177 ns can be noticed. The sharp increase in D takes place during the time interval where PbI₂-like structures are the most abundant. This suggests that the formation of PbI₂ seems to be correlated with the diffusion of MA⁺ ions inside the Pb-I clusters. From snapshot (c) in **Fig. 2.5**, one can see that MA⁺ ions are located in the vicinity of [PbI₄]²⁻ tetrahedra.

Around 180 ns this structure rearranges into perovskite corner-sharing $[\text{PbI}_6]^{4-}$ octahedra with MA^+ ions in the center of cubo-octahedral cages. A snapshot of the first born perovskite crystal is shown in **Fig. 2.5**. It can also be seen in **Fig. 2.5** that there is an increase in the number of perovskite corner-sharing octahedra compatible with the formation of a perovskite phase. Also, in **Fig. 2.8**, the diffusion diminishes substantially implying that the MA^+ ions have become part of the newly formed perovskite crystal.

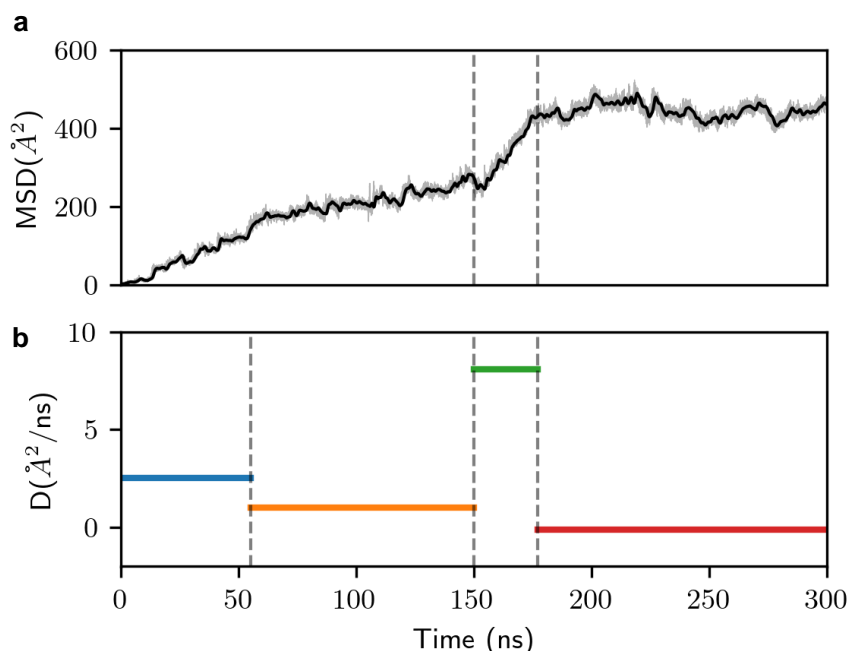


Figure 2.8 – **Diffusion analysis of the subset of MA^+ ions.** Time evolution of (a) mean square displacement and (b) diffusion coefficient of MA^+ ions that take part in the formation of the first perovskite nucleus.

At the final stage, the initial perovskite crystal grows as shown in **Fig. 2.3**. Snapshots illustrating this process are displayed in **Fig. 2.1d-f**. During this process, MA^+ ions from solution come to the surface of the perovskite crystal. To quantify this, I select the MA^+ and Pb^{2+} ions that form the largest perovskite crystal shown in **Fig. 2.1f** and calculate the concentration of these ions in a specific region around the center of the first perovskite nucleus. The dimensions of this region are selected based on the size of the largest observed crystal corresponding to simulation time $\sim 327\text{ns}$. I find that the concentration of Pb^{2+} ions at this stage remains approximately the same after the first stage. However, it can be observed from **Fig. 2.9a** that there is a continuous increase in the concentration of MA^+ ions around the center of the nucleus and that reaches a maximum at $\sim 327\text{ns}$. This strongly suggests that MA^+ ions have a fundamental role in the nucleation process. As the MA^+ ions reach the surface of the crystal, a simultaneous formation of perovskite corner-sharing octahedra around these MA^+ ions occurs. This can be seen from the increase in the number of corner-sharing octahedra in **Fig. 2.9b** and the increase in S_p in **Fig. 2.3**.

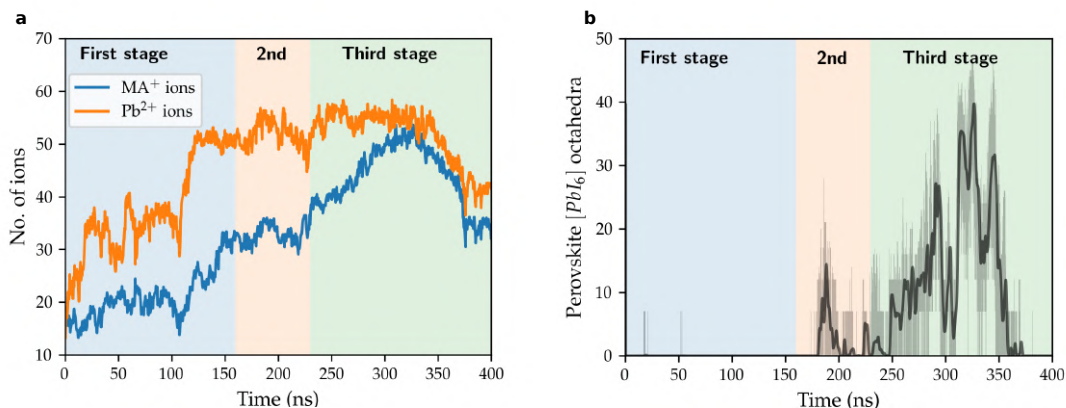


Figure 2.9 – **Analysis of the growth.** Left panel shows the change in number density of MA⁺ and Pb²⁺ ions around the center of the first perovskite nucleus. Right panel displays the temporal evolution of perovskite corner-sharing octahedra. The thick black line in the right panel is the running average (over 1 ns interval) of the data and is shown to guide the eye. Time on x-axis is WTmetaD time.

Around 327 ns, the crystal attains its maximum size and afterwards it gradually dissolves due to the above mentioned depletion effect in a finite size system. In summary, from the metadynamics simulations, the following qualitative description of the nucleation process of MAPi perovskite from GBL solution is emerging: Nucleation starts from the formation of aggregates of Pb²⁺ and I⁻. This result is in general agreement with the experimental studies from Yan *et al.*[84] and Kadro *et al.*[116] where colloids of Pb-I complexes display the Tyndall effect even at higher temperatures. Afterwards, these aggregates evolve into clusters of edge-sharing [PbI₆]⁴⁻ octahedra and a PbI₂-like intermediate phase is formed. Here I show that these intermediate phase is dominated by a rocksalt type. Eventually, MA⁺ ions diffuse into the Pb-I clusters and the PbI₂-like intermediate phase transforms into perovskite. In addition, I have identified that the continuous diffusion of MA⁺ ions into Pb-I clusters starts the nucleation and growth of perovskite. Furthermore, these results suggest that the formation of a PbI₂-like phase might facilitate the diffusion of MA⁺ ions into the Pb-I clusters.

2.1.3 Experimental results and discussion

To ascertain that MA⁺ ions induce the nucleation and formation of MAPbI₃ perovskite structures, myself and our experimental collaborator designed experiments involving both heterogeneous and homogeneous nucleation processes. To investigate the heterogeneous nucleation, we deposited MAPbI₃ (0.75 M, denoted as solution A) from GBL on glass substrate using a spin-coating technique. More experimental details are provided in the Methods section. The morphological characterization carried out using field-emission scanning electron microscopy (SEM) revealed the formation of contiguous films composed of >10 μm sized perovskite grains (Fig. 2.10a).

Interestingly, when an excess amount of MAI (0.25 moles) was added to the precursor solution A, the dimensions as well morphology of polydisperse grains changed drastically (**Fig. 2.10b**), inferring a strong correlation between MA^+ ions and the nucleation process. By increasing the excess amount of MAI to 0.5 moles, the dimensions of MAPI grains decreased further as evident from **Fig. 2.10c** and histograms (**Fig. 2.10d-f**). Such a growth behaviour could be explained by evoking variation in the nucleation density, which gets amplified when excess MA^+ ions are introduced into the precursor solution.

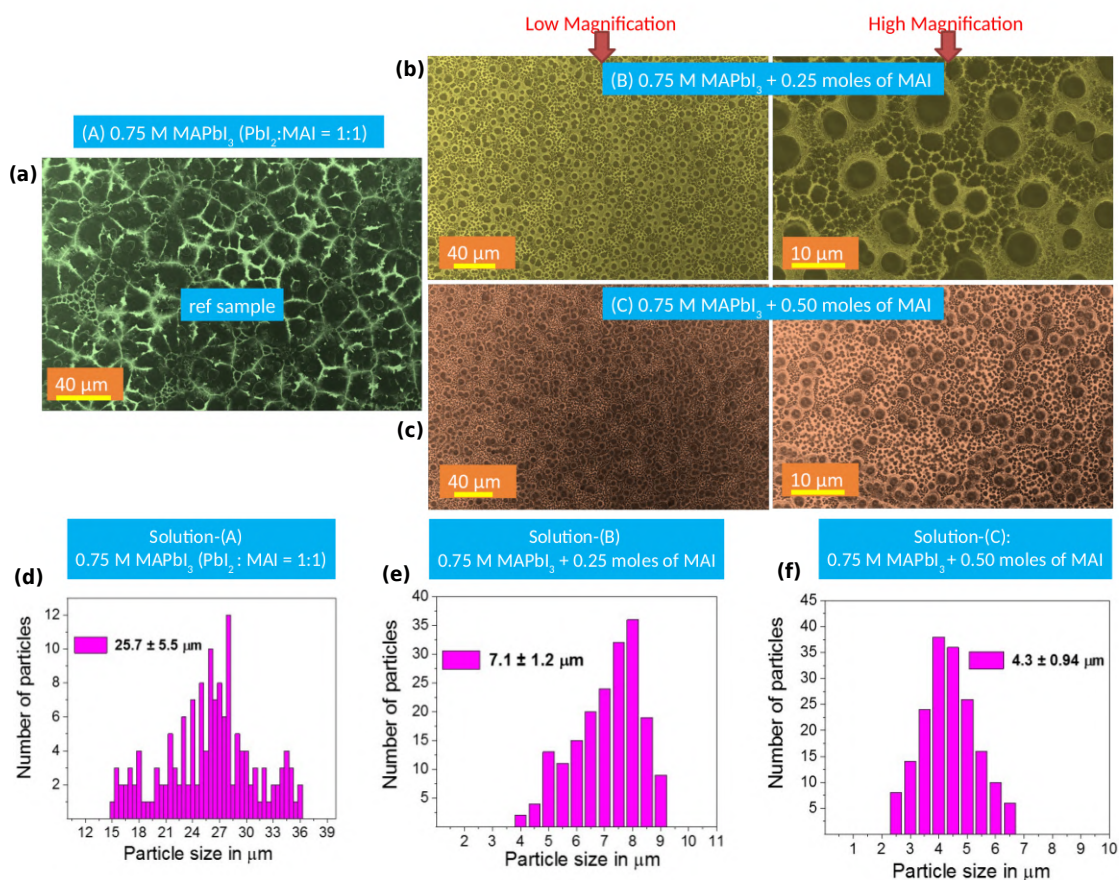


Figure 2.10 – Morphological characterization of thin films: (a) shows the top view SEM micrographs acquired from 0.75M MAPbI₃ films with 1:1 ratio of PbI₂ and MAI in the precursor solution. (b) shows the top view SEM micrographs acquired from the addition of extra 0.25 moles of MAI and (c) displays the top view SEM micrographs acquired from the addition of extra 0.50 moles of MAI. Left panel and right panel in (b) and (c) are the low and high magnification data from the SEM micrographs and also indicated in the respective figures. Figures (d), (e) and (f) show the grain size distribution of the final perovskite thin films prepared from solution-(A), solution-(B) and solution-(C) respectively. Further details are provided in the Methods section. We majorly considered large-sized grains for histograms owing to the presence of polydisperse grains.

A plethora of research demonstrates that perovskite films comprising large grains lead to the fabrication of highly-efficient and stable PSCs. By tailoring the interaction between solvent molecules or additives with MA^+ ions, it is possible to engineer the intermediates, which can consequently slow down the nucleation process to obtain high-quality perovskite grains. To further mimic our simulation, we investigated the homogeneous nucleation of MAPbI_3 as a function of MAI concentration in GBL by exploiting the inverse temperature crystallization (ITC) (**Fig. 2.11**). It is worth mentioning that ITC is one of the most explored processes to grow perovskite single crystals. There have been previous efforts to study the effect of monovalent cations on the morphological evolution of MAPbI₃ single crystals [122]. Here we perform similar experiments to understand the effect of MA^+ on nuclei density of perovskites. The formation of MAPbI_3 perovskite crystals can be easily visualized in the different vials displayed in **Fig. 2.11**. From comparative analysis, we conclude that the number density of the perovskite crystals increases with increasing concentration of MAI (**Fig. 2.11**). These results qualitatively support our theoretical simulations that a higher amount of MA^+ ions produces a greater number of perovskite nuclei in a perovskite precursor solution. Both so-called heterogeneous nucleation (spin-coating) and homogeneous nucleation (inverse solubility method) reveal the critical role of monovalent cations in inducing the nucleation of lead halide perovskites. In summary, the insights gained through simulation and experiments allowed to put forth some basic rules for controlling the dimensions and morphology of perovskite grains.

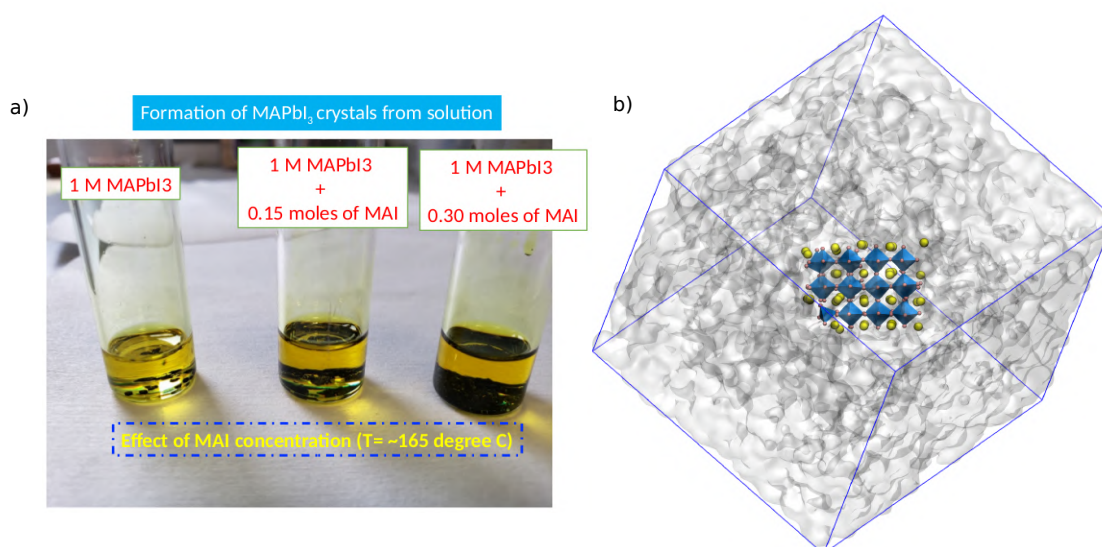


Figure 2.11 – Experimental results and analysis of homogeneous nucleation: Figure (a) shows the crystallisation of MAPbI₃ crystals in three different vials with three different concentrations of MAI in each vial. The respective concentrations in each vial are depicted in the picture itself. From left to right crystals grown in test tubes display the distinct black color of MAPbI₃ perovskite structure. Figure (b) displays the crystal of MAPbI₃ in GBL from simulations at the same experimental conditions of 1M concentration and 170°C. Pb-I octahedra are shown in blue color. MA^+ are shown as yellow spheres. I^- are represented with pink spheres.

2.1.4 Conclusions

To conclude, in this work we employ WTMetaD simulations to uncover the salient atomistic features of the nucleation of MAPI from solution. Here I have performed MD simulations of nucleation of a very complex multicomponent systems from solution. Simulations reveal that a PbI_2 -like phase appears from the clusters of Pb^{2+} and I^- before the onset of nucleation. This is followed by the diffusion of MA^+ ions into PbI_2 -like aggregates triggering the transformation into a perovskite. In this study, the relevant intermediate steps of the entire process were characterized with atomic detail. This mechanistic understanding of the nucleation process helped in designing relevant experiments to improve strategies for a better control over perovskite morphology which are necessary to design industrial processes to make highly efficient perovskite based solar cells, LEDs, and photodetectors. Furthermore, this work lays the foundations to study the atomistic details of nucleation and crystal growth of different perovskites.

2.1.5 Methods

MD simulations

Simulation (A) discussed in this work was prepared with 200 units of PbI_2 and 200 units of MAI, which are randomly distributed in 112 GBL molecules by using the *insert-molecule* utility of the gromacs simulation package. Simulation (B) was prepared in the same way with 180 units of PbI_2 and 180 units MAI randomly distributed in 368 GBL molecules. Simulation (C) was prepared with 200 units of PbI_2 and 200 units MAI randomly distributed in 2200 GBL molecules. A fixed point charge force field was chosen for MAPI [123] that is known to reproduce the high temperature cubic phase and the generalized amber force field (GAFF)[124] was used for GBL. The heterogeneous solute-solvent van der Waals (VdW) parameters were calculated based on the Lorentz-Berthelot mixing rules. In the force field for MAPI from Mattoni *et al.*[123], the VdW interactions of Pb^{2+} and I^- are modelled with a Buckingham-type potential. Therefore to calculate the heterogeneous solute-solvent parameters with mixing rules, I used the Lennard-Jones parameters of Pb^{2+} and I^- from Gutierrez-Sevillano *et al.*[125]. I have chosen a 1.0 nm cutoff for nonbonded interactions and three-dimensional periodic boundary conditions were applied for each simulation. Long range electrostatic interactions are treated with the particle-particle-particle-mesh Ewald method. I employ the SHAKE algorithm[126] to constrain the bond length of hydrogen atoms. The time step used in all of the simulations is 2 fs. All simulations are performed with the Large-scale Atomic/Molecular Massively Parallel Simulator(LAMMPS) code (31 Mar 2017)[127]. The systems were first minimized with a conjugate gradient algorithm with a tolerance of maximum residual force of 10^{-3} kcal/mol/Angstrom. After minimization, the systems were relaxed with a 100ps NVT equilibration run. All production run simulations presented in this work were carried out in the isothermal-isobaric ensemble. I use a velocity rescaling thermostat [128] with a relaxation time of 0.1 ps. Simulations (A) and (B) were carried out at 410K and simulation (C) was at 450K.

The Parrinello-Rahman barostat [129] was used to keep the pressure equal to the standard atmospheric pressure. The relaxation time of the barostat was set to 10ps. With this setup, at first we equilibrate the fully solvated simulations for 500 ps. In this way, the ions are uniformly dispersed in the solvent and density inhomogeneities are eliminated. After completing the equilibration run, the production WTmetaD run was started for longer time scales, typically up to 400 ns to 1000 ns. WTmetaD simulations were performed with a set of CVs which are described in detail in the next section.

Collective variables

The choice of the CVs is critical to be able to describe the crystallization from enhanced sampling simulations such as WT-MetaD. It is essential to carefully select the appropriate collective variables (CVs) which can enhance the fluctuations in the local order of crystalline species that form in solution. A multitude of CVs have been used to study crystallization, however most of them can only force the system to crystallize in specific crystalline structures. In this work, we propose a new CV named S_P , that does not presume a specific crystalline phase of MAPI. Thus, it enables us to observe all complexes that form before the onset of nucleation and reveal important details about the early stages of nucleation. This CV describes the local order of the species as a product of the individual local densities of MA^+ , Pb^{2+} and I^- centered around MA^+ . Here, I represent the location of MA^+ with the position of the center of C-N axis of the MA^+ ion. At first, I evaluate the local densities in the form of coordination numbers (f_i^α) of individual species MA^+ , Pb^{2+} and I^- surrounding the position i in the center of C-N axis of MA^+ within a defined cutoff radius (r_{cut}^α).

$$f_i^\alpha = \sum_{j=1}^{N_\alpha} \frac{1 - \left(\frac{r_{ij}}{r_{cut}^\alpha}\right)^a}{1 - \left(\frac{r_{ij}}{r_{cut}^\alpha}\right)^b} \quad (2.1)$$

Where r_{ij} is the distance between positions of i and j . The values for r_{cut}^α are selected based on the first minimum of the radial distribution function ($g(r)$) of MA^+ in the perovskite structure. To calculate the local densities, ρ_i^α , I define another switching function in the space of coordination numbers.

$$\rho_i^\alpha = \frac{1 - \left(\frac{f_i^\alpha}{f_{cut}^\alpha}\right)^{-m}}{1 - \left(\frac{f_i^\alpha}{f_{cut}^\alpha}\right)^{-n}} \quad (2.2)$$

Where f_{cut}^α is the lower threshold of the coordination number. The values for f_{cut}^α are chosen equal to the number of MA^+ , Pb^{2+} and I^- in the first coordination sphere of MA^+ in the perovskite structure of MAPI. The local order around i is calculated by multiplying the individual local densities of each species.

$$\eta_i = \prod_{\alpha=\text{MA}, \text{Pb}, \text{I}} \rho_i^\alpha \quad (2.3)$$

The final expression for the CV is the following:

$$S_P = \sum_{i=1}^{N_{MA}} \eta_i \quad (2.4)$$

Where N_{MA} is the number of MA^+ ions around which the variables are defined. We have implemented this CV in PLUMED-2.4[130]. The values for r_{cut}^α and f_{cut}^α that are used in our simulation are shown in the following table.

Table 2.1 – Values for the switching functions used in S_P

Species	r_{cut}^α	f_{cut}^α
$MA^+ - MA^+$	0.75nm	6.0
$MA^+ - Pb^{2+}$	0.70nm	8.0
$MA^+ - I^-$	0.55nm	12.0

The second CV, S_{PbI_6} is defined as the number of Pb^{2+} ions that have a coordination of six with I^- within a certain threshold. At first, I calculate the coordination number of Pb^{2+} with I^- .

$$f_i^{Pb-I} = \sum_{j=1}^{N_I} \frac{1 - \left(\frac{r_{ij}}{r_{cut}^{Pb-I}} \right)^a}{1 - \left(\frac{r_{ij}}{r_{cut}^{Pb-I}} \right)^b} \quad (2.5)$$

Where r_{ij} is the distance between positions of i and j . Here i and j represent the indices of Pb^{2+} and I^- . Then we define another switching function in the space of coordination number of $Pb-I$.

$$S_{PbI_6} = \sum_i^{N_{Pb}} \frac{1 - \left(\frac{f_i^{Pb-I}}{f_{cut}^{Pb-I}} \right)^{-m}}{1 - \left(\frac{f_i^{Pb-I}}{f_{cut}^{Pb-I}} \right)^{-n}} \quad (2.6)$$

The values for r_{cut}^{Pb-I} and f_{cut}^{Pb-I} are taken as 0.39 nm and 6. The values for a, m and b, n are 6 and 12. The height of the Gaussian bias potentials is set to $\approx 2k_B T$. The width of the Gaussian bias potentials is set to 0.5 and 1.0 for S_P and S_{PbI_6} respectively. The Gaussian hills are deposited after every 1 ps. I have chosen a bias factor of 300 that allows for an extensive exploration of hundreds of solute molecules contained in a typical simulation box. More theoretical details on WTmetaD can be found in references[131][105].

2.1.6 Clustering at the first stage

In order to quantify the number and type of the clusters of Pb^{2+} and I^- at the first stage of nucleation in our simulations, I have performed a clustering analysis with the depth first

search (DFS) algorithm. Further details on using this method and the implementation in PLUMED 2.4[130] are provided in reference [132]. The following plumed input is used for clustering.

Plumed input file:

```
##### Plumed input #####
### An example for the simulation-(A) ###
Pb:  GROUP ATOMS=1-200
I:   GROUP ATOMS=201-800

cPbI: COORDINATIONNUMBER SPECIESA=Pb SPECIESB=I SWITCH={CUBIC D_0=0.40 D_MAX=0.41}
cPbI3: MFILTER_MORE DATA=cPbI SWITCH={CUBIC D_0=2.99 D_MAX=3.00}
cmPbI3: COORDINATIONNUMBER SPECIES=cPbI3 SWITCH={CUBIC D_0=0.70 D_MAX=0.71}
cmPbI34: MFILTER_MORE DATA=cmPbI3 SWITCH={CUBIC D_0=3.99 D_MAX=4.00}
cm: CONTACT_MATRIX ATOMS=cmPbI34 SWITCH={CUBIC D_0=0.70 D_MAX=0.71}
dsf: DFSCLUSTERING MATRIX=cm
nat1: CLUSTER_NATOMS CLUSTERS=dsf CLUSTER= 1
PRINT: ARG=nat1 FILE=COLVAR_cluster
```

In the first two lines, the number of Pb^{2+} ions (cPbI3) that are coordinated by at least three I^- ions within a radial cut-off of 0.40 nm are calculated. Then the coordination number of these Pb^{2+} ions (cPbI3) with each other is calculated and only those Pb^{2+} ions (cmPbI34) are selected which have a coordination number of at least four between them with a radial cutoff of 0.70 nm. An adjacency matrix is built between cmPbI34 within a cutoff distance of 0.70 nm and the corresponding cluster is calculated with the DFS algorithm.

2.1.7 Edge-sharing octahedra

To calculate the number of edge-sharing octahedra, I identify the Pb^{2+} ions that have a six fold coordination with I^- in a radial cutoff of 0.40 nm as described in the equations for S_{PbI_6} . Since the positions of Pb^{2+} and I^- ions are fluctuating continuously in our simulations, I decide to take a larger cutoff as compared to the nearest distance between Pb^{2+} and I^- in the MAPI perovskite structure. However, my algorithm only selects the nearest six I^- to Pb^{2+} and assigns them as $[\text{PbI}_6]^{4-}$ octahedra. Then I quantify them on the basis of number of I^- shared between two neighbouring $[\text{PbI}_6]^{4-}$ in a distance of 0.50 nm between them. This distance cutoff is chosen according to the first coordination sphere of Pb^{2+} atoms in the crystalline P-3m1 structure of PbI_2 . The partial radial distribution function ($g(r)$) of Pb^{2+} - Pb^{2+} ions in the crystalline cubic phase of MAPI and the P-3m1 phase of PbI_2 is shown in **Fig. A.3**. A $[\text{PbI}_6]^{4-}$ octahedra is identified as an edge-sharing octahedra if the indices of any two of six I^- that take part in the formation of this $[\text{PbI}_6]^{4-}$ octahedra are the same as any two out of six I^- of neighbouring $[\text{PbI}_6]^{4-}$ octahedra. Edge-sharing $[\text{PbI}_6]^{4-}$ octahedra are classified based on the

number of edges shared between them. I call a $[\text{PbI}_6]^{4-}$ octahedron as 1-edge-sharing if at least one-edge is formed between them, 2-edge-sharing if a $[\text{PbI}_6]^{4-}$ octahedron shares at least two edges with two different $[\text{PbI}_6]^{4-}$ octahedra, 3-edge-sharing shares at least three edges with three different $[\text{PbI}_6]^{4-}$ octahedra. In **Fig. A.2** I show the time-evolution of the number of edge-sharing octahedra in simulation (A). It can be noticed that all types of edge-sharing octahedra reach maxima at the second stage $\sim 161\text{ns}$. At this time, I observe aggregates of edge-sharing octahedra as displayed in **Fig. 2.6**. Since it is difficult to see the arranged PbI_2 -like structures in this cluster, therefore for clarity, in **Fig. 2.6** I also display the individual regions of the cluster. These smaller clusters of edge-sharing octahedra show remarkable similarity with the unit cell of PbI_2 . I also track the evolution of these edge-sharing octahedra in our simulation. From **Fig. 2.7**, one can see that almost all of the edge-sharing octahedra in simulation (A) get converted into a perovskite structure at $\sim 327\text{ns}$.

2.1.8 Perovskite corner-sharing octahedra

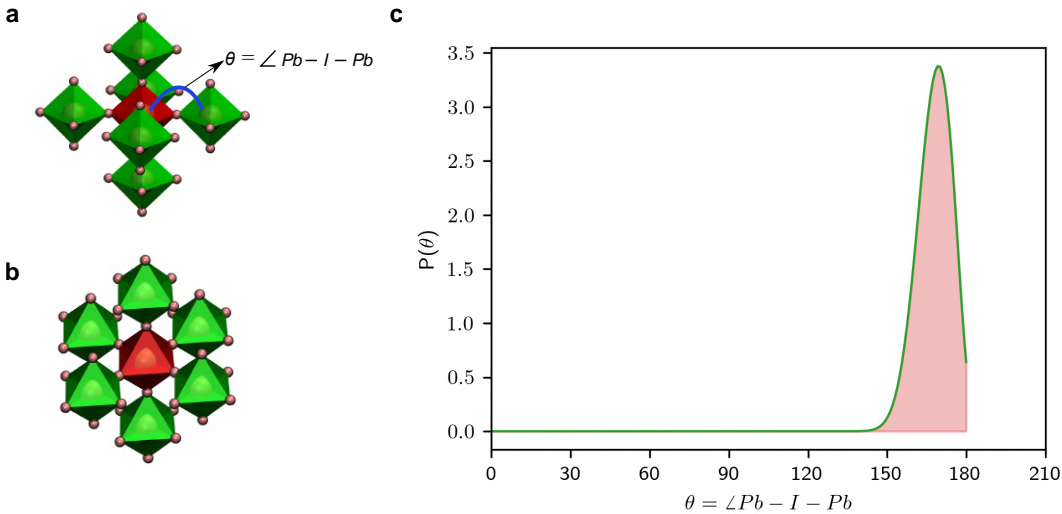


Figure 2.12 – **Perovskite corner-sharing octahedra**. The two snapshots (a) and (b) on the left shows the configurations of perovskite corner-sharing octahedra. The picture (c) on the right is the histogram of Pb-I-Pb angles in the cubic perovskite structure of MAPI.

Perovskite corner-sharing octahedra are calculated in the following steps:

1. Initially I calculate the number of Pb^{2+} that have six fold coordination with the nearest I⁻ in a cutoff of 0.40 nm and mark them as $[\text{PbI}_6]^{4-}$ octahedra.
2. Secondly, I identify the $[\text{PbI}_6]^{4-}$ octahedra that have a coordination number of six with neighbouring $[\text{PbI}_6]^{4-}$ octahedra within a distance cutoff of 0.72 nm. This distance cutoff is taken according to the first coordination sphere of Pb^{2+} ions in the cubic perovskite phase of MAPI as shown in **Fig. A.3**.

3. Then I count the number of those particular octahedra (displayed in red color in **Fig. 2.12a**) that are sharing six I⁻ corners with the neighbours and the angle between Pb-I-Pb (as shown in **Fig. 2.12a**) of these octahedra is more than 150°. The value of this angle is selected from the histogram of Pb-I-Pb angles displayed in **Fig. 2.12c**. This histogram is calculated from a 10ns trajectory of a supercell made of 7x7x7 unit cells of cubic MAPI at 410K and atmospheric pressure in the isothermal-isobaric ensemble as described in the Methods section. These octahedra form the core of the perovskite crystal.
4. The total number of perovskite corner-sharing octahedra are calculated as sum of core (shown in red color in **Fig. 2.12**) and their neighbours (shown in green colors in **Fig. 2.12**).

2.1.9 Experimental Methods

Materials and Chemicals

Lead iodide (PbI₂) (TCI), methylammonium iodide (MAI) (Greatcell Solar), and γ -Butyrolactone (GBL) (Sigma-Aldrich). All the chemicals were used as received.

Spin-coating method (Heterogenous Nucleation)

Three different perovskite precursor solutions including 0.75 M MAPbI₃ (PbI₂ + MAI in 1:1 molar ratio), 0.75 M MAPbI₃ + 0.25 moles of MAI and MAPbI₃ + 0.50 moles of MAI were prepared in GBL. These precursor solutions were heated at 330K for 4 h prior to the deposition. Typically, 50 μ L of precursor solution was spin-coated on the precleaned glass substrates at a speed of 3000 rpm for 30 s with an acceleration of 2000 rpm. The resulting films were subsequently annealed at 373K for 10 minutes under inert conditions.

Growth from Solution (Homogeneous Nucleation)

We prepared three different perovskite precursor solutions such as 1 M MAPbI₃ (PbI₂ + MAI in 1:1 molar ratio), 1 M MAPbI₃ + 0.15 moles of MAI, and 1 M MAPbI₃ + 0.30 moles of MAI dissolved in GBL. To induce homogeneous nucleation and to observe the growth and formation of perovskite single crystals, the resulting solutions were rapidly heated to 430K on a hot plate. This method is commonly known as inverse solubility method. All the experimental variables including concentration, duration and temperature were carefully optimized. Relatively less concentrated solution demanded high temperature (>450K for > 1M solution), and longer duration (1h) to realize the formation of perovskite crystals, and in case of very low concentrated solutions (< 0.6 M), we did not observe the formation of perovskite single crystals, even after prolonged heating at high temperature. Field-emission scanning electron microscope (ZEISS Merlin) with an In-lens detector operating at an acceleration voltage of 3 kV was employed to examine the surface morphology of perovskite films.

2.2 Effect of different solvents

2.2.1 Introduction

A typical perovskite precursor solution consists of lead halide salts, organic or inorganic ammonium salts, dissolved in toxic polar aprotic solvents (e.g., DMF, dimethylacetamide (DMAc), NMP, etc.) and other high-boiling point solvents such as DMSO in high concentration. The high purity raw materials (e.g., PbI_2 , FAI, MAI, etc.) are very expensive and having a short shelf life due to aggregation/degradation. Fabrication of the state-of-the-art PSCs requires a high concentration of lead components [20, 21] to obtain thick, compact, highly crystalline, and pinhole-free photovoltaic devices. Record efficiencies are currently achieved through a combination of coating processes with a highly concentrated precursor solutions. However, spin-coating of high concentration solutions also results in precursor waste generated during processing. This cannot be addressed by lowering the concentration of traditional precursors without also lowering film thickness and PCE. Such high concentration perovskite solutions with high viscosity and low evaporation rates create obstacles to typical scalable perovskite deposition methods [133] in industrial applications, e.g., slot-die coating, spray coating, blade coating, ink-jet printing, roll-to-roll printing as well as industrial-based spin coating, by slowing down the continuous production rate and reducing opportunities for collection and reuse of excess solution. Another downside of concentrated solutions is their short shelf-life due to propensity to aggregate and agglomerate, which increases toxic waste. Therefore, commercialization of PSCs requires to develop an eco-friendly strategy [134] which can minimize the consumption of toxic materials by simultaneously reducing toxic waste during processing steps and by extending the shelf life of perovskite-precursor inks.

2.2.2 Results

Here, I present molecular understanding of a co-solvent dilution strategy which maintains high-quality perovskite films with very low concentration precursor solutions. Considering the precursor solubility and its toxicity, our experimental collaborators choose tetrahydrofuran (THF) as a co-solvent which is considered as a green solvent [135] with very low disability-adjusted life year (DALYs) per kg of substance emitted among typical solvents of PSCs fabrication.

To validate the co-solvent dilution mechanism, I employ a combination of computational methods, including DFT calculations and *ab-initio* MD simulations. I first investigated the solvent-solute interaction by DFT calculations. I calculated the interaction energies of Pb^{2+} with pure DMSO, DMF, THF, and their mixtures for prototypical tetra-coordinated complexes **Fig. 2.13**. I find that the interaction energy of Pb^{2+} with THF is considerably lower than with DMSO and DMF, as illustrated in **Fig. 2.14**. I also find that an intimate mixture with THF can significantly decrease the average interaction energy of Pb^{2+} with the solvent molecules which we anticipate may have implications on the conversion chemistry, that is, if some THF remains

coordinated, the conversion to the perovskite phase might be enhanced. This phenomena is demonstrated via different experiments.

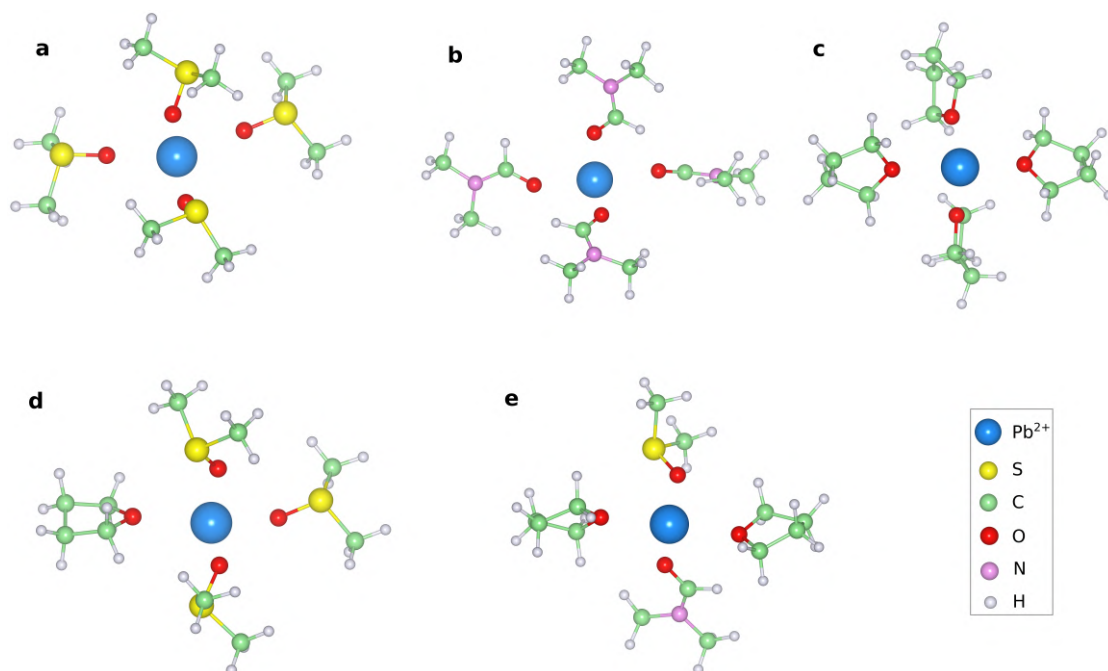


Figure 2.13 – **Prototypical tetracoordinated Pb^{2+} clusters with different solvents:**(a) DMSO, (b) DMF, (c) THF, (d) mixtures of DMSO and THF, and (e) mixtures of DMF, DMSO and THF. All the atoms are labeled with their element symbols. All species are shown with balls and sticks representations.

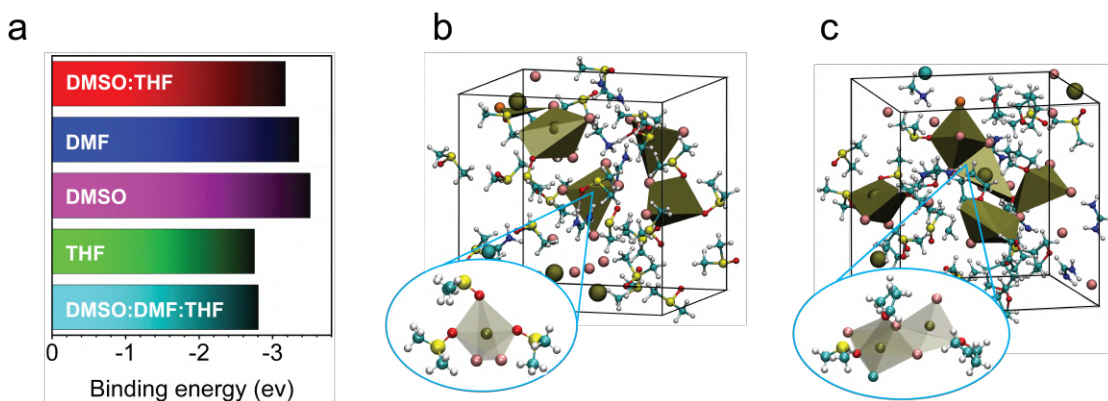


Figure 2.14 – **Solvent-solute interactions:** Average binding energies of Pb^{2+} ions with solvents and their mixtures (evaluated on the tetracoordinated complexes shown in **Fig. 2.13**). b-c Ab initio MD simulations of perovskites precursors in (b) DMSO and (c) THF/DMSO mixture after ~ 15 ps. All species are shown with balls and sticks representations. Pb ions are shown with golden color, I with pink color, Cs with greenish-blue, Br with orange, C with light blue, N with dark blue, O with red, S with yellow and H atoms with white color. In the (b) and (c) panels, lead coordination polyhedra are shown within a 3.6 Å cutoff.

To further understand the finite-temperature solvation effects at the pre-nucleation stage, we performed ~15 ps *ab-initio* MD simulations of solute-solvent mixtures without and with THF. Simulation details are presented in the methods section. To evaluate the effect of co-solvent dilution on the solvent-solute interaction, I use DMSO as a model system in the following discussion. As shown in **Fig. 2.13**, I see that both Pb^{2+} and monovalent cations (FA^+ and MA^+) are highly coordinated with oxygen atoms of DMSO molecules, forming individual small clusters in the case of perovskite precursor in pure DMSO. This can be expected due to the high interaction energies with DMSO (see **Fig. 2.13**).

However, in pure THF, I find that the Pb-I edge-sharing clusters start to form during the MD simulations. This can also explain the experimental observation that precursor complexes are not able to dissolve in pure THF. Interestingly, I find a mixed behavior in the DMSO/THF mixed system with the formation of small mixed Pb-I-solvent clusters and large Pb-I edge-sharing clusters (**Fig. 2.13c**). These smaller solute-solvent clusters can also act as nucleation centers as described in the first part of this chapter. A similar behavior was also observed in the mixtures of DMSO/DMF/THF. One of the main insights from these simulations is that the addition of a co-solvent, like THF, can be used to tune the solvent-solute interaction strength with a direct impact on the subsequent conversion and crystallization process of the perovskite phase. This strategy could substantially reduce the quantity of expensive raw materials in the perovskite precursor ink, and reduces the toxic waste production by minimizing precursor loss during the processing of perovskite films.

2.2.3 Methods

I use the Gaussian 16 program package [136] to perform electronic structure calculations for binding energies. All calculations were carried out at the level of DFT with the Becke-Lee Yang Parr (B3LYP) hybrid functional [137, 138] and with a LanL2DZ[139] basis set for Pb and 6-311G+(d,p) basis set [140] for C, N, S, O, and H atoms. All Pb-solvent clusters are shown in **Fig. 2.13**: (a) Pb with 4 DMSO (noted as DMSO in **Fig. 2.14a**), (b) Pb with 4 DMF (noted as DMF in **Fig. 2.14a**), (c) Pb with 4 THF (noted as THF in **Fig. 2.14a**), (d) Pb with 1 THF and 3 DMSO ((noted as DMSO:THF in **Fig. 2.14a**)) and (e) Pb with 2 THF, 1 DMF and 1 DMSO molecules (noted as DMSO:DMF:THF in **Fig. 2.14a**). First, I performed geometry optimization of different metal (Pb)–organic (solvent molecules) clusters. To determine the solvent-metal interaction energies, I calculated the energy difference between relaxed configurations (shown in **Fig. 2.14**), the same solvent configurations with Pb^{2+} removed and the energy of the isolated Pb^{2+} cation.

Ab-initio MD

I performed constant temperature and constant pressure (NPT) Born-Oppenheimer MD (BOMD) simulations of a homogeneous mixture of different precursor solutions. For all simulations I used a typical mixed cations/halides configuration of 7 Pb^{2+} , 20 I^- , 1 Cs^+ , 1

Br^- , 5 FA^+ , 1 MA^+ in 24 solvent molecules. I performed 5 different precursor simulations of the mixtures of these ions: (a) pure DMF, (b) pure DMSO, (c) pure THF, (d) mixture of THF and DMSO (1:1 mixture) and (e) mixture of THF, DMSO and DMF (3:1:2). All simulations were performed with DFT at the PBE+D3 [141, 142] level with double-zeta basis sets (DZVP-MOLOPT for Pb, I, S, O, C, N, H) [143] and Goedecker–Teter–Hutter (GTH) pseudopotentials [144] with 560 Ry density cutoff. BOMD simulations were performed with the CP2K package [145, 146]. I used a time step of 1 fs and a Nose-Hoover chain thermostat [147–149] was used for controlling the temperature at 300 K and the barostat by Martyna *et al.* [150] was used for pressure control at 1 atm.

2.3 Effect of pseudo-halides

2.3.1 Introduction

In this part, I studied the effect of pseudo-halide anion formate (HCOO^-) that is used as additive from experimental collaborators to control crystallization of FAPbI_3 , to suppress anion-vacancy defects that could be present on grain boundaries as well as surface defects of the perovskite films. The resulting solar cell devices reached a world record power conversion efficiency of 25.6% and had long-term operational stability. This provided an efficient way to eliminate the most abundant and deleterious lattice defects present in metal halide perovskites, therefore providing a facile access to solution-processable films with improved optoelectronic performance.

2.3.2 Results

At first we have to understand if HCOO^- becomes part of bulk FAPbI_3 lattice or not. To this aim, I performed DFT calculations of the formation energy of doped FAPbI_3 , explained in the methods section. I find that the formation energy increases after replacing I^- with HCOO^- anions, therefore concluding that HCOO^- could not be doped into FAPbI_3 . To explore the unique role of HCOO^- anions, I performed *ab-initio* MD simulations of a homogeneous mixture of different ions in the precursor solution (see ethods, **Fig. 2.15**), comprising Pb^{2+} , I^- , HCOO^- , and FA^+ , and found that the HCOO^- anions coordinate strongly with the Pb^{2+} cations.

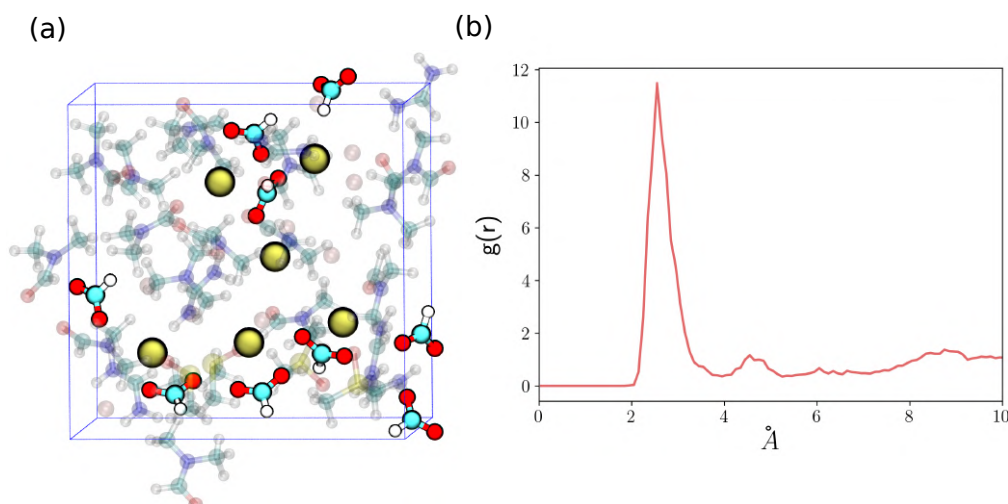


Figure 2.15 – *Ab-initio* MD of precursor solution: (A) MD snapshot showing the coordination of Pb^{2+} ions with HCOO^- anions. To guide the eyes, we only highlight Pb^{2+} and HCOO^- ions. Rest of the ions and solvent molecules are shown with transparent color. All ions are shown with balls and sticks representation. Pb^{2+} ions are shown with yellow balls, oxygen with red balls, carbon with light blue, nitrogen with dark blue, sulfur with light yellow and hydrogen atoms are represented with white balls. (B) The radial distribution function $g(r)$ between the oxygen atoms of HCOO^- around Pb^{2+} over the full *ab-initio* MD trajectory of ~ 11 ps.

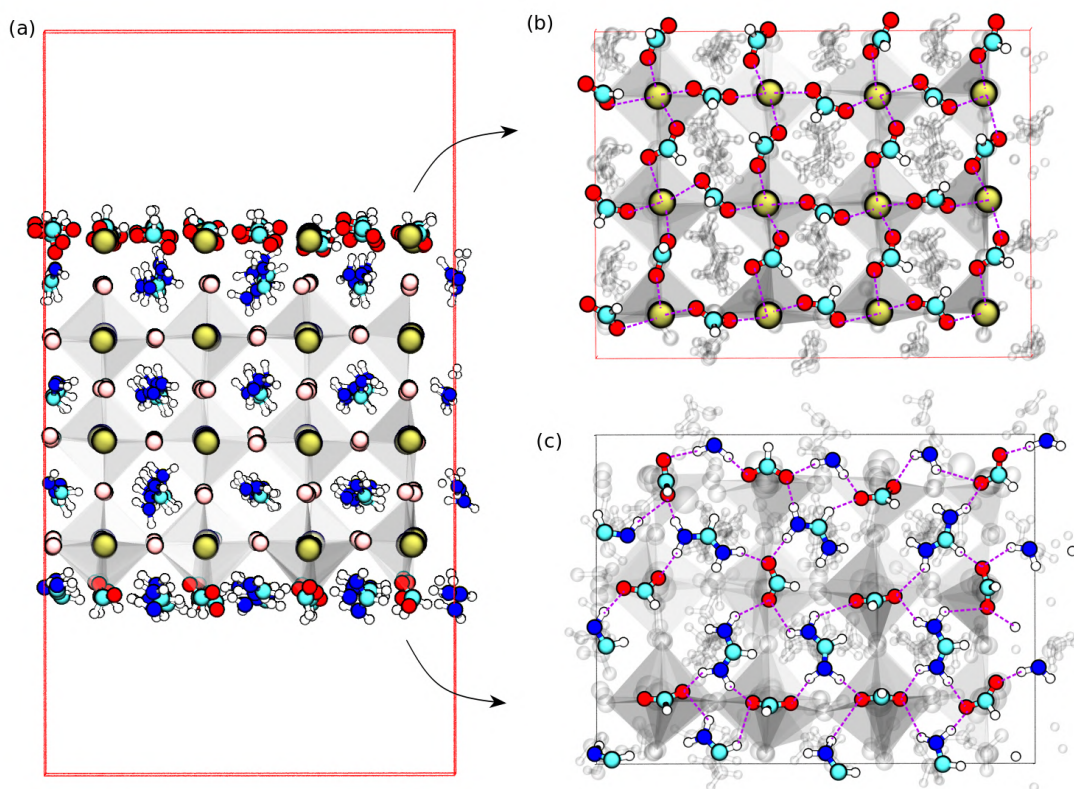


Figure 2.16 – *Ab-initio* MD of formate anions on the surface: (a) Initial configuration with surface iodide replaced by formate anions. All ions are shown with balls and sticks representation. Pb²⁺ ions are shown with yellow balls, iodides with light pink, oxygen with red, carbon with light blue, nitrogen with dark blue and hydrogen atoms are represented with white balls. (b) The top view of the surface atoms on the Pb²⁺ terminated side. (c) The top view of surface atoms on the FA⁺ terminated side. Pb²⁺-HCOO⁻ and FA⁺-HCOO⁻ bonding networks are illustrated with red colored bonds in (b) and with magenta colored bonds in (c).

This strong coordination might help in slowing down the growth process, resulting in larger stacked grains of the perovskite film, which is validated by the *in-situ* thin-film experiments. Compared to the reference film, 2% HCOO⁻-FAPbI₃ film had a slower color change from brown to black. I also performed MD simulations to understand the surface passivation effects of HCOO⁻ anions. (Fig. 2.16 shows a super cell of a α -FAPbI₃ perovskite slab with surface iodides replaced by formate anions. I found that HCOO⁻ anions can form a nexus of hydrogen bonding with FA⁺ ions (shown in (Fig. 2.16c), in agreement with the hydrogen bonding in the FAHCOO crystal structures. In addition, HCOO⁻ anions can also form a bonding network on the Pb²⁺ ion terminated surface because of their strong affinity towards lead (shown in (Fig. 2.16b).

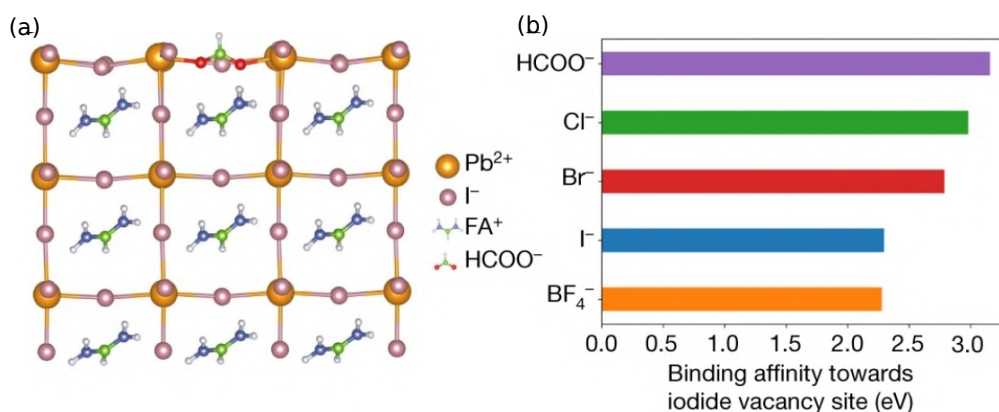


Figure 2.17 – **Binding affinities:** (a) Calculated structure illustrating the passivation of an I⁻ vacancy at the FAPbI₃ surface by a HCOO⁻ anion. All chemical species are shown in balls and sticks representation. (b) The relative interaction strengths of different anions with the I⁻ vacancy at the surface.

Fig. 2.17a shows a HCOO⁻ anion passivating an I⁻ vacancy at the FAPbI₃ surface. I then calculated the binding affinity of the HCOO⁻ anions to the I⁻ vacancies at the surface (**Figs. A.4, A.5, A.6**). I⁻ vacancy defects are the most deleterious defects for the stability of halide perovskites. The energies in **Fig. 2.17b** show that HCOO⁻ has the highest binding energy to I⁻ vacant sites at the interface compared to other anions including Cl⁻, Br⁻, I⁻ and BF₄⁻. Furthermore, I have also calculated the binding energies of formamidinium at the interface with formate anions and with other anions (see methods and **Fig. A.7** and **Fig. A.8**). I found that FA⁺ cations at the interface form a stronger bonding with HCOO⁻ than with the other anions. One can conclude that the HCOO⁻ anion acts as a passivating agent against the formation of vacancy defects (such as I⁻ and FA⁺).

2.3.3 Methods

DFT calculations of the formation energy:

I constructed 12 and 24 formula unit (f.u.) supercells of α -FAPbI₃ and a hypothetical FAPb(HCOO)₃. In order to create the formate analogue of the cubic perovskite phase, I took inspiration from the published literature on formate based perovskites [151]. The FAPb(HCOO)₃ perovskite structure was thus constructed by taking the perovskite structure of formamidinium manganese formate [152] as an initial template and replacing the manganese ion with the lead (Pb₂₊) ion. After this, the structure was relaxed with DFT. The formation energies of both cubic perovskite phases, FAPbI₃ and FAPb(HCOO)₃ were calculated with respect to the precursor phases. For α -FAPbI₃, we chose PbI₂ and FAI as precursors: $E_{\text{Pure}} = E[\text{FAPbI}_3] - E[\text{FAI}] - E[\text{PbI}_2]$, while for FAPb(HCOO)₃ we chose lead formate (Pb(HCOO)₂) and formamidinium formate (FAHCOO) as precursors: $E_{\text{HCOO doped}} = E[\text{FAPb(HCOO)}_3] - E[\text{FAHCOO}] - E[\text{Pb(HCOO)}_2]$. Here, E is the total energy of the respective fully relaxed phases calculated with DFT. The for-

mate based precursor structures were taken from the Cambridge Crystallographic Structural Database [153–155]. All calculations were performed at 0 K, without considering thermal effects. The resulting formation energy of the 144 atoms supercell (12 f.u.) of α -FAPbI₃ is ca. +0.15 eV/f.u., while the formation energies of the 252 atoms supercell (12 f.u.) of cubic FAPb(HCOO)₃ is ca. +0.26 eV/f.u., showing that the formation energy increased by replacing iodide anions with formate anions on the α -FAPbI₃ lattice. Taking into account possible finite size effects, we also compared the formation energies of 24 f.u. supercells of α -FAPbI₃ (288 atoms) and cubic-FAPb(HCOO)₃ (504 atoms) and found that the formation energy increased similarly. Furthermore, I also highlight the fact that the effective ionic radius of the formate anion is 136 pm and smaller than 181 pm for the chloride anion. Therefore, I conclude that the formate anions cannot be doped inside cubic lattice of α -FAPbI₃.

Computational details: I performed variable cell Kohn-Sham DFT calculations of all structures within the Generalized Gradient Approximation (GGA) in the form of the Perdew-Burke-Ernzerhof (PBE) [141] exchange-correlation functional with Grimme D3 dispersion corrections [142]. I used Quantum Espresso [156] with ultra-soft pseudo-potentials for valence-core electron interactions and a plane wave basis set with a 60 Ry kinetic energy cutoff and a 480 Ry density cutoff. The Brillouin zone for the 144 atoms supercell of α -FAPbI₃ was sampled by a 1x1x2 k-point grid, the 108 atoms supercell of FAI by 1x1x2 k-points grid, for the 36 atoms supercell of PbI₂ by 2x2x2 k-points, for the 252 atom supercell of FAPb(HCOO)₃ by 1x2x1 k-point grid, the 144 atom supercell of FAHCOO by 1x2x2 k-points and the 108 atom supercell of Pb(HCOO)₂ by 1x2x2 k-points.

Reference crystal structures for DFT calculations:

CCDC reference: 1861266 – Formamidinium formate (FAHCOO)

CCDC reference: 925259 – Lead formate (Pb(HCOO)₂)

CCDC reference: 1538402 – Formamidinium iodide (FAI)

***Ab-initio* MD of homogeneous mixture of ions at pre-nucleation stage**

I performed constant temperature and constant pressure (NPT) Born-Oppenheimer MD (BOMD) simulations of a homogeneous mixture of ions: 6 Pb²⁺, 9 I⁻, 9 HCOO⁻, 6 FA⁺ in, 4 dimethyl sulfoxide (DMSO) and 16 dimethylformamide (DMF) molecules. All simulations were performed at DFT level (PBE+D3) [141, 142] as described in the methods section. These simulations show that formate ions coordinate strongly with Pb²⁺ ions which might help in avoiding formation of δ -phase at the pre-nucleation stages. Furthermore, this coordination also slows down the growth process which helps in the formation of larger stacked grains.

Computational details: BOMD was performed with the CP2K package [145, 146]. I used a time step of 1 fs, a Nose-Hoover chain thermostat [147–149] for controlling the temperature at 300 K and the barostat by Martyna *et al.* [150] for pressure control at 1 atm. All simulations

used DFT at the PBE+D3 [141, 142] level with double-zeta basis sets (DZVP-MOLOPT for Pb, I, S, C, N, H) [143] and Goedecker-Teter-Hutter (GTH) pseudopotentials [144] with a 560 Ry density cut-off.

***Ab-initio* MD of formate anions on the surface of FAPbI₃**

To further understand the passivation effect of HCOO⁻ anions, I also performed DFT level MD simulations. In the absence of an experimental determined atomistic structure for formate passivated surface or grain boundaries, I started with a plausible passivated structure of FAPbI₃. In this computational experiment, I first created a 684 atoms slab (vacuum on both sides) of α -FAPbI₃ with two-different terminated sides ie. with a cut through a FA-I plane on one side and through a Pb-I plane on the other side. Then we fully replaced the outmost surface layers of I⁻ anions with HCOO⁻ anions. This final configuration is shown in **Fig. 2.16**. In the case that formate anions passivate the iodide defects, these are the two possible configurations that can be present at the perovskite-HTM interface or grain boundaries. For this structure, I performed constant temperature and constant volume (NVT) BOMD simulations. We ran ~12 ps BOMD with a similar setup as defined above.

Passivation effects of HCOO⁻ anions

Comparison of HCOO⁻ passivation strength with other anions at I⁻ vacancy on surface: To understand the benefits of the surface passivation with formate anions, I created an I⁻ vacancy (only one) at the surface and compared the binding affinities of different anions to this vacant site. I selected I⁻, Cl⁻, Br⁻, BF₄⁻ and HCOO⁻. At first, different anion passivated structures were relaxed at the DFT level with variable-cell optimization as described in the following computational details. All of the DFT relaxed slabs are shown in **Fig. A.4**. To calculate the binding energies the adsorbed anions from surface were moved in the z-direction as shown in **Fig. A.4(f)**. DFT energies were calculated for each structure along this de-sorption profile. The resulting energy profiles were used to estimate the relative binding strengths shown in **Fig. 2.17b** were calculated relative to the energy of the respective original (fully bound) configurations.

Computational details First, I constructed a 324-slab structure of cubic phase FAPbI₃ with more than 15 Å empty space in the z-direction. Four more different structures were constructed from this slab by replacing one I⁻ from surface with four different anions: Br⁻, Cl⁻, BF₄⁻ and COOH⁻ on the FA-I and Pb-I terminated surfaces of the slab. DFT calculations are performed with a similar setup as described above with a plane wave basis set of 60 Ry kinetic energy cutoff for the wavefunctions and 480 Ry density cutoff. The Brillouin zone was sampled by a 2x2x1 k-points for every structure. There is a possibility of I⁻ vacancy passivation (by Br⁻, Cl⁻, BF₄⁻ and HCOO⁻) on both Pb-I terminated surfaces, shown in **Fig. A.4** and FA-I terminated surfaces, shown in **Fig. A.5**. The binding affinities shown in **Fig. 2.17b** are calculated on the Pb-I interfaces at z-distance ~4Å.

Systematic comparison of binding energies of passivated surface To further understand effects of the surface/grain boundaries passivation with HCOO^- anions, I also performed a systematic comparison of the desorption energies of FA^+ cations from surfaces passivated with different anions: I^- , Cl^- , Br^- , BF_4^- and HCOO^- . To this end, different anion passivated structures were constructed and subsequently relaxed with DFT level variable-cell optimization as described above. I constructed a 240 atoms ($2 \times 2 \times 5$) slab of cubic phase FAPbI_3 with more than 15 Å empty space in the z-direction. Four more different structures were made from this slab by replacing surface I^- with four different anions: Br^- , Cl^- , BF_4^- and COOH^- on the FA-I terminated interface of the slab as depicted in **Fig. A.6**. All of the DFT relaxed slabs are shown **Fig. A.7**. Then one FA^+ cation from surface was selected and moved to the increasing distance along z-direction. DFT energies were calculated for each structure along this desorption profile. The resulting energy profiles (at distance $\sim 4\text{Å}$) shown in the **Fig. A.8** were calculated relative to the energy of the respective original (fully bound) configurations.

3 Phase transitions in the two-step process

This chapter was adopted from the following articles:

Postprint version of the article: P. Ahlawat, A. Hinderhofer, E. A. Alharbi, H. Lu, A. Ummadisingu, H. Niu, M. Invernizzi, S. M. Zakeeruddin, M. I. Dar, F. Schreiber, A. Hagfeldt, M. Graetzel, U. Rothlisberger and M. Parrinello, “A combined molecular dynamics and experimental study of two-step process enabling low-temperature formation of phase-pure α -FAPbI₃.” *Science Advances* 7, no. 17 (2021): eabe3326. (doi: 10.1126/sciadv.abe3326)

My contribution: Conceived, conceptualized and coordinated the research. Designed, performed and analyzed all simulations. Conceived and designed experiments with Dr. Haizhou Lu and Dr. Essa A. Alharbi. I wrote the manuscript.

Postprint version of the article: H. Lu, Y. Liu, P. Ahlawat, A. Mishra, W. R. Tress, F. T. Eickemeyer, Y. Yang, F. Fu, Z. Wang, C. E. Avalos, B. I. Carlsen, A. Agarwalla, X. Zhang, X. Li, Y. Zhan, S. M. Zakeeruddin, L. Emsley, U. Rothlisberger, L. Zheng, A. Hagfeldt, M. Graetzel, “Vapor-assisted deposition of highly efficient, stable black-phase FAPbI₃ perovskite solar cells.” *Science* 370, no. 6512 (2020). (doi: 10.1126/science.abb8985)

My contribution: Conceived, conceptualized, designed, performed and analyzed all simulations. I wrote the simulations part.

3.1 Sequential deposition

It is well established that the lack of understanding the crystallization process in two-step sequential deposition has a direct impact on efficiency, stability and reproducibility of perovskite solar cells. Here, I try to understand the solid-solid phase transition occurring during two-step sequential deposition of methylammonium lead iodide and formamidinium lead iodide. Using metadynamics, DFT and experiments, we reveal the microscopic details of this process. I find that the formation of perovskite proceeds through intermediate structures and report polymorphs found for MAPbI₃ and FAPbI₃. From simulations, we discover a possible crystallization pathway for the highly efficient metastable α -phase of FAPbI₃. Guided by these simulations, we perform experiments that result in the low temperature crystallization of

phase-pure α -formamidinium lead iodide.

3.1.1 Introduction

Two-step deposition[30] is one of the main experimental techniques used to fabricate highly efficient and stable PSCs [157, 158]. In this process, lead iodide (PbI_2) is first deposited and then converted to perovskite by adding halide salts of monovalent cations such as methylammonium iodide (MAI) and formamidinium iodide (FAI)[29]. This process offers several advantages for the industrial-scale fabrication[159–161] of larger modules over the single-step spin-coating technology, which is limited to smaller devices. However when scaling up, maintaining reproducible high performances and long-term stability is difficult. These problems arise mainly from the lack of control over the fabrication process [162, 163]. Therefore, it is essential to understand at the atomic level the mechanism of halide perovskites crystallization.

Among the several perovskites of interest, I study here the two-step fabrication of MAPbI_3 and FAPbI_3 . The former is a well-studied system on which many experiments have been performed. The latter FAPbI_3 , is a compound that in its α - FAPbI_3 polymorph has several attractive features like a ~ 1.45 eV bandgap, high charge carrier mobility and superior thermal stability. The practical application of α - FAPbI_3 has been hampered by the fact that the α -phase is metastable and the thermodynamic phase transition requires high temperatures at $\sim 150^\circ\text{C}$. The main result of this paper is the discovery of a low temperature pathway to the fabrication of α - FAPbI_3 . This has been made possible by a combined experimental and theoretical effort that has uncovered the microscopic details of the crystallization process.

Previous experimental research [164–173] on MAPbI_3 has revealed that the two-step process occurs via intercalation of the MA^+ cations in the PbI_2 layers followed by a transformation to the perovskite structure via intermediate phases. However, these experiments could not resolve the nature of intermediate phases nor elucidate the underlying atomistic mechanism. In order to fill in the details that experiments cannot resolve and obtain an understanding of the microscopic transformation mechanism, I have performed a molecular dynamics investigation. Since the time scale involved in the fabrication process is too large, we have made use of an enhanced sampling technique. In particular, I have used WTMetaD. This method allows simulating processes that take place on an extended time scale with affordable computing resources.

In the following sections, I show that the picture of the initial intercalation followed by a sequence of intermediates states is correct. I perform WTMetaD simulations and found that transformation from the intercalated initial structure to the final perovskite arrangement takes place via a sequence of intermediates. These theoretical results are in line with present and past experiments [96, 174–177]. The highly satisfactory agreement between theory and experiments in the case of MAPbI_3 encouraged to investigate theoretically whether a similar process was operational also for the much less studied α - FAPbI_3 . Simulations indeed discovered that a two-step formation of α - FAPbI_3 is possible at lower temperatures. We perform

X-ray and thin-film experiments that confirmed the outcome of the simulations and enabled the low-temperature formation of phase-pure α -FAPbI₃ thin films.

3.1.2 WTmetaD simulations

To begin with, I start from the plausible hypothesis that monovalent cations (MA^+) intercalate between the edge-sharing layers of Pb-I octahedra in PbI₂ (**Fig. 3.1a**) and form a quasi-2D layered structure which is similar to the post-perovskite structure[178]. I manually construct such a structure by placing MA^+ ions in between the layers of PbI₂ (**Fig. 3.1b**). The remaining iodide (I^-) from MAI is placed on the Pb-I octahedra to have a final charge-neutral layered MAPbI₃ structure. This model is based on experimentally reported intercalated PbI₂ structures [179, 180]. I verify the stability of this structure by carrying out a variable cell enthalpic optimization with both classical MD simulations and DFT. From both techniques, I find that the structure shown in **Fig. 3.1b** is stable. Details are presented in the Methods section.

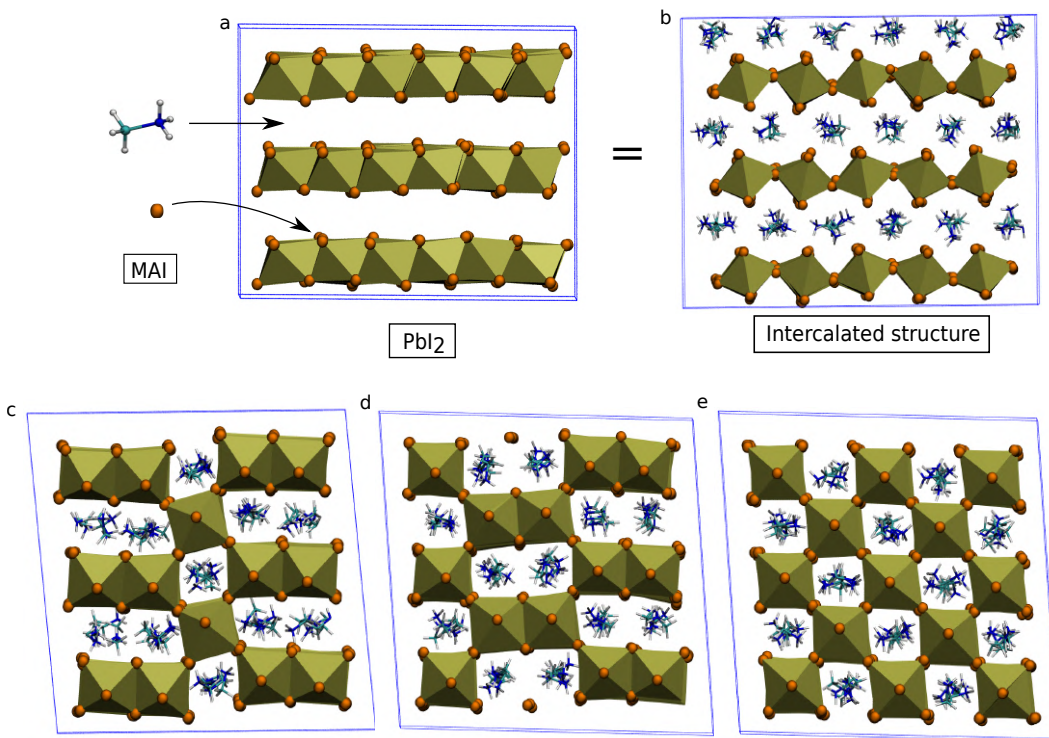


Figure 3.1 – Phase transition via intermediate phases: Images a and b show the intercalation process. Images (b) to (e) display the phase transition from quasi-2D intercalated structure (b) to perovskite phase of MAPbI₃ (e). Pb-I complexes are shown as golden polyhedra with Pb^{2+} in the center and I^- as dark orange balls on the corners. MA^+ cations are shown with balls and sticks with carbon as light blue, nitrogen as dark blue and hydrogens being white. Similar structures have been observed for other materials such as MgSiO_3 , CsIrO_3 , AgTaS_3 , NaMgF_3 , MgGeO_3 , UFeS_3 [178].

Furthermore, calculate the powder diffraction pattern of the DFT relaxed intercalated structure. I find that the first peak of PbI_2 at $\sim 12.7^\circ$ shifts to $\sim 11.4^\circ$ for the intercalated structure, see **Fig. 3.2**. This observation is consistent with the previously reported XRD experiments on two-step deposition [181].

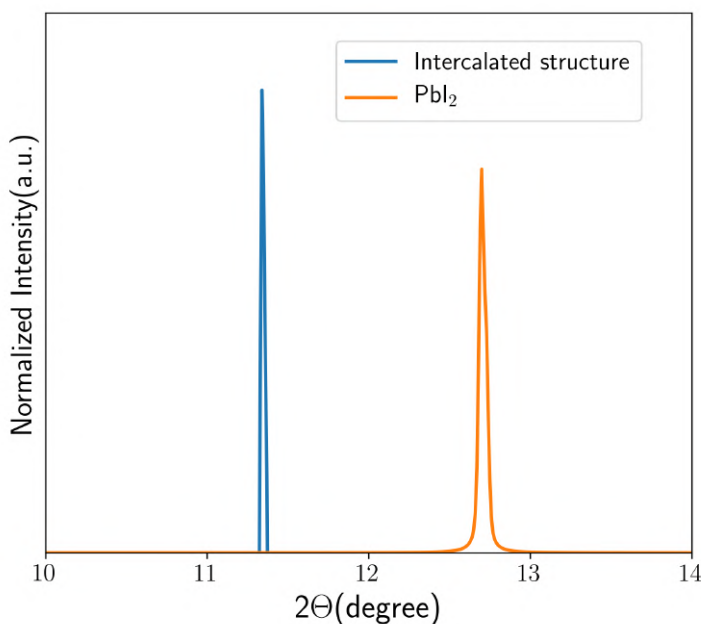


Figure 3.2 – **Simulated XRD spectra of intercalated phase and PbI_2** : Comparison of the first peak of powder diffraction patterns of DFT-D3 optimized PbI_2 and intercalated structure. We use VESTA software to calculate the powder diffraction patterns.

I proceed with the WTMetaD simulations of the transformation of the intercalated MAPbI_3 to the perovskite. I prepare two different size supercells of the intercalated structure with 32 and 108 formula units of MAPbI_3 , respectively. With these supercells, I perform WTMetaD simulations as outlined in the Methods section. These simulations are done at different temperatures ranging from 300 to 420K corresponding to typical experimental conditions. For both supercells, I successfully observe the transformation of the starting quasi-2D layered intermediate structure to the 3D corner-sharing perovskite. Interestingly, I find that the phase transition from quasi-2D to 3D perovskite proceeds through distinct intermediary structures as shown in **Fig. 3.1a** to **Fig. 3.1e**. This observation can be explained by Ostwald's step rule which states that metastable structures are formed as intermediate phases before the formation of the thermodynamically stable phase. I also compute the free energy profile to demonstrate the metastability of these intermediates as compared to final perovskite. Typical free energy profiles are shown in **Fig. 3.3** and **Fig. 3.4**. From these figures: one can see that the intermediate phases are formed by rotating PbI_6 octahedra over the planes of PbI_2 (along

the axis of the Pb-Pb edge-shared octahedra). This is a general pathway to the formation of intermediate structures. In the larger supercell more PbI_6 octahedra are required to rotate for complete formation of the perovskite structure which leads to formation of more intermediate phases.

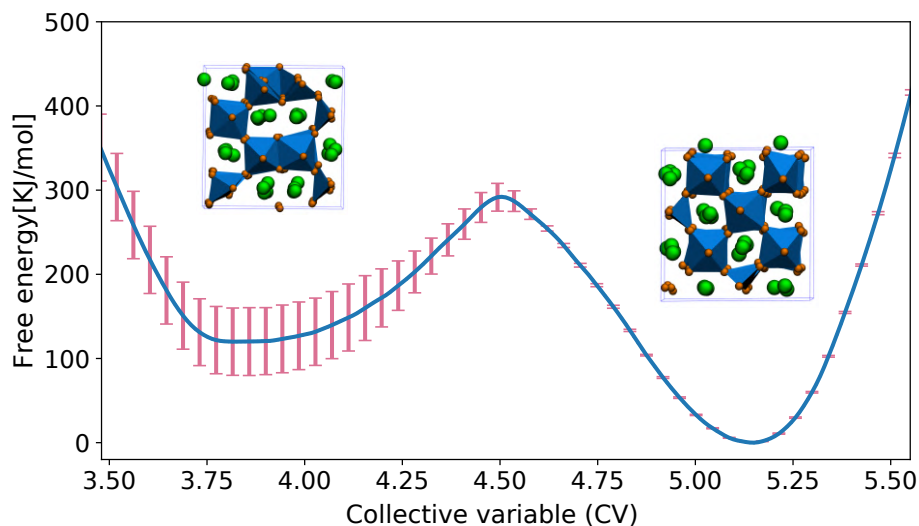


Figure 3.3 – **Free energy profile for smaller supercell:** Free energy profile between intermediate phase and full perovskite structure for smaller supercell. The error bars show the standard error of the free energy difference at each CV value in the final free energy profile.

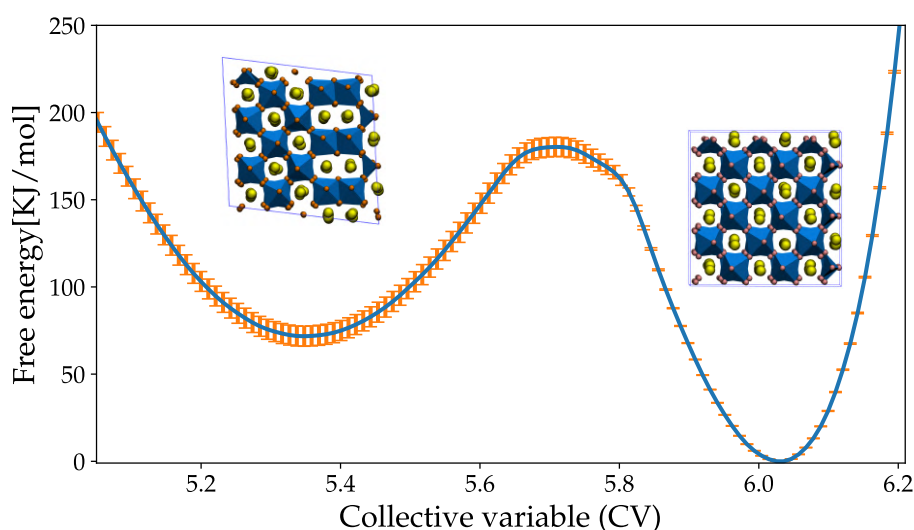


Figure 3.4 – **Free energy profile for larger supercell:** Free energy profile between intermediate phase and full perovskite structure for larger supercell. The error bars show the standard error of the free energy difference at each CV value in the final free energy profile.

I quantify this with the evolution of the first peak ($q \approx 10 \text{ nm}^{-1} = 2\theta \approx 14.1^\circ$) of the Debye structure factor (S_{Pb1}) of Pb^{2+} ions in cubic perovskites, detailed in the Methods section. **Fig. 3.5** shows the evolution of S_{Pb1} for the larger supercell while results for the smaller supercell are shown in **Fig. 3.6**.

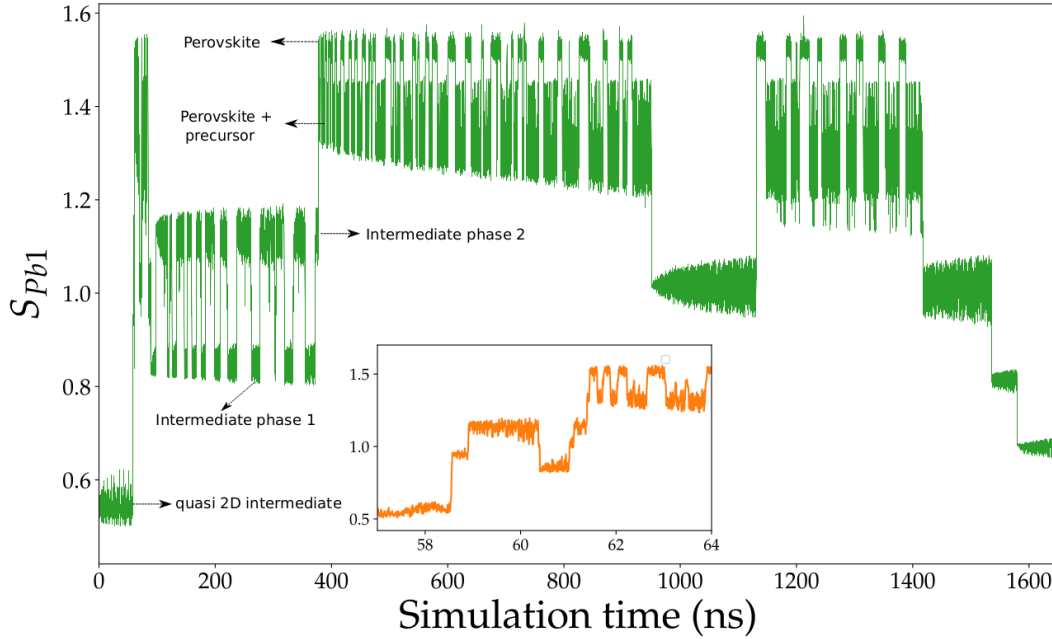


Figure 3.5 – **Structure factor for larger cell:** Evolution of first peak of structure factor of Pb^{2+} ions (S_{Pb1}) with WTmetaD simulation at 370K. Inset is a zoom of S_{Pb1} for the first transition from quasi-2D to 3D.

Moreover, I further explore the free energy landscape and find a variety of different polymorphic structures. I outline all of the observed phases in **Fig. 3.7**. By performing variable cell enthalpic optimization with DFT, we find that all of the structures are stable. This polymorphic behavior in halide perovskites is related to the existing polytypism in PbI_2 [182, 183], which also gives rise to these intermediates in crystallization. Many of these polymorphs have a high probability of forming during crystallization of other halide perovskite systems and some of these structures have been already identified experimentally. [174–177]

Encouraged by the results for MAPbI_3 , I proceed to study the phase transition of FAPbI_3 . Here, the main practical challenge is to find the possible pathways for crystallization of the pure samples of the photoactive α phase. I attempt to solve this problem by first performing simulations and then experiments based on insights from the simulations. I carry out simulations similar to the above reported approach for MAPbI_3 . First, I construct a quasi-2D PbI_2 structure intercalated with FA^+ , similar to the structure in **Fig. 3.1b**.

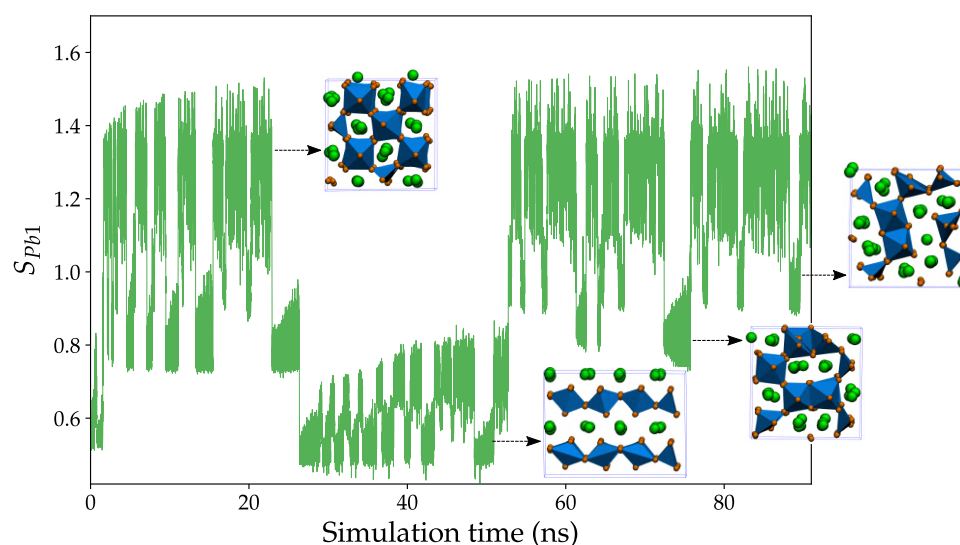


Figure 3.6 – **Structure factor for smaller supercell:** Here we show metadynamics time evolution of first peak of structure factor for Pb^{2+} ions with their corresponding observed structures. Pb-I complexes are shown as blue polyhedra with Pb^{2+} in the center and I^- on the corners. I^- is shown as pink spheres. To guide eyes, monovalent cations are represented with green spheres.

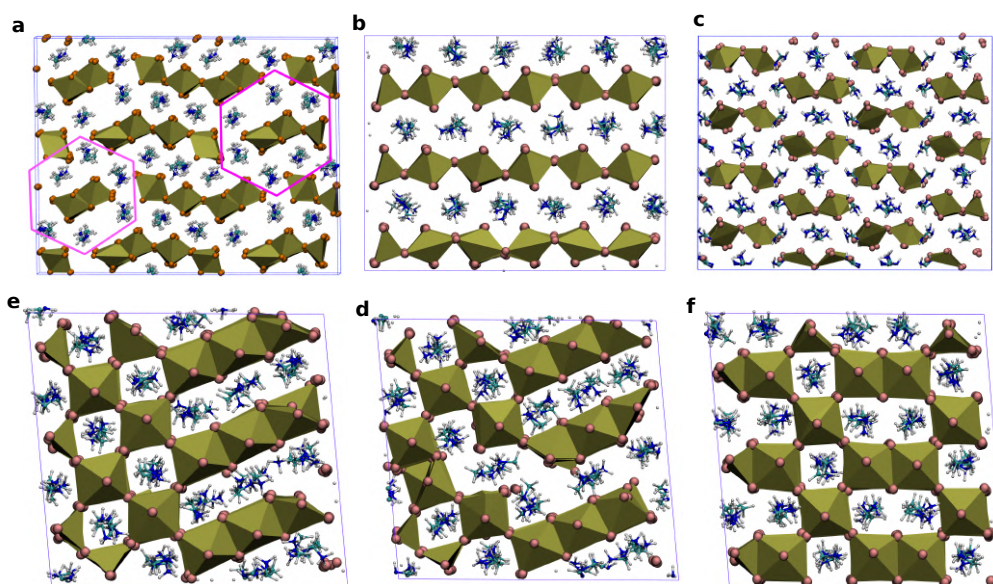


Figure 3.7 – **Different polymorphs:** Pb-I complexes are shown as golden polyhedra with Pb^{2+} in the center and I^- on the corners. Free I^- is shown as pink spheres. MA^+ and FA^+ cations are shown with ball and sticks with carbon as light blue, nitrogen as dark blue and hydrogens being white.

I depict this structure in **Fig. 3.8b**. I perform WTMetaD simulations of two different size supercells of FAPbI_3 , again, as in the case of MAPbI_3 , in both cases, I successfully observe the phase transition to the perovskite structure of FAPbI_3 . Remarkably, these simulations reveal a direct path (from the intercalated PbI_2) to the formation of the metastable phase of α - FAPbI_3 without the need for a high-temperature induced transformation via the δ phase. In particular, these findings suggest that α - FAPbI_3 can be formed at lower temperatures from an initial quasi-2D structure.

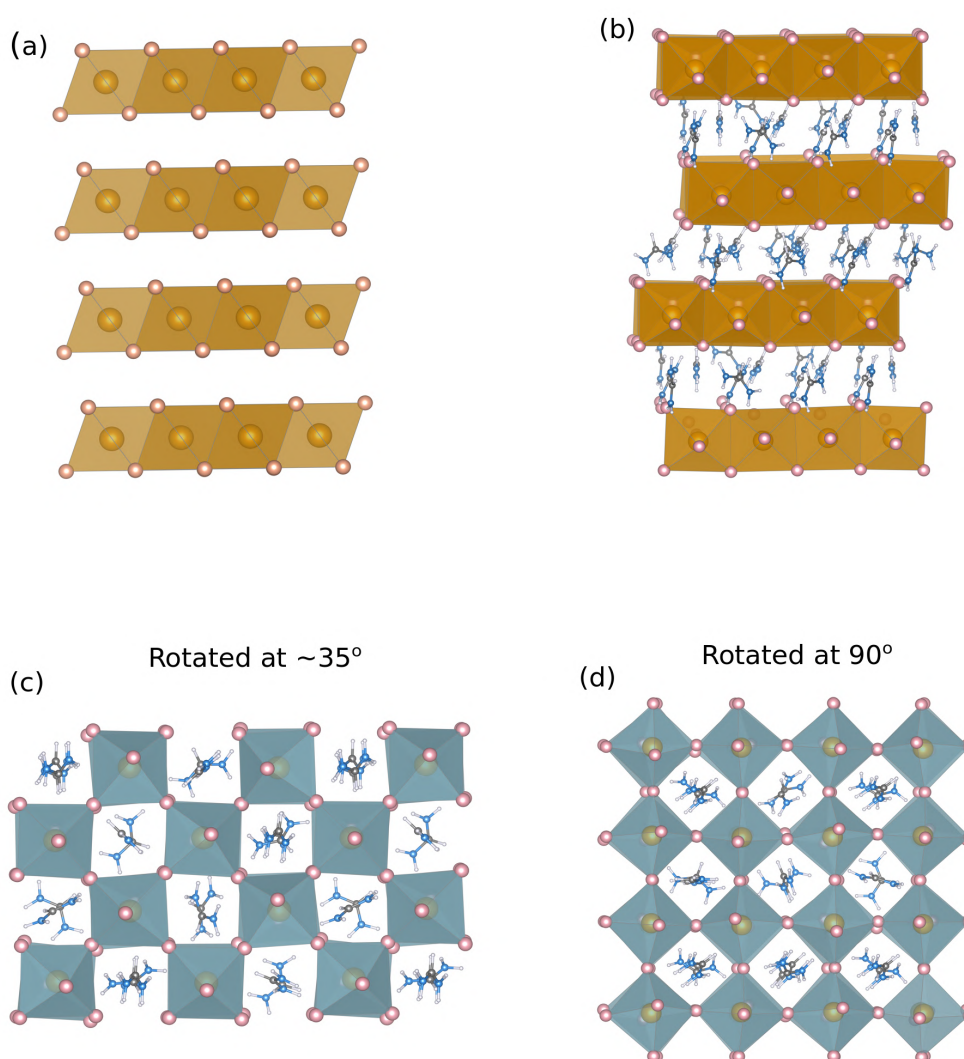


Figure 3.8 – Illustration of crystal structures from two-step FAPbI_3 simulations: Figure (a) is the crystal structure of PbI_2 (b) shows intercalated structure (c and d) are the crystal structures of FAPbI_3 perovskite oriented at 35° and 90° , respectively.

3.1.3 Experiments

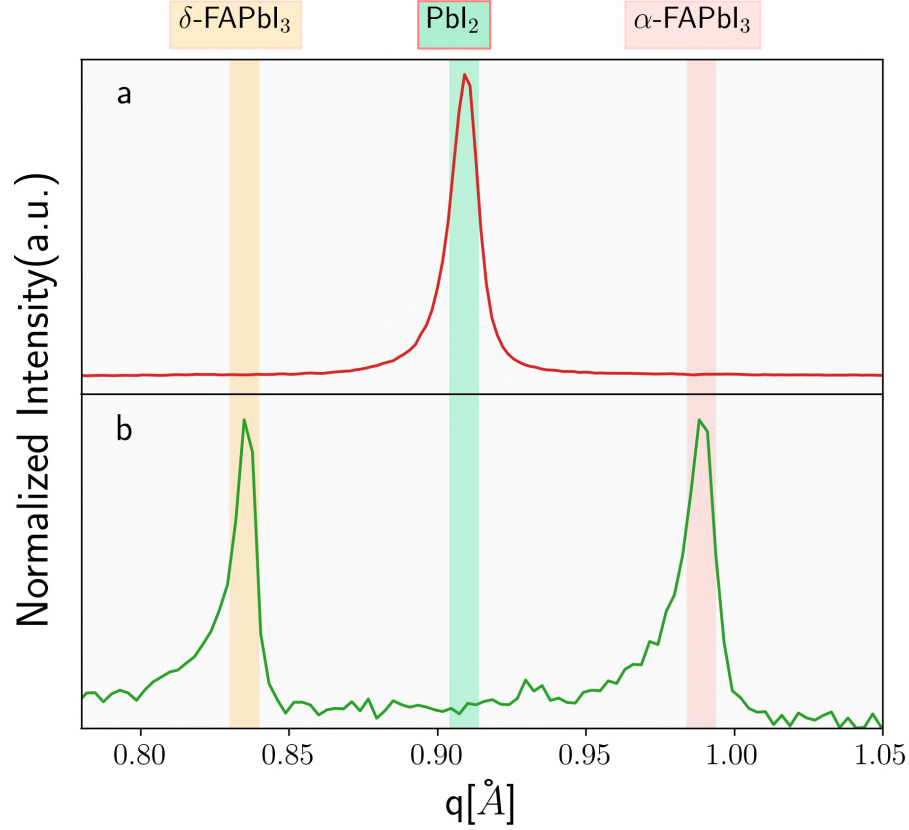


Figure 3.9 – **XRD spectra of FAPbI₃ samples at room temperature:** Top panel is the XRD spectrum of PbI₂ deposited film and bottom panel shows the corresponding data after the FAI loaded onto PbI₂ at room temperature

Now we test our simulation results against the experiments. We directly attempt sequential deposition of α -FAPbI₃ at room temperature. First, we deposit a layer of PbI₂ and directly dip it in FAI solution. XRD measurements on this film (**Fig. 3.9**), show that PbI₂ is partially converted to α -FAPbI₃. I expect this from insufficient diffusion of large FA⁺ cations in a highly compact PbI₂ film. I design a computational experiment to explain this observation. I remove parts of FAI from the FAI-intercalated PbI₂ and perform DFT based variable-cell enthalpic relaxation of this structure. I observe that FAI removed pieces of intercalated structure turn into face-sharing Pb-I octahedra, thus forming characteristic motives of the δ -FAPbI₃. I depict this whole process in **Fig. 3.10**

We further scrutinize our simulations and compare the orientational changes in the metadynamics trajectory with *in-situ* GIWAXS data. During the initial stage of the phase transition from PbI₂ to perovskite structure, GIWAXS experimental results in the published article [184]

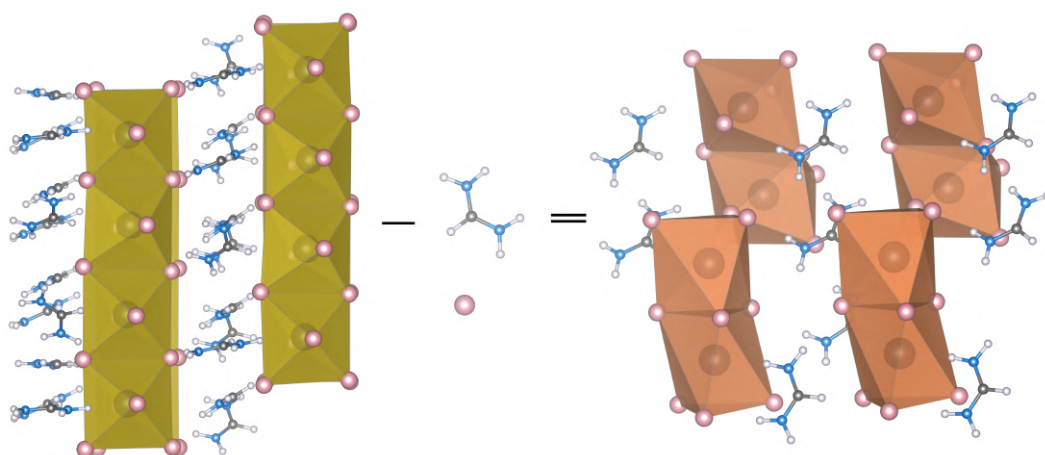


Figure 3.10 – **From edge-sharing to face-sharing:** This figure shows that removing FAI from the intercalated structure leads to the formation of face-sharing octahedra. Left figure is the DFT relaxed intercalated structures and right hand side shows the DFT relaxed structure after removal of one stoichiometric unit of FAI.

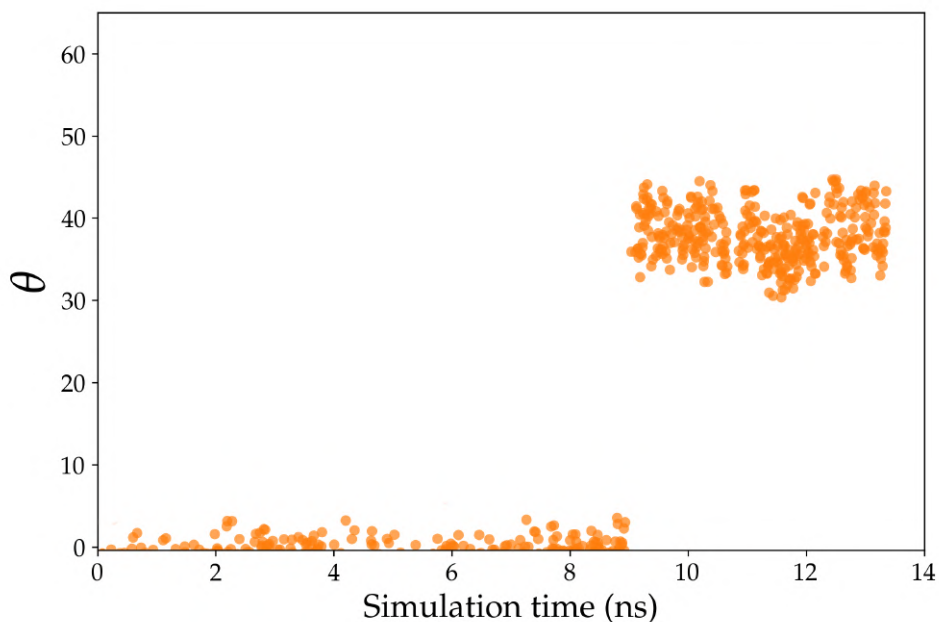


Figure 3.11 – **Analysis of WTmetaD trajectories:** This figure shows the angle between 001 plane of PbI_2 and metadynamics trajectory of the formation of 100 plane α -FAPbI₃.

show that the first perovskite Bragg reflection (001 in cubic notation, 002/110 in tetragonal notation) is oriented at a polar angle of $\sim 35^\circ$, defining 0° as the horizontal plane direction of 001-PbI₂. This orientation corresponds to the 111 plane (cubic notation) being parallel to the substrate plane. Similar to these experiments, I calculate the initial orientation of perovskite structure in our simulations. I take 0° as the horizontal plane direction of 001-PbI₂ intercalated structure. I find a similar tilt of $\sim 35^\circ$ of the 001 plane. A pictorial representation of this whole process is shown in **Fig. 3.8** and **Fig. 3.11**. We conclude that our simulations are consistent with experimental observations, since the orientational changes of the structure during the crystallization are well reproduced.

3.1.4 Thin-film experiments on formation of phase-pure α -FAPbI₃

In this section, we aim to utilize the above-presented insights to make phase pure thin-films of α -FAPbI₃. Based on the intercalation of monovalent cations, we expect that the formation of FAPbI₃ would strongly depend on the microstructure of initially deposited PbI₂ thin films. To understand this effect, we design three different experiments with tailored crystallinity and porosity of PbI₂. Experimental details are provided in the Methods section. **Fig. 3.12a**, **Fig. 3.12b**, and **Fig. 3.12c** are scanning electron microscopy (SEM) images of the three PbI₂ films, showing the top-view surface morphologies. The porosity of these films is in increasing order from first to third. From **Fig. 3.12c**, one can see that the third film is highly porous compared to the others. Next, we use only FAI and perform an identical sequential deposition procedure for their conversion to FAPbI₃, see experimental details in the Methods section. **Fig. 3.12d**, **Fig. 3.12e**, and **Fig. 3.12f** show the XRD patterns of the final FAPbI₃ films. We observe the formation of cubic(α)-phase of FAPbI₃ in all cases. However, we find that the significant amounts of unconverted PbI₂ are present in the first two cases (**Fig. 3.12d** and **Fig. 3.12e**), whereas conversion to FAPbI₃ from a highly porous film (the third case) does not contain any detectable amount of PbI₂ and δ -FAPbI₃, evident from **Fig. 3.12f**. From this study, we can conclude that a highly porous thin-film of PbI₂ leads to the formation of a kinetically stable phase-pure α -FAPbI₃. We calculate the kinetic barrier between α -FAPbI₃ and δ -FAPbI₃. These simulations are explained in the next section of this chapter.

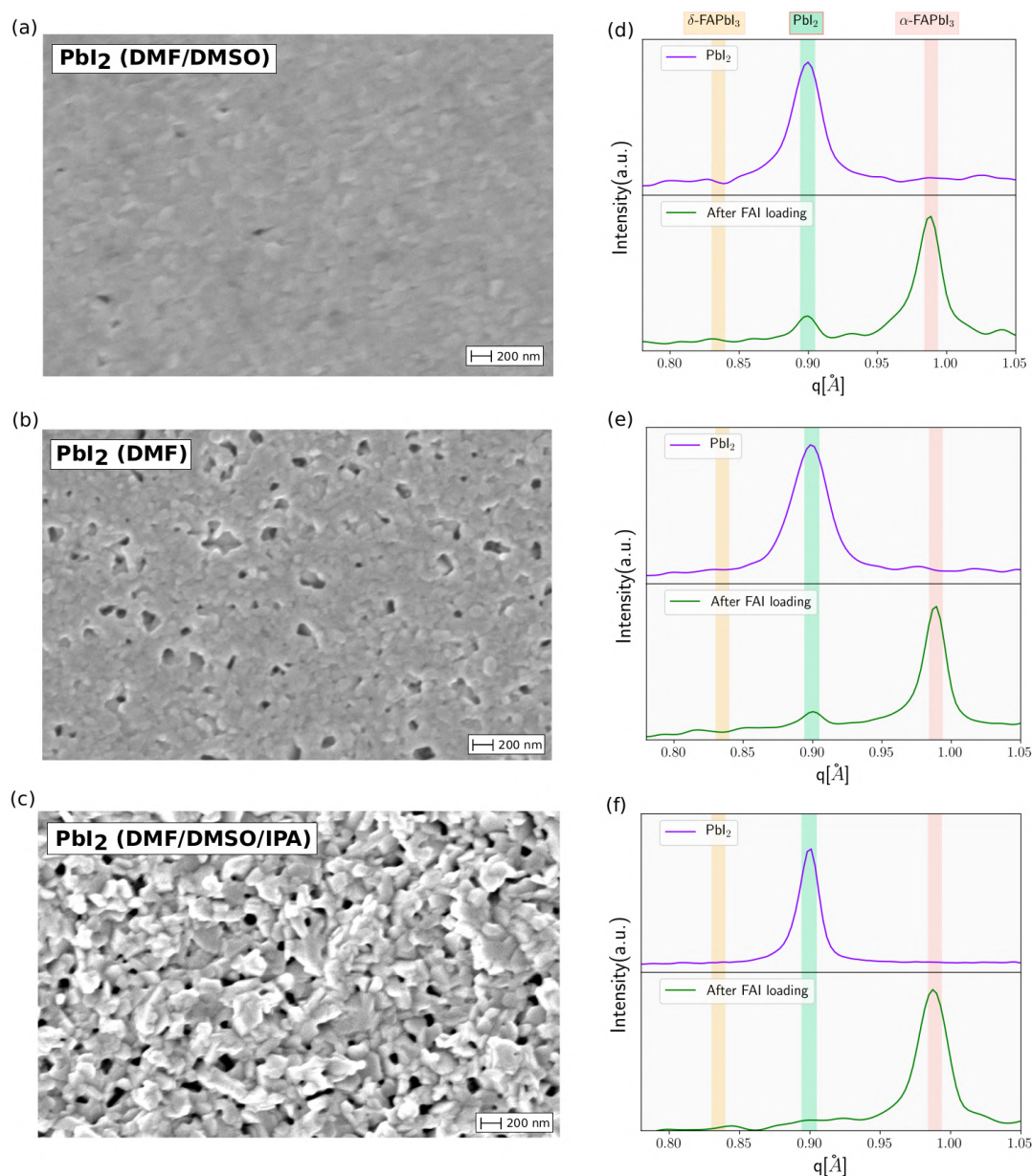


Figure 3.12 – **Thin-film experiments of sequential deposition of FAPbI₃**: Figures (a) to (c) are the SEM images showing the surface topography and figures (d) to (e) are the corresponding XRD spectra of thin-films before and after conversion to FAPbI₃

3.1.5 Discussion

I point out that the phase transition from a quasi-2D to 3D perovskite structure via rotation of Pbl₆ octahedra is a general pathway to form the perovskite structure. This theoretical result can be useful as such a quasi-2D phase can be tailored with additives to synthesize high-quality and stable α-FAPbI₃. One example are anion additives such as chloride, which is widely known

to modify the crystallization process and has become a commonly used additive to make high efficiency α -FAPbI₃ based solar cells. Recent XRD[185] and cryo-electron microscopy (cryo-EM)[186] experiments have shown that chloride induces a quasi-2D like intermediate phase which can help in nucleation of α -FAPbI₃. Therefore, the current theoretical approach presented here can be applied to unravel the effects of different additives. Moreover, the reverse phase transition from 3D to quasi-2D might also be present during degradation leading to PbI₂.

3.1.6 Conclusions

By using WTmetaD, I explore the phase transition paths in the two-step deposition of halide perovskites. Combining simulations and experiments, we reveal the intricate details of the phase transition of MAPbI₃ and FAPbI₃. I find a low temperature crystallization pathway for the α -FAPbI₃. Our combined experimental and simulation study will help in designing better industrial scale processing techniques for MAPbI₃ and FAPbI₃. In the end, I point out that other Raman studies[180, 187] have also demonstrated the PbI₂ intercalation with other organic molecules such as ammonia, ethylamine (C₂H₅NH₂), butylamine (C₄H₉NH₂), and even larger ones such as cyclohexenyl ethyl ammonium (C₆H₉C₂H₄NH₃⁺). Therefore, combined experimental and simulations study can be extended to study the formation of other systems such as lower-dimensional (2D) perovskites as well.

3.1.7 Methods

I use a fixed point charge model for MAPbI₃ [188] with 1.0 nm cutoff for nonbonded interactions. I take the PbI₂ parameters from this force field and prepare the force fields for FAPbI₃ by mixing rules. In variable cell isothermal-isobaric simulations, this force fields gives stable delta and cubic phases and can also reproduce all other experimentally known 4H and 6H polytypes of FAPbI₃. Electrostatics are treated with the particle-particle-particle-mesh Ewald method and the SHAKE algorithm[189] is used to constrain covalent bonds to hydrogen. All systems are simulated with the Large-scale Atomic/Molecular Massively Parallel Simulator(LAMMPS) code (31 Mar 2017)[127]. I first minimize all systems with a conjugate gradient algorithm keeping a tolerance of maximum force of 10⁻³ kcal/molÅ. After minimization, I perform a 100ps NVT equilibration run. All production run simulations presented in this work were carried out in the isothermal-isobaric ensemble with a velocity re-scaling thermostat [128] of relaxation time 0.1 ps and a Parrinello-Rahman barostat [129]. All WTmetaD simulations are performed with PLUMED 2.4 [130].

DFT calculations

I use Quantum Espresso [156] for geometry optimization with Generalized Gradient Approximation (GGA) of Kohn-Sham DFT, namely the Perdew-Burke-Ernzerhof (PBE) functional

[141] with Grimme-D3[142] dispersion corrections for van der Waals interactions. In all DFT calculations, I use ultra-soft pseudo-potentials with a plane wave basis set of 60 Ry kinetic energy cutoff and 480 Ry density cutoff.

Collective variables

In this study I use an experimentally measurable quantity, the structure factor [190] as a collective variable (CV). In particular we employ the Debye form [191] of structure factor ($S(q)$):

$$S(q) = 1 + \frac{1}{N} \sum_{i=1}^N \sum_{j \neq i}^N \frac{\sin(qr_{ij})}{qr_{ij}} \quad (3.1)$$

In this equation the sum is done over neighbors of atom i which are contained in a sphere of radius r_c . As previously done a damping function is added to remove the termination effects from a finite cutoff. Further details are provided in reference[190]. Contrary to previous applications, perovskites are multi-component systems. In order to deal with this, I use a linear combination of the first two peaks of the structure factors of individual species Pb^{2+} and MA^+ , as shown in **Fig. 3.13**. I design this strategy based on two main factors: (a) Pb^{2+} are the heaviest atoms and contribute most to XRD spectra and (b) our previous simulations [192] have revealed that the monovalent cations (MA^+ and FA^+) play an important role in the crystallization process of halide perovskite. Furthermore, these are also the peaks which are assigned to identify perovskite formation in GIWAXS experiments, see **Fig. 4**. MA^+ and FA^+ cations are represented with the center of C-N bond similar to our previous study [192].

$$CV = S_{\text{Pb1}} + S_{\text{Pb2}} + S_{\text{MA1}} + S_{\text{MA2}} \quad (3.2)$$

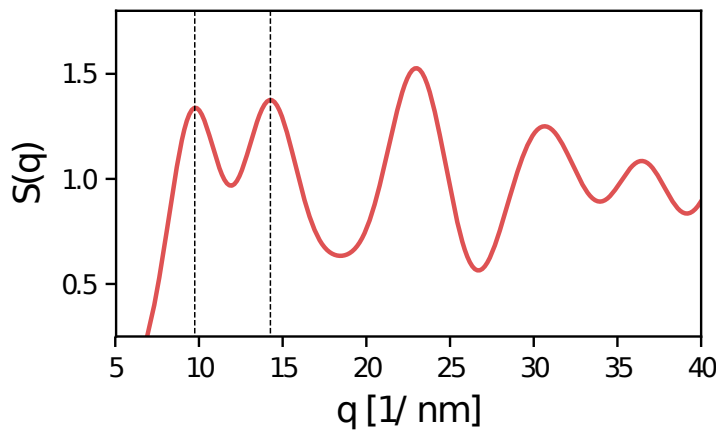


Figure 3.13 – **Calculated structure factor from Equation 3.1:** Debye structure factor of Pb^{2+} ions in cubic phase of MAPbI_3 . MA^+ have a similar profile due to the symmetry of the cubic phase.

I use this CV to perform the phase transition from the quasi-2D phase to 3D-perovskite. In this study, I have focused on the phase transition of halide perovskites. A similar methodology can also be used to study the phase transitions in many other perovskites systems such as MgSiO_3 [193] which is important for earth seismic activities and perovskite solid electrolytes which are promising materials for next-generation Li^+ ion solid-state batteries [194].

Dipping experiments on FAPbI_3

For FAPbI_3 samples, 1.3M PbI_2 solution (DMF:DMSO = 9:1) was spin coated at a speed of 2000 rpm/min for 30 seconds. Then, the PbI_2 layer was annealed at 70 degree C for 1 minute. After that, the PbI_2 layer was dipped inside a isopropanol(IPA) solution of FAI (20 mg/mL). XRD data is measured in the Bragg-Brentano geometry using a Bruker D8 Advance powder X-ray diffractometer. The setup has $\text{Cu K}\alpha$ ($\lambda = 1.54\text{\AA}$) radiation and operates in reflection, theta-theta mode (fixed sample) with a 2D strip detector. A beam mask of 1cm was chosen to suitably irradiate the films being measured. A step size of 0.01° was used for measurement and time/step was 0.15s. All results are presented in Fig. S10.

FAPbI_3 thin-film experiments:

Substrate preparation: Fluorine-doped tin oxide (FTO)-glass substrates (TCO glass, NSG 10, Nippon sheet glass, Japan) were cleaned by ultrasonication in Hellmanex (2%, deionized water), rinsed thoroughly with de-ionized water and ethanol, and then treated in oxygen plasma for 15 min. A 30 nm blocking layer (TiO_2) was deposited on the cleaned FTO by spray pyrolysis at 450°C using a commercial titanium diisopropoxide bis(acetylacetonate) solution (75% in 2-propanol, Sigma-Aldrich) diluted in anhydrous ethanol (1:9 volume ratio) as precursor and oxygen as a carrier gas. A mesoporous TiO_2 layer was deposited by spin-coating a diluted paste in ethanol (1:8.5 wt. ratio) (Dyesol 30NRD: ethanol) (3000 rpm, acceleration 2000 rpm for 20 s) onto the substrate containing TiO_2 compact layer, and then sintered at 450°C for 30 min in dry air.

Fabrication of perovskite films: Two stock solutions of 1.15 M PbI_2 were dissolved in 1mL DMF and DMF/DMSO (1ml of DMF and 100 l of DMSO) respectively, and then stirred at 70°C for 12 h. Next, these solutions were spin-coated on FTO/c- TiO_2 /meso- TiO_2 substrate at 4000 r.p.m. for 45 s and then heated at 80°C for 3-5 min to remove the solvents. After cooling down, the FAI (60mg) dissolved in 1 mL of IPA was spin-coated on top of the PbI_2 while the one dissolved in DMF or DMF/DMSO at 2500 r.p.m. for 45 s followed by annealing at 80°C for 40 min. In case of the effect of DMF/DMSO with IPA, first after cooling down the substrate (PbI_2 dissolved in DMF/DMSO), IPA solution was held on the substrate for 1 min without any further post-annealing and after that, the film was spin-coated at 4000 r.p.m. for 45 s [195, 196]. Next, the FAI was spin coating 2500 r.p.m. for 45 s followed by annealing at 80°C for 40 min.

3.2 Two-step phase transition from δ -FAPbI₃ to α -FAPbI₃ via vapor treatment

Obtaining highly crystalline, stable, and pure α -phase FAPbI₃ films are of vital importance. However, FAPbI₃ undergoes a phase transition from the black α -phase to the photoinactive δ -phase below 150°C. In this two-step process [74] deposition method, first equimolar mixtures of FAI and PbI₂ are mixed together to make yellow δ -FAPbI₃ film and then surface vapor treatment is used to convert δ -FAPbI₃ to the desired pure α -phase below the thermodynamic phase-transition temperature. We perform molecular simulations and layout the atomic level mechanism of the formation and stabilization of α -FAPbI₃.

3.2.1 Introduction

α -FAPbI₃ perovskite could be an ideal candidate for efficient and stable PSCs. Unfortunately, a photoinactive δ -FAPbI₃ is the most stable phase at room temperature, and the crystallinity of FAPbI₃ film is normally poor even after high-temperature annealing. To avoid formation of the δ -phase and to improve crystallinity, various compositions have been developed. To this end, various additives of alkali metals (K⁺, Rb⁺, Cs⁺) [197–199] and halides (Br⁻, I⁻) [200–203] were introduced as alloying recipes to make mixed-cation/anion α -phase PSCs. However, mixing results in unwanted blue shift in the light absorption and under long-term continuous illumination, different halides (Br⁻, I⁻) and cations (Cs⁺, FA⁺) can irreversibly segregate [43, 48] in their respective δ phases. Furthermore, MA⁺ is thermally unstable [204], therefore mixing strategies may be unfavorable for long-term operational stability.

In contrast to the previous mixing strategies, manipulation of surface energy has been reported to stabilize perovskite phases and modify the grain growth orientations [205, 206]. Motivated by these promising strategies of surface energy manipulations and recent work using polyiodide vapor for scalable perovskites [69], experimental collaborators developed a vapor treatment method for preparing efficient and stable α -FAPbI₃ PSCs.

In this two-step process, a thin-layer of δ -FAPbI₃ is deposited first, and after that methylammonium thiocyanate (MASCN) or formamidinium thiocyanate (FASCN) vapor treatment is used to convert δ -FAPbI₃ to the desired pure α -phase below its thermodynamical phase-transition temperature, meaning significantly below 150°C, see **Fig. 3.14**.

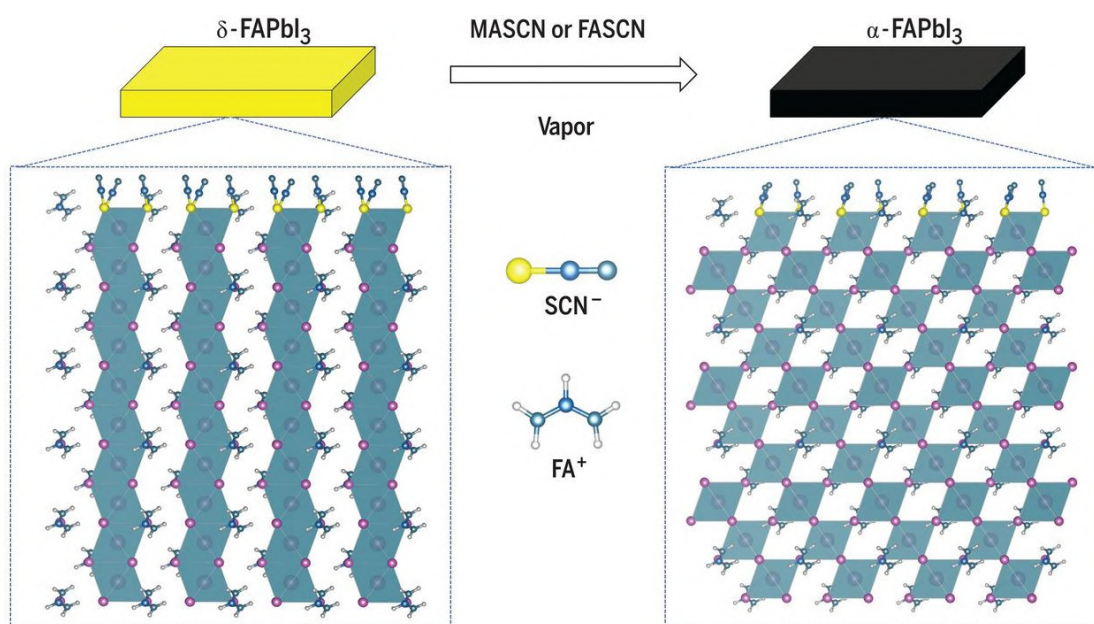


Figure 3.14 – A schematics of experiment and simulations of phase transition from δ -FAPbI₃ to α -FAPbI₃

3.2.2 Results

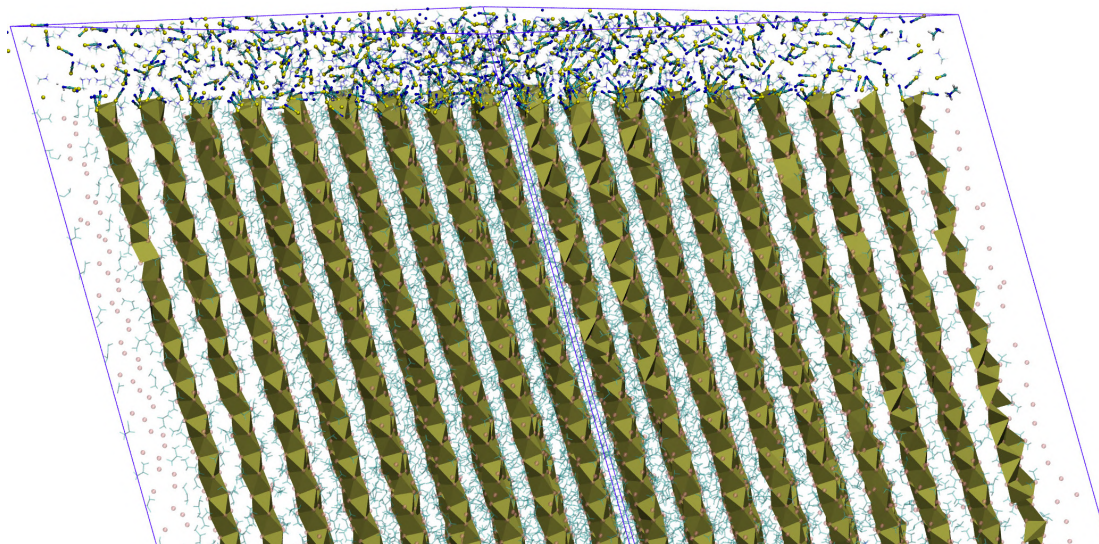


Figure 3.15 – **Simulation setup of classical MD:** A large slab of δ -FAPbI₃ with MA⁺ and SCN⁻ on top. This image was generated with Visual Molecular Dynamics (VMD). Pb-I octahedra are shown with golden color with iodide as orange balls at the corners of the octahedra. FA⁺, MA⁺, and SCN⁻ ions are shown with balls and sticks representation. Nitrogen is dark blue, carbon is light blue, hydrogen is white, and sulfur is yellow.

I performed MD simulations to gain insights into the vapor treatment process (see **Fig. 3.15**). I perform large scale classical MD simulation and small scale DFT based *ab-initio* MD. All details are provided in the methods sections. I find that the SCN^- ions on the surface of $\delta\text{-FAPbI}_3$ do not diffuse inside the face-sharing structure of $\delta\text{-FAPbI}_3$ but remain at the surface. Because of their strong affinity to Pb^{2+} ions, SCN^- anions coordinate to Pb^{2+} on the surface of $\delta\text{-FAPbI}_3$. In particular, Pb^{2+} ions are coordinated with the sulfur atoms of SCN^- (**Fig. 3.16**) strongly enough that the SCN^- ions displace the iodides. This process disintegrates the top layer of face-sharing octahedra and induces the transition to the corner-sharing architecture of $\alpha\text{-FAPbI}_3$.

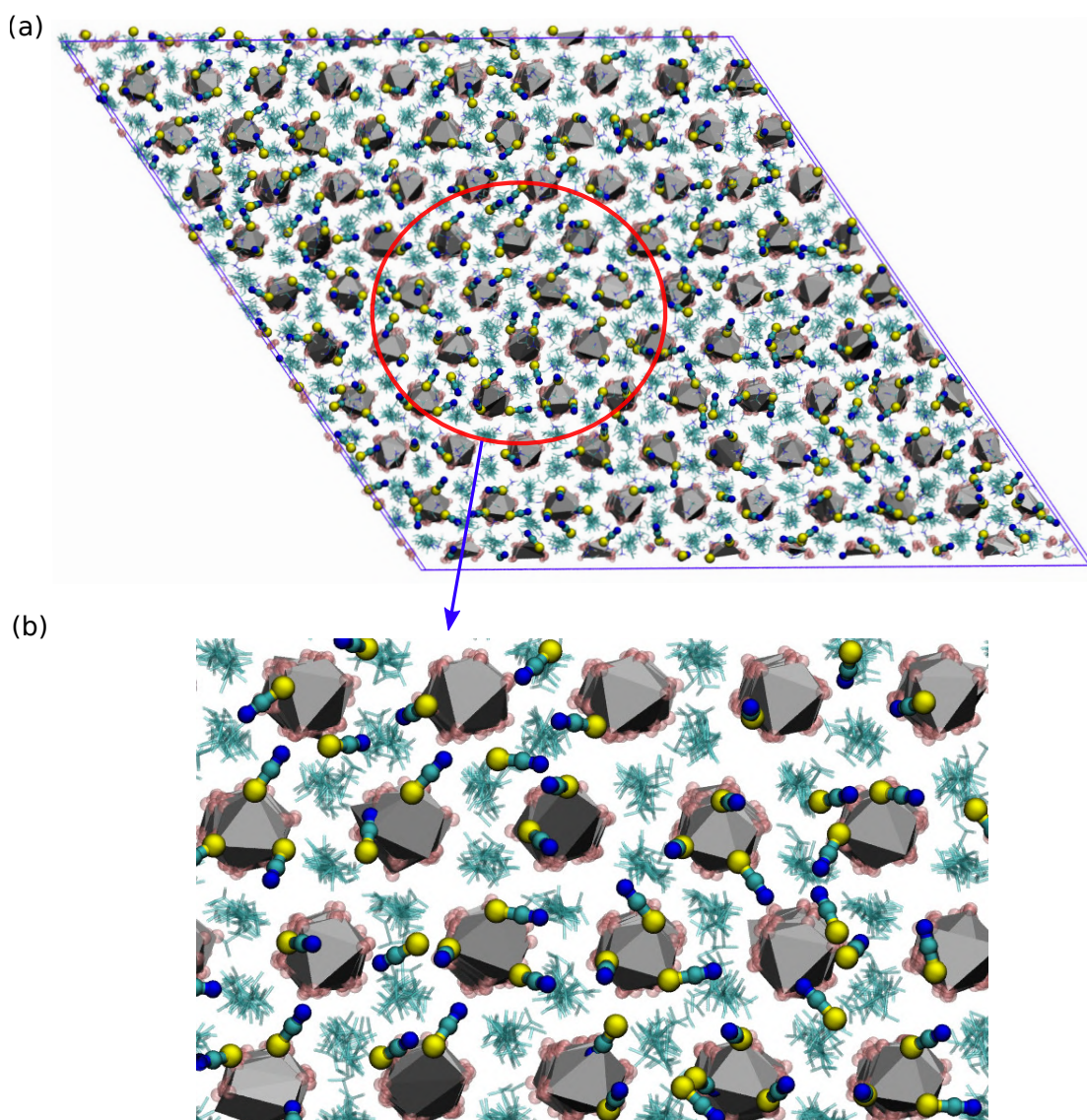


Figure 3.16 – **Top view of the adsorption of SCN^- ions on top of $\delta\text{-FAPbI}_3$:** (a) Top view of the simulations. (b) A zoomed-in version of a small part of the top view to clearly show the adsorption of SCN^- ions on top.

Furthermore, the disruption of the topmost surface layer with SCN^- ions also helps the penetration of monovalent cations (MA^+ , FA^+) into the PbI_6 chains of δ -FAPbI₃, which further helps the growth of α -FAPbI₃, in agreement with the solid-state NMR analysis [74].

I investigated the successive rearrangement of ions at the surface of δ -FAPbI₃. Some parts of face-sharing octahedra on the interface start to form corner-sharing Pb-I-SCN structures. With the addition of extra SCN^- ions, corner-sharing structures, which contain mixtures of SCN^- ions and iodides, are formed and stabilized. The atomic view of this whole transformation from face-sharing to corner-sharing octahedra is shown in **Fig. 3.17**. Further analysis reveals that the conversion of the face-sharing structure proceeds through the formation of edge-sharing intermediates. This results mainly from the step-by-step addition of SCN^- ions around the Pb^{2+} ions. In the first chapter, I have also shown the formation of such intermediate structures before conversion to perovskites [192]. Some domains of the mixed-corner and face-sharing structures formed during the simulation, and I found that SCN^- ions could also induce the formation of polytypes at the interface.

I observed the formation of localized structures similar to the well-known 4H polytypes of FAPbI₃ (**Fig. A.9**). We also generated a model of a periodic structure of 4H polytype with iodides replaced by SCN^- and found that this structure remained stable after variable cell first-principles DFT optimization (see the Methods section). From these simulations, I can conclude that SCN^- ions drive and stabilize the formation of corner-sharing structures upon contact formation with MASCN/FASCN, which in turn triggers the conversion to α -FAPbI₃. This process can occur below the thermodynamic phase-transition temperature. A further illustration of the δ to α -phase transition by SCN^- ions from the surface to the bulk is shown in **Fig. 3.18**.

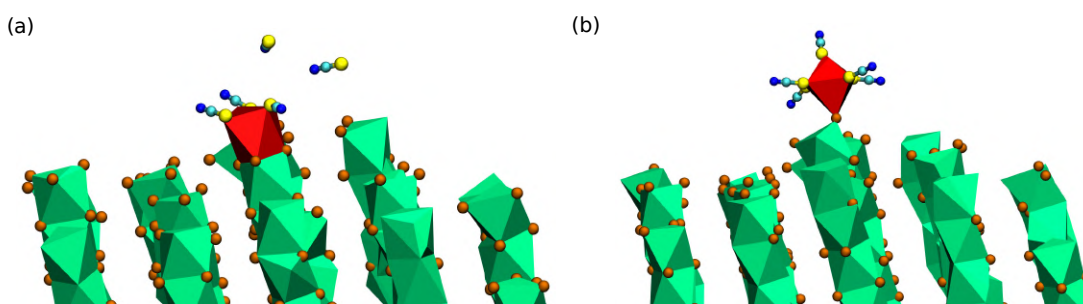


Figure 3.17 – MD simulations showing a structural conversion: Representative snapshots from the MD simulations showing a structural conversion of (A) the initial face-sharing octahedra and (B) the corner-sharing octahedra. Pb-I octahedra are shown in green; iodide is shown as orange balls on corners. To highlight the structural transformation, red was chosen for octahedra on the interface. FA^+ and MA^+ ions are not shown for clarity. Selected SCN^- ions are shown as ball and stick representations: sulfur is yellow, carbon is light blue, and nitrogen is dark blue (the other SCN^- ions are not shown for clarity).

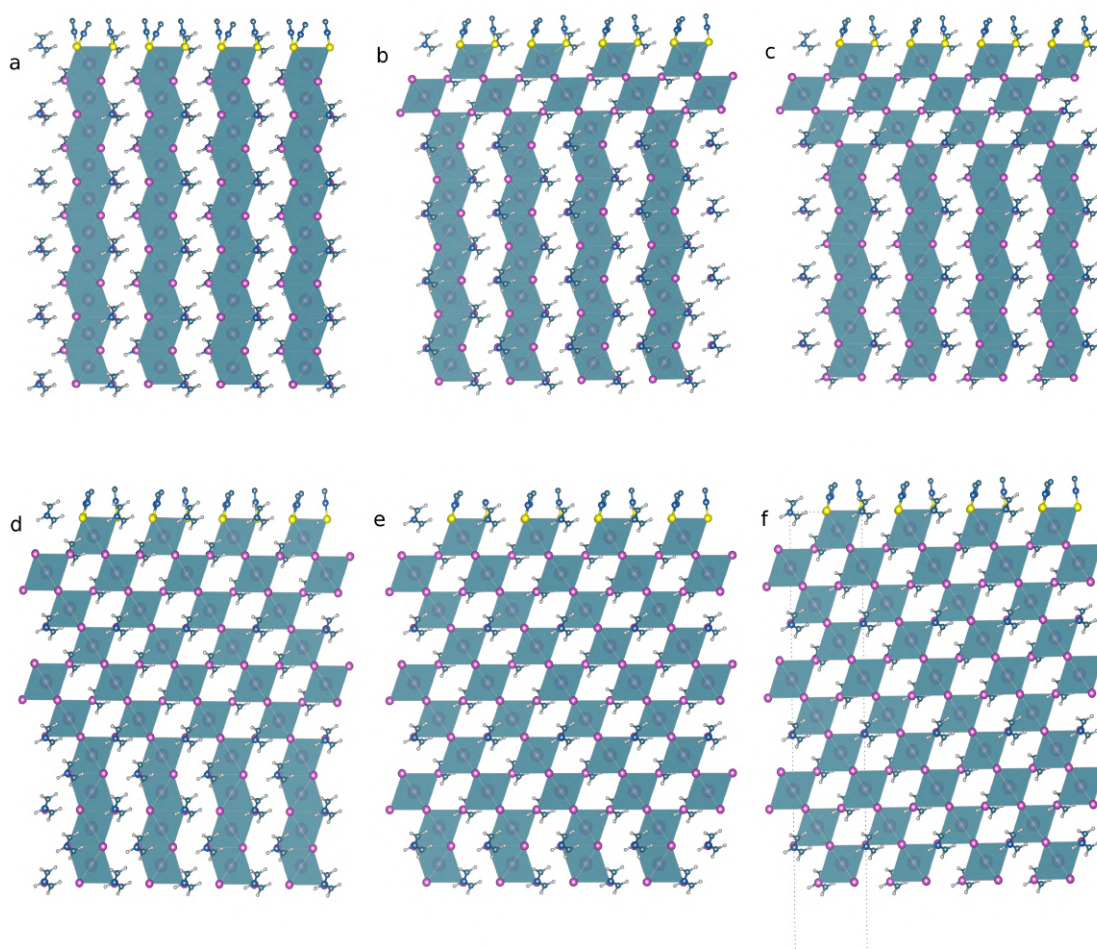


Figure 3.18 – Illustration of a possible phase transition path induced by SCN^- anions: (a) δ -phase FAPbI_3 structure. The mixtures of δ and α -phases of FAPbI_3 with the increasing number of corner-sharing structures from (b) to (e). (f) α -phase FAPbI_3 structure. SCN^- ions are adsorbed on the top of the respective structures. Pb^{2+} octahedra are portrayed with light blue colour with iodide as pink balls on corners. FA^+ and SCN^- ions are represented with balls and sticks representation. All the images were generated with the VESTA software.

3.2.3 Kinetic stability of α - FAPbI_3

Experiments show that once a film of the yellow phase was converted to a highly crystalline black α -phase by vapor exposure of $\text{MASCN}/\text{FASCN}$ at 100°C , it retained this structure after 500 hours at 85°C . Solar cells fabricated with this material had a power conversion efficiency of more than 23% [74]. After 500 hours under maximum power tracking and a period of dark recovery, 94% of the original efficiency was retained.

The fundamental question arises that why the phase pure α - FAPbI_3 based solar cells are stable and do not degrade or transform back to thermodynamically stable δ -phase during operation and even at 85°C . We first hypothesized that the phase pure α - FAPbI_3 is a kinetically stable

structure. To prove this hypothesis I performed molecular simulations to calculate the energy barrier between these two polymorphs of FAPbI₃.

At first, I identified a possible phase transition pathway between δ and α -phase of FAPbI₃. I constructed a 288 atoms super-cell of δ -phase and explored the phase space between δ and α -phases of FAPbI₃ by performing classical MD simulations at different temperatures and pressures. I successfully observe the phase transition going from face-sharing to edge-sharing to corner-sharing structures. I also find that the increasing pressure could break face-sharing octahedra and help in transformation towards increasing corner-sharing structures. This is also demonstrated by recent experiments [207]. To calculate the potential energy landscape of this transition pathway, I performed first-principles DFT calculations for each structure, detailed in the methods section. The final energy profile along this path could provide a good estimate of the possible height of the energy barrier involved in the transition between the two phases.

My calculations show that the reverse phase transition from α to δ -phase is restrained by a high potential energy barrier of ≈ 0.7 eV/f.u., see **Fig. 3.19**. Therefore, we prove that once the phase-pure α -phase FAPbI₃ is formed, it remains kinetically arrested in its α form. This is also demonstrated by different experiments[208], where crystallized α -FAPbI₃ was shown to be stable in black phase. Furthermore, Peidong Yang and co-workers [209] performed experiments to calculate the energy barrier between polymorphs of different halide perovskites. They use *in-situ* optical imaging and quantitatively calculated the rates of phase propagation while heating the δ -FAPbI₃ nanowires at different temperatures. Using plot fitting with Arrhenius equation, they calculate the activation energy barrier height going from δ to α -FAPbI₃ to be $\approx 0.84 \pm 0.25$ eV/f.u. [209]. Therefore, my calculations presented in **Fig. 3.19** are in substantial agreement with experiments.

An interesting observation was noticed in these experiments: a large blue-shift in the photoluminescence (PL) peak (~ 38 meV) at the low-temperature/high-temperature two-phase interface of partially transformed FAPbI₃ nanowire. This observation is again of high practical relevance as such phase transition could be present in many experimental recipes to make FAPbI₃ based PSCs. From this, I move to another fundamental question that why a direct conversion (no vapor treatment, only by heating $>150^\circ$) of δ to α -phase always results in lower device efficiencies. To understand this, I explore possible polymorphs of FAPbI₃ that could form while heating δ to α -phases. For this, I extracted different structures from the phase transition trajectory obtained from above mentioned classical MD simulations. These structure were relaxed at DFT level by performing variable cell enthalpic optimization. Some of the relaxed structures are shown in **Fig. 3.19**. I find that many of these phases relaxed into well defined periodic structures, made of mixed layers of edge/face-sharing and corner-sharing octahedra. These are very similar to the commonly known hexagonal stacking faults that are observed during a typical phase transition from hexagonal to cubic phases. In the end, I hypothesize that these stacking faults/polytypes are responsible for the large blueshifts observed in these phase-transition experiments and might remain in the bulk even after ex-

cessive heating. I note here that this remains an open question and needs further experiments and theoretical calculations.

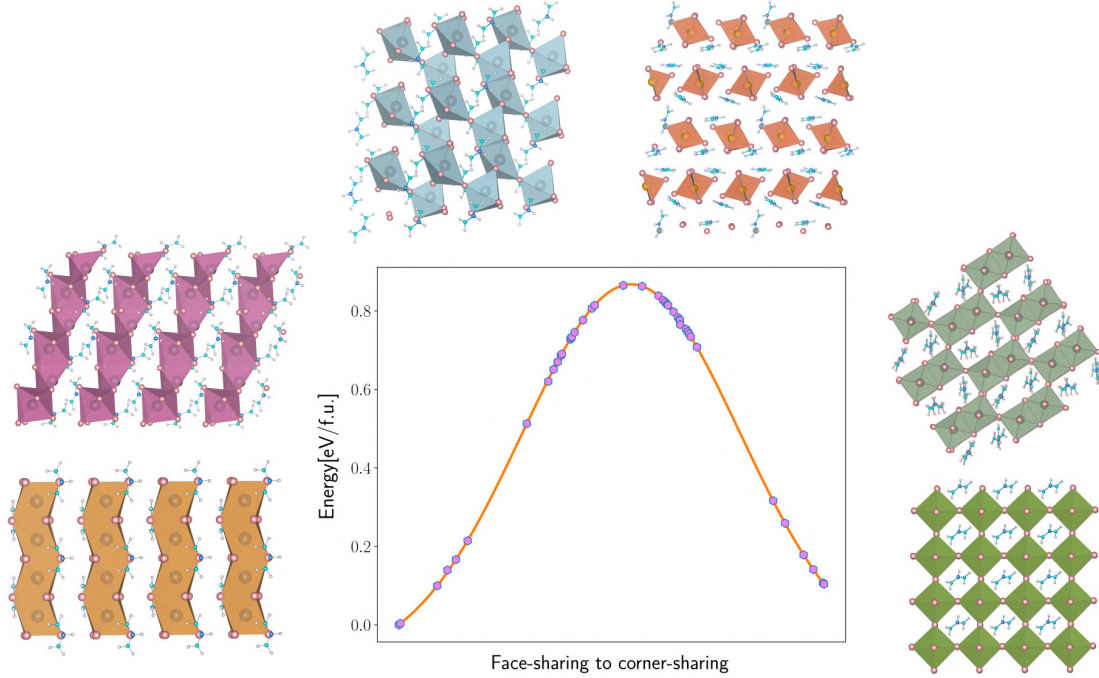


Figure 3.19 – **Energy diagram along a transition from δ -FAPbI₃ and α -FAPbI₃**: Each point on the energy plot represent a different DFT optimized structure along the path. A Gaussian fit of these points is included as guide to the eyes. For better visualization of the pathway, we have illustrated some of the intermediate phases. Pb-I octahedra are represented with light green colour with iodide on corners with pink balls. FA⁺ cations are shown with ball and sticks representation.

3.2.4 Methods

Classical MD simulations

I constructed a large supercell of δ -phase FAPbI₃ with 28800 atoms (2400 stoichiometric units of FAPbI₃). To perform molecular dynamics (MD) simulations of FAPbI₃, I followed a similar procedure as used in our previous work [210]. Polytypes play an important role in crystallization of FAPbI₃ [96]. Therefore, I also upgraded the previously used force field to be able to simulate all the experimentally known polytypes (2H, 4H, 6H and 3C) of FAPbI₃. At first, I equilibrated this supercell by performing 10 ns variable-cell isothermal-isobaric simulations at 370 K. Next, I exposed this supercell to MA⁺ and SCN⁻ ions. With this set-up, I again performed an equilibrium run for 2 ns in isothermal-isobaric ensemble at 370 K with a force field for SCN⁻ ions available from literature [211]. Interaction parameters between different heterogeneous species were calculated with mixing rules. All production runs were performed in isothermal-isobaric ensemble ranging from 20-100 ns. All simulations were

performed with the Large-Scale Atomic/Molecular Massively Parallel Simulator (LAMMPS) code (31 Mar 2017) ([127]). I used a 1.0 nm cutoff for nonbonded interactions, SHAKE for constraints and particle-particle-particle-mesh Ewald for electrostatic interactions. I used a velocity rescaling thermostat ([128]) with a relaxation time of 0.1 ps and a Parrinello-Rahman barostat ([129]) to keep the pressure at atmospheric pressure with a relaxation time of 10 ps.

DFT calculations of 4H and 2H polytype with SCN^-

First, I replaced up to 50% I^- with SCN^- ions in the 2H (δ -phase) and 4H-FAPbI₃ crystal structures ([96]). Then, I performed variable cell first-principles DFT calculations of these structures with Generalized Gradient Approximation in the Perdew-Burke-Ernzerhof formulation revised for solids (PBEsol)[212]. I used Quantum Espresso [156] with ultra-soft pseudo-potentials for valence-core electron interactions with a plane wave basis set of 60 Ry kinetic energy cutoff and 420 Ry density cutoff. The Brillouin zone was sampled by a 2x2x2 k-points grid for 192 atoms supercell of 4H-FAPbI₃. The optimized structure is shown in Appendix. All DFT calculations for the energy barrier used Perdew-Burke-Ernzerhof (PBE) [141] functional with D3-vdW [142] dispersion corrections. The Brillouin zone was sampled by a 3x3x2 k-points grid for 288 atoms (24 f.u.) supercell of α -FAPbI₃ and equivalent for other structures.

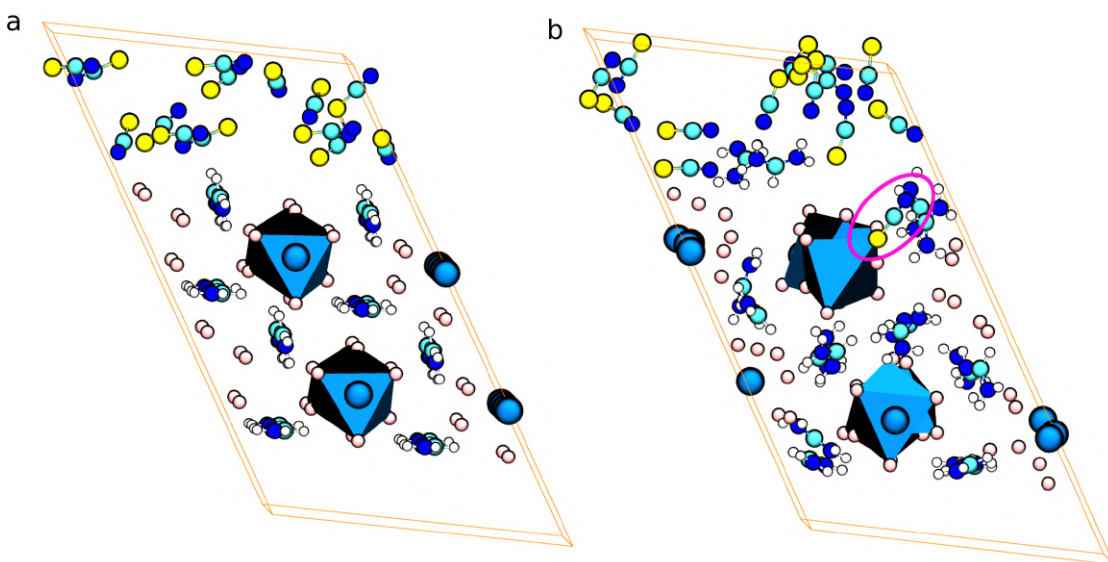


Figure 3.20 – **Configuration for the δ -FAPbI₃ with SCN^- on top:** (a) The starting configuration (at $t=0$) and (b) the configuration at $t \sim 10$ ps for the δ -FAPbI₃ with SCN^- on top. We show the dimensions of the supercell to display the empty space used to treat the SCN^- ions as vapor between periodic slabs. Pb^{2+} ions and octahedron are shown with blue colour with iodide as light pink balls. FA^+ and SCN^- ions are shown with balls and sticks representation.

Ab-initio MD of SCN⁻ vapor on δ -phase

An initial configuration, as depicted in **Fig. 3.20** was created by putting 14 SCN⁻ ions in a box with a 192 atoms supercell of δ -phase FAPbI₃. Constant temperature and constant volume Born-Oppenheimer MD simulations were performed with the CP2K package [145, 146]. We used a time step of 1fs and a Nose-Hoover chains [147–149] for temperature control. I performed BOMD simulations at two different temperatures: 300 and 400 K. All simulations used DFT at the PBE+D3 [141, 142] level with double-zeta basis sets (DZVP-MOLOPT for Pb, I, S, C, N, H) [143] and Goedecker-Teter-Hutter (GTH) pseudopotentials [144] with 560 Ry density cutoff.

4 Structure prediction of low-dimensional perovskites

This chapter was adopted from the following articles:

Postprint version of the article: M. C. Gelvez-Rueda, P. Ahlawat, L. Merten, F. Jahanbakhshi, M. Mladenovic, A. Hinderhofer, M. I. Dar, Y. Li, A. Ducinkas, B. Carlsen, W. Tress, A. Ummadisingu, S. M. Zakeeruddin, F. Schreiber, A. Hagfeldt, U. Rothlisberger, F. C. Grozema, J. V. Milic, and M. Graetzel, "Formamidineium-based Dion-Jacobson layered hybrid perovskites: structural complexity and photoelectronic properties." *Advanced Functional Materials* 30, no. 38 (2020): 2003428. (DOI: 10.1002/adfm.202003428)

My contribution: Partially conceived and conceptualized research of structure prediction. Designed, performed and analyzed simulations on structure prediction. Equal contribution as the first author.

Postprint version of the article: M. A. Hope, T. Nakamura, P. Ahlawat, A. Mishra, M. Cordova, F. Jahanbakhshi, M. Mladenovic, R. Runjhun, L. Merten, A. Hinderhofer, B. I. Carlsen, D. J. Kubicki, R. Gershoni-Poranne, T. Schneeberger, L. C. Carbone, Y. Liu, S. M. Zakeeruddin, J. Lewinski, A. Hagfeldt, F. Schreiber, U. Rothlisberger, M. Graetzel, J. V. Milic, and L. Emsley, "Nanoscale phase segregation in supramolecular π templating for hybrid perovskite photovoltaics from NMR crystallography." *Journal of the American Chemical Society* 143, no. 3 (2021): 1529-1538. (DOI: 10.1021/jacs.0c11563)

My contribution: Partially conceived and conceptualized research of structure prediction. Designed, performed and analyzed simulations on structure prediction. Equal contribution as the first author.

Postprint version of the article: L. Hong, J. V. Milic, P. Ahlawat, M. Mladenovic, D. J. Kubicki, F. Jahanbakhshi, D. Ren, M. C. Gelvez-Rueda, M. A. Ruiz-Preciado, A. Ummadisingu, Y. Liu, C. Tian, L. Pan, S. M. Zakeeruddin, A. Hagfeldt, F. C. Grozema, U. Rothlisberger, L. Emsley, H. Han, and M. Graetzel, "Guanine-stabilized formamidineium lead iodide perovskites." *Angewandte Chemie International Edition* 59, no. 12 (2020): 4691-4697. (DOI: 10.1002/anie.201912051)

My contribution: Partially conceived and conceptualized research of structural analysis. Designed, performed and analyzed simulations on structure predictions.

Postprint version of the article: F. Jahanbakhshi, M. Mladenovic, E. Kneschaurek, L. Merten, M. C. Gelvez-Rueda, P. Ahlawat, Y. Li, A. Ducinkas, A. Hinderhofer, M. I. Dar, W. Tress, B. Carlsen, A. Ummadisingu, S. M. Zakeeruddin, A. Hagfeldt, F. Schreiber, F. C. Grozema, U. Rothlisberger, J. V. Milic, and M. Graetzel, "Unravelling the structural complexity and photophysical properties of adamantyl-based layered hybrid perovskites." *Journal of Material Chemistry A*, 2020, 8, 17732-17740. (DOI: 10.1039/D0TA05022A)

My contribution: Partially conceived and conceptualized research of structural analysis. Designed, performed and analyzed simulations on structure prediction.

4.1 Introduction

Stability is one of *the* main problems in the field of halide perovskites. Several external factors can affect their stability; however, the most commonly known issues are humidity and bulk defects. Molecular additives are often used to resolve these issues by passivating the surface of perovskite crystals to eliminate ionic defects and protect PSCs from water. However, different molecular additives can have different electronic and physical properties, which can also harm PSCs performance. To solve this issue in advance, one can perform *first-principles* calculations to understand the structural and electronic properties. However, to perform such calculations to build any atomic level understanding, one has to know the molecular/crystal structure of the system. Many of the molecular additives are expected to form low-dimensional perovskite structures. Although experimental techniques such as X-ray diffraction, electron microscopy, NMR crystallography are well suited to obtain crystal structures, however in most cases, these techniques require single crystals. Synthesis of single crystals of low-dimensional perovskites could be a formidable task. Moreover, experimental methods are limited for screening a wide range of complex molecular additives. Molecular simulations can help and assist experiments in solving this problem. In this chapter, I describe the structure prediction of low-dimensional halide perovskites. We validate the predicted structures by comparing their physical properties with the available experimental data.

4.2 Structure prediction with constraints

I start with the assumption that molecular additives would form typically known structures of quasi-2D halide perovskites of the Ruddlesden-Popper(RP)[213] or Dion-Jacobson (DJ)[214, 215]. Therefore, my approach is confined to finding ligands' most stable RP or DJ configuration between the layers of corner-sharing Pb-I octahedra. As a general procedure, I always start from an approximate DJ structure of $n=1$ composition, with the well-aligned inorganic slabs of corner-sharing Pb-I octahedra (with PbI_4^{2-} stoichiometry). Then I place the molecular additives (cations) between these layers with the ammonium sites in A-cation cavities similar to reported experimentally determined crystal structures [216]. Afterward, I optimize this structure in two steps: first, I perform classical MD simulations with increasing temperatures up to 500K, as described in the Appendix. During this step, if I observe that the structures do not remain in a perovskite-like corner-sharing geometry, I discard this configuration and build another structure with a different arrangement of organic molecules. This new geometry is consistently built from the information obtained from failed simulations. Once a stable structure is found from this trial and error technique, I perform variable-cell DFT optimization to get the final structure for the low-dimensional perovskite. In the end, I verified the simulated structures by comparing their physical and electronic properties with the experimental data. In the following sections, I describe this process for different organic molecules.

4.3 Guanine-based low-dimensional halide perovskite

In this project [210], guanine (G) was used as a molecular additive to stabilize FAPbI₃ based solar cells. Molecular simulations were employed to gain insights into a possible structural model compared with the experimental findings. I start from an approximate Dion-Jacobson (DJ) structure of $n=1$ composition, with well-aligned inorganic slabs (G₂PbI₄; **Fig. A.10a**). In a first attempt, guanine cations were arranged parallel with ammonium sites in A-cation cavities. To optimize this structure, I first performed classical MD simulations, as described in the Appendix. We find that the optimized structure adopts an edge-sharing geometry (**Fig. A.10d**). In this arrangement of guanine cations, oxygen atoms display a propensity for hydrogen bonding with the ammonium groups of adjacent guanine cations. This can lead to rearrangements of guanine cations that prevent the final configuration from remaining a stable perovskite structure. Thus, I discarded this simulation and analyzed the alternative one where oxygen atoms of guanine cations are positioned next to other possible hydrogen bonding sites of adjacent guanine cations (**Fig. A.11a,b**). Again, I perform classical MD simulations and find that this structure shows a high level of instability (**Fig. A.11d**) and is therefore not likely to occur in experiments. I build another structure with the same aim to keep the oxygen atoms away from ammonium groups. I optimize the structure, but also in this case we end up in a distorted structure (**Fig. A.12d**).

From the second and third attempts, I found that the structures go through a transient phase with guanine cations overlapping with each other (**Fig. A.11b,c**). This could be due to π - π interaction between guanine cations. Moreover, π - π interactions are known to play an important role in both structural and electronic properties in guanine-containing compounds. Based on these simulations, I build another structure that appropriately accommodates hydrogen bonding and π - π interactions between guanine cations. The supercell of such a structure is shown in **Fig. 4.1** for $n=1$ and **Fig. A.13** for $n=2$. I perform simulations to optimize these structures and find that the optimized structure forms a stable layered 2D perovskite configuration. The optimized structures are shown in **Fig. 4.1c,d** ($n=1$) and **Fig. A.13c** ($n=2$). I observe strongly bonded and highly rigid layers of guanine cations in the low-dimensional structure with this configuration.

4.3.1 Proton transfer

In the previous section, we have predicted a possible structure of G₂FA _{$n-1$} Pb _{n} I_{3 $n+1$} . The corresponding structures were later optimized with electronic structure methods based on DFT. We use a smaller cell size as the number of atoms limits electronic structure calculations. Further details are presented in the Appendix. I find that the DFT optimized structures remain in the same configuration as those obtained from classical MD simulations. The optimized structures are shown in **Fig. A.14** for $n=1$ and **Fig. A.15** for $n=2$. During relaxation for $n=1$, interestingly, I observe that a proton transfer occurs in one of the layers of guanine cations. The whole process is depicted in **Fig. 4.2**. This process leads to the formation of two different

tautomers (shown in **Fig. A.16**) of guanine cations in the same structure. One of the important facts is that tautomerization happens during geometry optimization, highlighting the fact that there is no energy barrier to the formation of these tautomers.

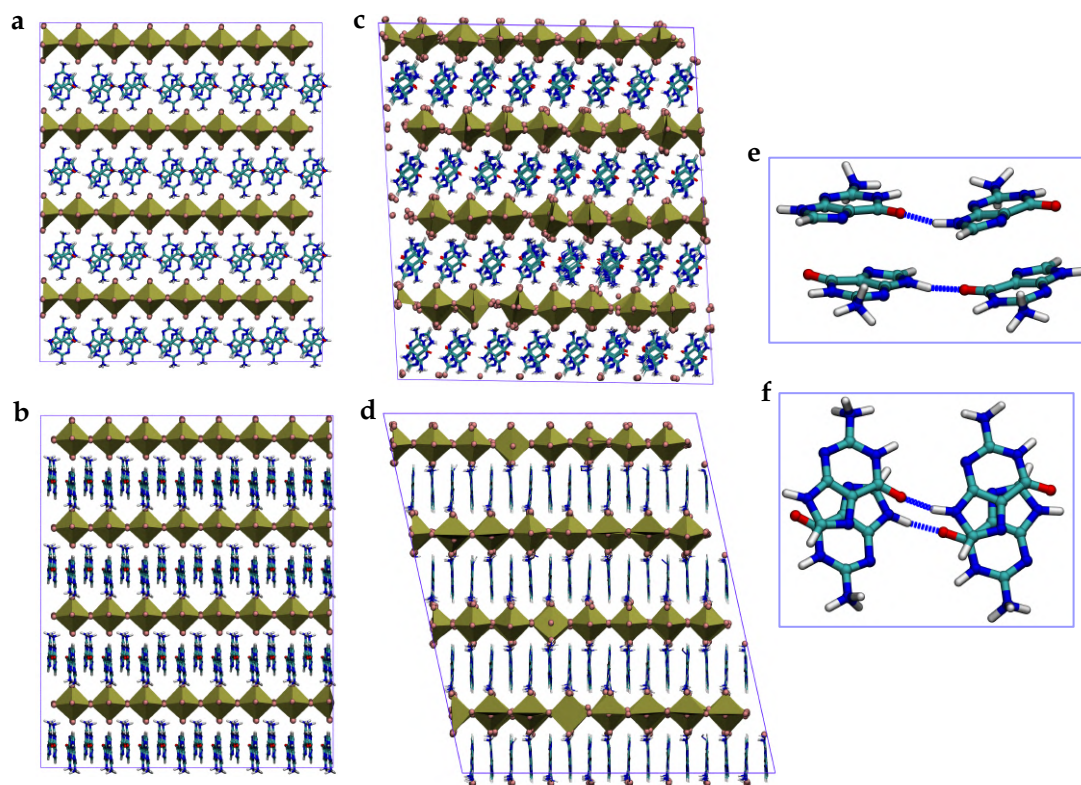


Figure 4.1 – **Predicted structures:** Images (a) and (b) are front and side view of an initially estimated supercell for $n=1$. (c) and (d) show the front and side view of final structure. (e) and (f) illustrate the structure and hydrogen bonding of guanine molecules in the final structure. Lead (Pb^{2+}) ions are shown with golden balls, iodide (I^-) ions are displayed with pink spheres. Pb-I polyhedra are displayed in golden color. Guanine ions are illustrated with balls and sticks.

This insight leads to vital information that these tautomers and their derivatives can also be present during the crystallization of these structures and will play an essential role in the evolution of the final structure. There is another insight emerging from these simulations. I see a chain of simultaneous proton transport at the ends of guanine cations. This result may suggest that guanine cations might have long-range charge transport properties, improving the charge transport properties of low-dimensional lead halide perovskites. However, this has to be addressed with further in-depth experiments and simulations.

I assessed these possible G_2PbI_4 and $\text{G}_2\text{FAPb}_2\text{I}_7$ configurations by comparing them to the experimental findings from experimental collaborators. First, the structural properties of the resulting system matched well the molecular dimensions (0.74nm) revealed by both the

TEM and XRD measurements [210]. Moreover, DFT calculations of the structures suggested that proton transfer occurs between the molecules in the spacer layer, which supports the existence of multiple tautomeric forms (observed in ssNMR experiments). In this fashion, the G-based spacer layer might affect proton transfer along with providing enhanced transport for electronic charge carriers.

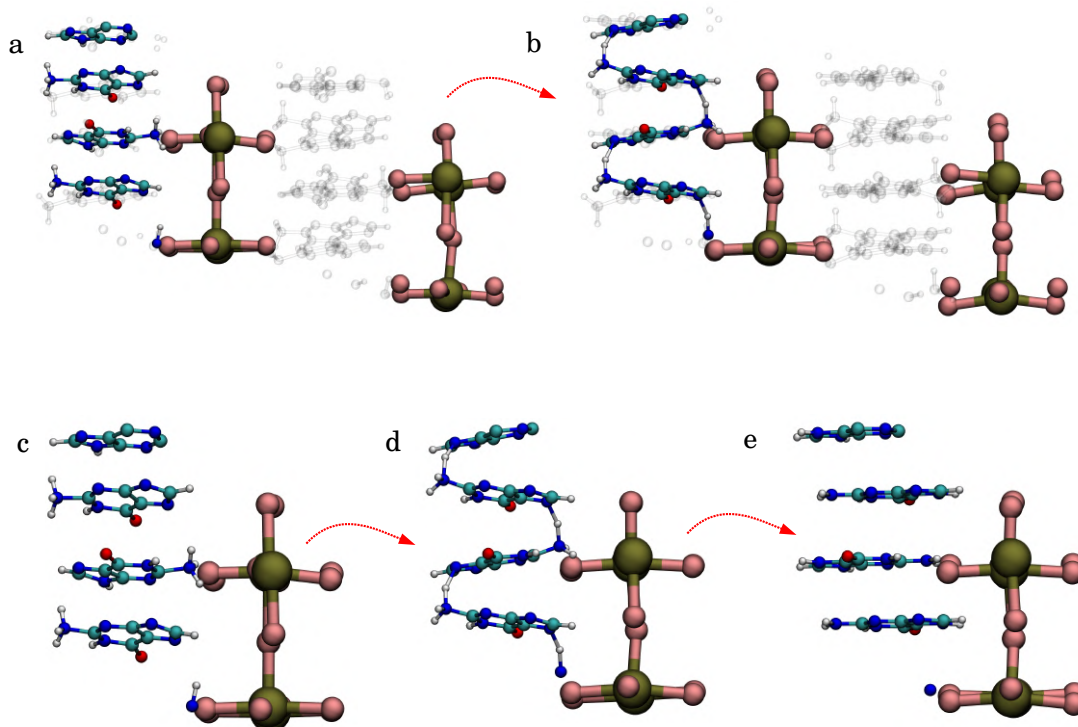


Figure 4.2 – **Full pathway of proton transfer in $n=1$** : (a) shows the initial configuration. Image (b) is the snapshot where hydrogens are shared between guanine molecules. (c) and (d) are the zoomed images from (a) and (b) respectively. Snapshot (e) is the final optimized geometry and illustrates that hydrogens are transferred

4.4 1,4-phenylenedimethan ammonium (PDMA)

Here, the structure and physical properties of low-dimensional halide perovskites featuring (PDMA) $\text{FA}_{n-1}\text{Pb}_n\text{I}_{3n+1}$ ($n = 1-3$) [217] formulations are unraveled. In the case of small aromatic bifunctional spacers, a DJ type of structure is envisaged [216]. I start from an initially built DJ structure of (PDMA) $\text{FA}_{n-1}\text{Pb}_n\text{I}_{3n+1}$ composition ($n = 1$) by appropriately placing the ligands in between layers of corner-sharing Pb-I octahedra. While equilibrating the structure, I observe a structural transition to something that appears to be a mixture of DJ and RP structures. I find that the mixed-phase persists at room temperature. However, the structure transforms to DJ

when we heat the system up to higher temperatures > 350 K (as shown in **Fig. 4.3**). I note here that the predicted structure is in good agreement with the XRD and ss-NMR experimental data.

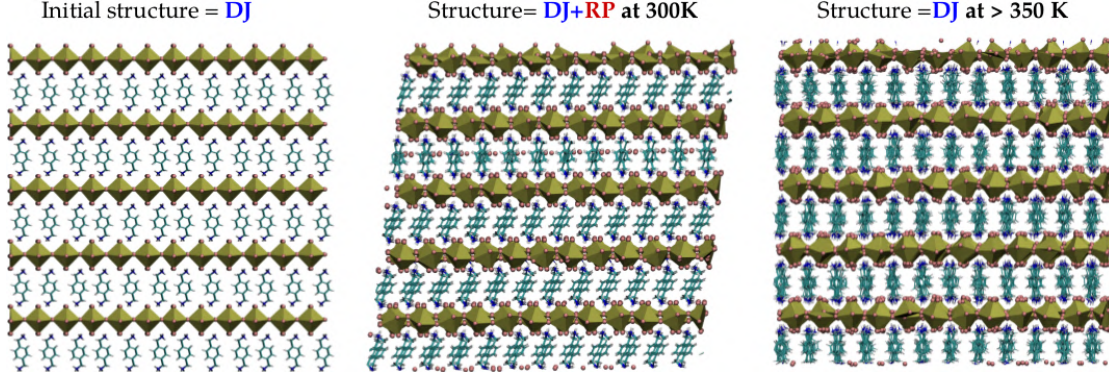


Figure 4.3 – Change in structure with increasing temperature: Image on the left is the initial geometry, middle one is the intermediate phase and image on the right is the final relaxed structure. Lead (Pb^{2+}) ions are shown with golden balls, iodide (I^-) ions are displayed with pink spheres. Pb-I octahedra are displayed in golden color. Ligand B is illustrated with balls and sticks. The images are generated with VMD.

In order to further probe the effect of temperature, I calculated the angular autocorrelation function (ACF) of PDMA orientation $\langle \hat{v}(t) \cdot \hat{v}(0) \rangle$ ($\hat{v} = (\vec{r}_{C5} - \vec{r}_{C1}) / (|\vec{r}_{C5} - \vec{r}_{C1}|)$) as:

$$ACF = \langle \hat{v}(t) \cdot \hat{v}(0) \rangle = \frac{1}{N} \sum_{i=1}^N \frac{1}{M} \sum_{\theta=1}^M \hat{v}_i(t + t_\theta) \cdot \hat{v}_i(t_\theta) \quad (4.1)$$

Where \vec{r}_{C5} and \vec{r}_{C1} are positions of atoms C5 and C1 of ligand B as depicted in **Fig. 4.4**. The time-dependent ACF of the PDMA molecular orientation is computed as an average over all the pairs of the configurations at a given lag time to each other (over $\theta=1, M$). From **Fig. 4.4a**, one can observe that with the increase in temperature, molecules rotate faster as compared to lower temperatures. However, while comparing the ACF for $n=1$ and $n=2$, we observe that rotation of ligands is significantly faster for $n>1$ as compared to $n=1$. These observations about ACF also suggest that entropy might play a significant role in the crystallization or stabilization of these proposed 2D perovskites structures. From our simulations of $n=2$, $n=3$ and $n=4$, we find that the structures do not go through any intermediate phase as for $n=1$ and stay in the DJ phase. This difference may arise due to the strong π - π interactions between the ligands in $n=1$. We find that there are two different types of stacking in the structures of $n=1$ at temperature < 350 K: T-shaped and parallel-displaced as shown in **Fig. A.17**. Moreover, in the case of $n=1$, the molecules would have more freedom to slide than $n>1$. Also, there is a significant tilt between the adjacent Pb-I octahedra for $n=1$ in mixed DJ+RP phases. These qualitative insights can be beneficial for analyzing the structural properties of 2D perovskite with a bi-cation spacer. Different pi-stacking patterns may dominate when these ligands are

used to make 2D structures of these perovskites.

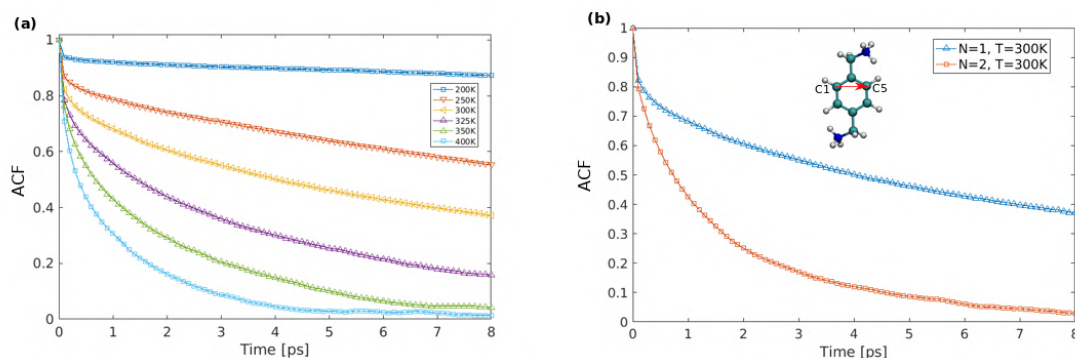


Figure 4.4 – **Time dependent autocorrelation function of the unit C1-C5 vectors of ligand B:** Image (a) display the behavior of ACF at different temperatures from 200-400K for n=1 and (b) is the comparison between n=1 and n=2 at 300K.

4.5 (1-adamantyl)methan ammonium (A) and 1-adamantyl ammonium (A')

I perform classical MD simulations of the structure presented in **Fig. A.18** [218]. The simulation procedure is similar to one described in the previous sections. Following a gradual increase in temperature, I observe that the structure changes to the RP phase and stays in RP for a long time (30ns). This is shown in **Fig. A.19**. These simulations show that the final structure in the RP phase has a stable minimum on the potential energy surface compared to the initial DJ structure. Furthermore, I also found that temperature has significant effects on structural properties. In **Fig. A.19**, I show the evolution of the structure with the increase in temperature. One of the aspects I observe is that there is transition in the configuration of the ligand from **Fig. A.19d** to **Fig. A.19e**. The snapshots in **Fig. A.19d** is taken around 150K and **Fig. A.19e** is taken at room temperature. I find that the ligands are parallel to each other at lower temperatures.

However, at higher temperature the aromatic rings and the terminal ammonium groups of the ligand start to rotate around the backbone of the ligand. These rotations can also be seen in **Fig. A.19f**. For further information, I have calculated the ACF of ligand A orientation $\langle \hat{v}(t) \cdot \hat{v}(0) \rangle$ ($\hat{v} = (\vec{r}_{C8} - \vec{r}_{C3}) / (|\vec{r}_{C8} - \vec{r}_{C3}|)$) as given in **Equation 4.1**. Where \vec{r}_{C8} and \vec{r}_{C3} are positions of atoms C8 and C3 of ligand A as depicted in **Fig. 4.5**. The rotational times of ligand-A are of the order of ns which is in qualitative agreement with the ns time scale from ssNMR studies reported in previous study. Similar simulations were performed for n=2, n=3 and n=4 with similar findings, i.e. that the most stable phase is RP.

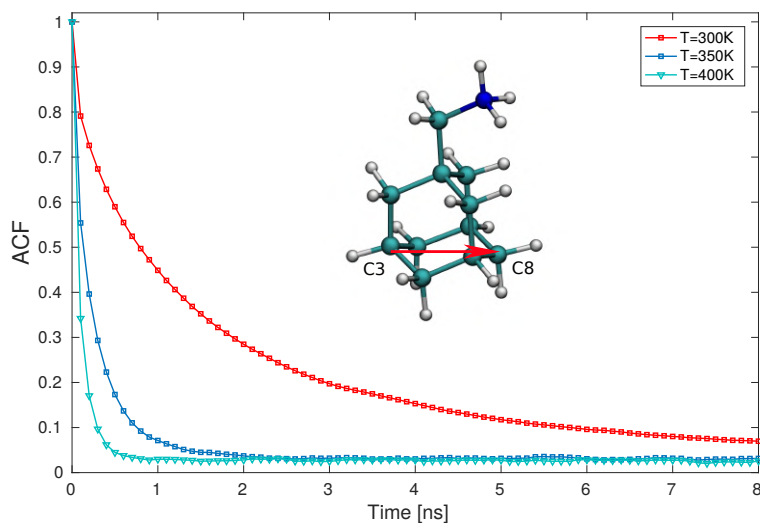


Figure 4.5 – **Time dependent autocorrelation function of the unit C3-C8 vectors of ligand A:** Image displays the behavior of ACF at different temperatures: 300K, 350K and 400K for $n=1$.

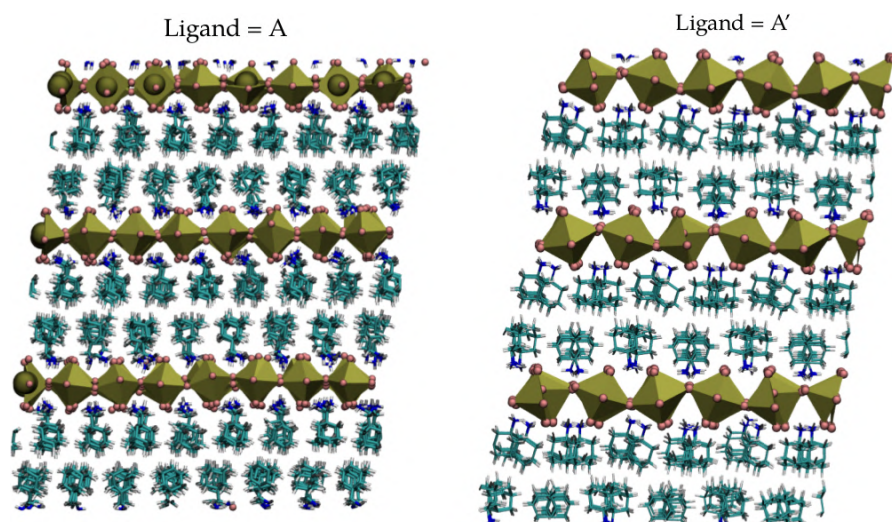


Figure 4.6 – **Comparison of equilibrated structures for 2D perovskite ($n=1$) with ligand-A and ligand-A'.** Lead (Pb^{2+}) ions are shown with golden balls, iodide (I^-) ions are displayed with pink spheres. Pb-I octahedra are displayed in golden color. Ligand A and A' are illustrated with balls and sticks. The images are generated with VMD.

Ligand A'

I follow a similar procedure as described in the previous section. Concerning structural differences between systems A with respect to A', it is interesting to observe a significant mutual tilt between adjacent Pb-I octahedra with ligand A' that is absent or less pronounced for ligand A. This behavior has also been observed in another study of rigid spacers from Mitzi and co-worker [29]. Furthermore, due to the higher rigidity of ligand A', the configuration of the ligand is more random, as shown in **Fig. 4.6**.

In order to gain a first indication of the thermal stability of the structures, I also performed classical MD simulations at higher temperatures (more than 400K). In the case of ligand A', I find that the corner-sharing network of Pb-I octahedra slowly starts to transform into edge-sharing configurations, which does not occur in the case of ligand A. This could indicate that the experimentally observed structures for 2D perovskites with ligand A' might be a mixture of corner and edge-sharing octahedra, which might lead to lower efficiencies than 2D perovskites with ligand A.

4.6 Mixture of 2-phenylethylammonium and 2-(perfluorophenyl)ethylammonium

One of the most widely employed organic moieties for layered perovskites is 2-phenylethylammonium (PEA^+) which interacts with the PbI_6^{4-} octahedra slabs via ion pairing and hydrogen bonding through the ammonium termini ($-\text{NH}_3^+$). In this project, fluoroarenes, such as 2-(perfluorophenyl) ethylammonium (FEA^+) are added along with PEA^+ . The presence of fluoroarene moieties could further contribute to the hydrophobicity of the material, improving its resilience to moisture. At the same time, fluoroarene anion- π interactions could also reduce halide ion migration, increasing the stability under device operating conditions. Therefore, supramolecular π -assemblies of arenes and fluoroarenes could be used to control the properties of hybrid perovskites and their composites, although they remain under-exploited in this context.

Here, I use molecular simulations to elucidate the atomic-level structure of this mixed cations in a model system that consists of PEA^+ and/or FEA^+ molecules (S^+) in a typical layered low-dimensional perovskite of S_2PbI_4 ($n = 1$) composition[219]. First, trial structures were generated by selecting low-energy structures from MD simulations (detailed in the Appendix). Based on previously reported crystal structures, two different relative orientations of the molecule's aromatic rings were considered: the "twisted" structure (**Fig. 4.7a**), with a twist between the aromatic rings in the two opposing layers and the "parallel" structure (**Fig. 4.7b**), with aromatic rings from opposite layers aligned in parallel planes at 180° between the layers. For $(\text{PEA})_2\text{PbI}_4$, the twisted structure has a lower energy than the parallel structure (see **Table 4.1**), which is in agreement with the reported single crystal structure (CCDC no. 1542461) [220].

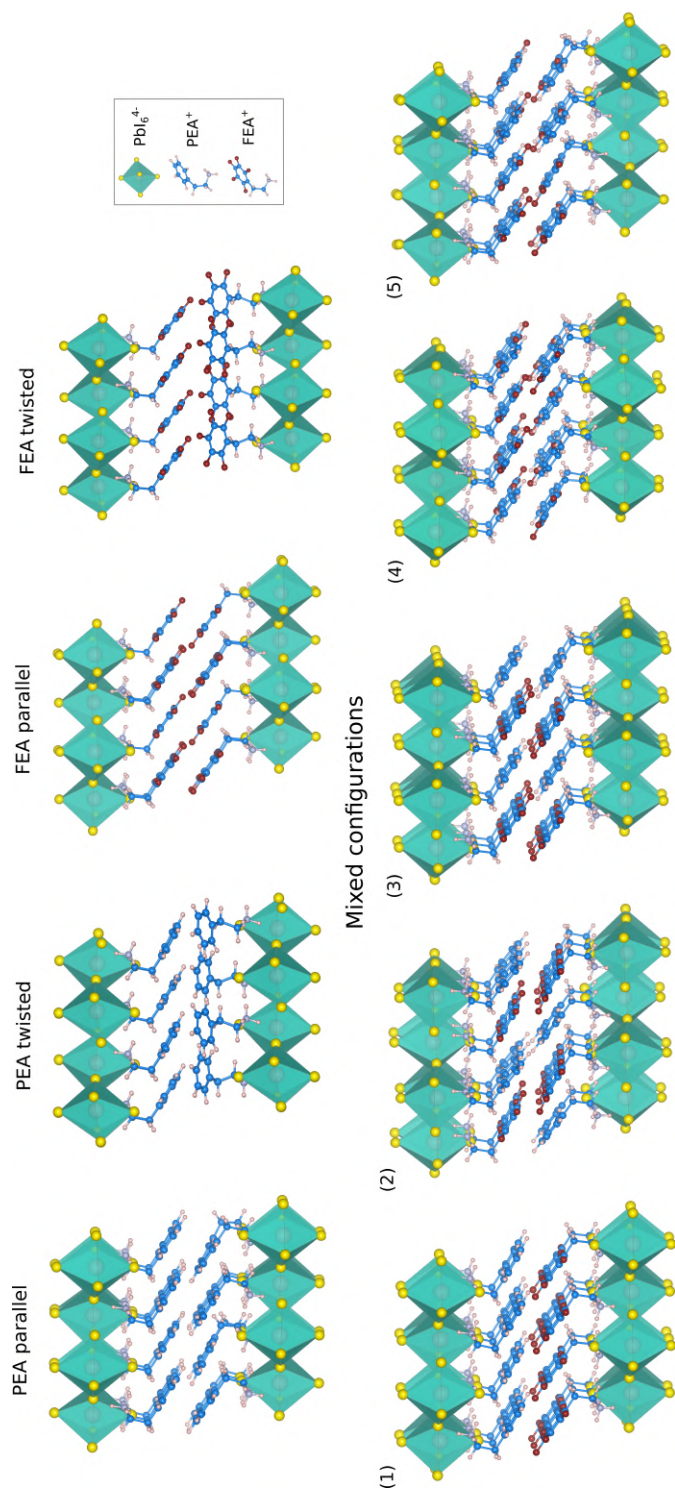


Figure 4.7 – **Trial structures of layered perovskites:** Top panel shows the twisted and parallel relative orientations of the aromatic rings in adjacent layers. Bottom panel is a schematic of different possible arrangements (1–5) of PEA^+ and FEA^+ molecules on the two opposing lattices representing the spacer bilayer within the layered perovskite.

In contrast, for $(\text{FEA})_2\text{PbI}_4$, the parallel structure was found to have lower energy than the parallel structure.

For the mixed $(\text{PF})_2\text{PbI}_4$ layered perovskite, there could be many possible arrangements of the PEA^+ and FEA^+ spacers. I have considered the simpler representations of spacer cations to form five trial structures (1–5, **Fig. 4.7**). In structure 1, each face comprises only a single type of spacer, while structures 2 and 3 have “checkerboard” arrangements of the cations on each face. In structure 2, the arrangements are offset so that unlike spacers are opposite each other (i.e., PEA^+ is opposite FEA^+), while structure 3 has alike spacers opposing. Finally, structures 4 and 5 have striped arrangements of the spacers on each face with unlike and like-pairing arrangements of the opposing spacers, respectively. In addition, I also consider a segregated model, where the energies are calculated for the separate pure twisted $(\text{PEA})_2\text{PbI}_4$ and parallel $(\text{FEA})_2\text{PbI}_4$ structures, to imitate the environments in a nanoscale segregated structure that would form as a result of predominantly narcissistic self-sorting.

Table 4.1 compares the relative energies of five mixed $(\text{PF})_2\text{PbI}_4$ structures and the segregated model with the pure $(\text{PEA})_2\text{PbI}_4$ and $(\text{FEA})_2\text{PbI}_4$ structures. The lowest energy was found for a segregated model which is in agreement with the experimental observations from experimental collaborators. As a result, the photovoltaic performance of the mixed system could be affected as compared to the pure system through a synergistic effect.

Table 4.1 – DFT energy comparison of twisted and parallel structures for $(\text{FEA})_2\text{PbI}_4$, $(\text{PEA})_2\text{PbI}_4$, and configurations 1–5 of $(\text{PF})_2\text{PbI}_4$ ($\text{PF} = 1:1 \text{ PEA}^+:\text{FEA}^+$; shown in Figure 5 in the main text). The energy of the segregated model is the average of the lowest energy $(\text{FEA})_2\text{PbI}_4$ and $(\text{PEA})_2\text{PbI}_4$ structures.

	DFT energy [eV/f.u.]	Relative energy [eV/f.u.]
$(\text{FEA})_2\text{PbI}_4$		
<i>Twisted</i>	-15276.3635210	0.175
<i>Parallel</i>	-15276.5384697	0.000
$(\text{PEA})_2\text{PbI}_4$		
<i>Twisted</i>	-8711.5987783	0.000
<i>Parallel</i>	-8711.5641965	0.035
$(\text{PF})_2\text{PbI}_4$		
1	-11994.2329298	0.000
2	-11993.8457719	0.387
3	-11993.9927588	0.240
4	-11993.9960029	0.237
5	-11993.9259885	0.307
Segregated model	-11994.0686240	0.165

5 General Conclusions

During my Ph.D. thesis, I contributed to the progress of halide perovskite research: enhancing the efficiency and stability by understanding the fundamentals of their crystallization process. I studied nucleation and growth from solution, solid-solid phase transition, and low-dimensional halide perovskites. Moreover, I predicted new polymorphs of halide perovskites which could play an important role in the crystallization process and can be of potential interest for making PSCs, LEDs, photo-detectors, and passivating surface defects. My results revealed the molecular level details of the phase transitions and effects of the additives for the synthesis and stabilization of the most efficient FAPbI₃ perovskite.

I started from the original MAPbI₃ perovskite. I revealed the formation mechanism of intermediate colloidal clusters and identified the key role of monovalent cations in the nucleation process. Most importantly, for the first time in all atomistic simulations, I nucleated such a complex hybrid organic-inorganic material from its homogeneous solution. I collaborated with experimentalists and utilized the fundamental insights to design a new synthesis process for a rational control over the grain size in thin-films.

After this study, I have been focused on the most important perovskite used to make record-breaking PSCs: FAPbI₃. In general, highly efficient metastable α -FAPbI₃ can only be formed above $\sim 150^\circ$. In contrast to this common belief, I discovered a new path to the low-temperature formation of phase-pure α -FAPbI₃. From the successful molecular simulations of the two-step process, I was able to show that FAI can directly react with PbI₂ to form a primary metastable phase that can be directly converted to α -FAPbI₃ via Ostwald ripening, therefore avoiding the formation of δ -FAPbI₃. Once again, I found that monovalent cations are important for the formation of α -FAPbI₃, meaning insufficient availability of FAI might result in incomplete conversion and formation of δ phase, whereas the abundance of FAI could help in the formation of α phase. I collaborated with experimental groups, and first, we proved that indeed a low-temperature formation of phase-pure α -FAPbI₃ is possible. This we demonstrated via both *in-situ* and *ex-situ* XRD measurements of two-step process. After I corroborated my theoretical results, I conceived and conceptualized a new experimental methodology to make the thin-films of the phase-pure α -FAPbI₃. Together with the experimental collaborators, we

systematically designed a highly porous PbI_2 morphology which could facilitate the diffusion of FAI for a complete conversion. Lastly, we made thin-films of the phase-pure α -FAPbI₃. In the race of making record-breaking PSCs with α -FAPbI₃, fundamental questions on the stability of the metastable α phase have remained unanswered ever since the experimental community has started to make α -phase based electronics. I calculated the energy barrier for the phase transition between α and δ phases of FAPbI₃. I found that they are separated by an energy barrier of ~ 0.7 eV, hence proving that α -FAPbI₃ is a kinetically stable material.

Apart from these rewarding fundamental aspects of crystallization, I studied the impact of different additives and solvents on the formation and stabilization of α -FAPbI₃. Importantly, my simulations uncovered the role of pseudo-halide additives (SCN^- and HCOO^-) to make high-efficiency PSCs. I realized that the smaller SCN^- and HCOO^- anions are not likely to be doped into the lattice; however they impact the crystallization process. My calculations illustrated that comparatively higher binding affinities of pseudo-halides towards the Pb^{2+} , and FA^+ cations could help in breaking and prohibiting the formation of face-sharing Pb-I octahedra, which are building blocks of the δ -phase. The subsequent simulation results explained the benefits of the passivation of harmful iodide vacancies on the surface and grain boundaries with SCN^- and HCOO^- . Moreover, while studying the effect of different solvents on the crystallization process, my simulations explained the atomic details of mixing a low-toxicity solvent (THF) in the conventional recipe. From quantifying the binding energies and coordination chemistry of different solute-solvent complexes, we learned that mixing THF and DMF/DMSO can effectively regulate the thin-film thickness and minimize the raw material waste during coating processes preserving the efficiency. Lastly, I successfully predicted the crystal structures of low-dimensional perovskites, which are used to produce highly stable PSCs, LEDs, and transistors.

Future direction

PSCs are now moving towards commercialization. Although record efficiencies are still increasing, the main research focus has been shifting towards reproducing the small area PCEs on the industrial scale large surface area solar panels. Popular manufacturing methodologies such as solution processing, solid-solid two-step conversion, and other coating techniques have many problems while reproducing and up-scaling small area PCEs to the large area. Moreover, the limited stability and potential toxic Pb leakage during operational conditions are serious challenges that must be addressed. I believe precise control over final morphology will solve these problems and contribute to the rapid industrialization of halide perovskites.

My research allowed a better understanding of the atomic-level details of the crystallization of halide perovskites. However, I could only qualitatively and partially understand the nucleation, growth, and polymorphism in these highly complex materials. In the future, I believe it is essential to first lay out a complete phase diagram of these materials and calculate the nucleation rates and mechanism of important perovskite polymorphs from the molecular sim-

ulations and state-of-the-art experimental recipes. Also, it is equally important to control the shape and size of the growing crystals. To achieve these goals, a great deal of new simulations methodologies need to be developed. I also believe future simulations will help in replacing traditional DMF and DMSO solvents with new suitable solvents/additives to make excellent quality and stable perovskites.

A An appendix

A.1 Single-step process

Simulation-(B)

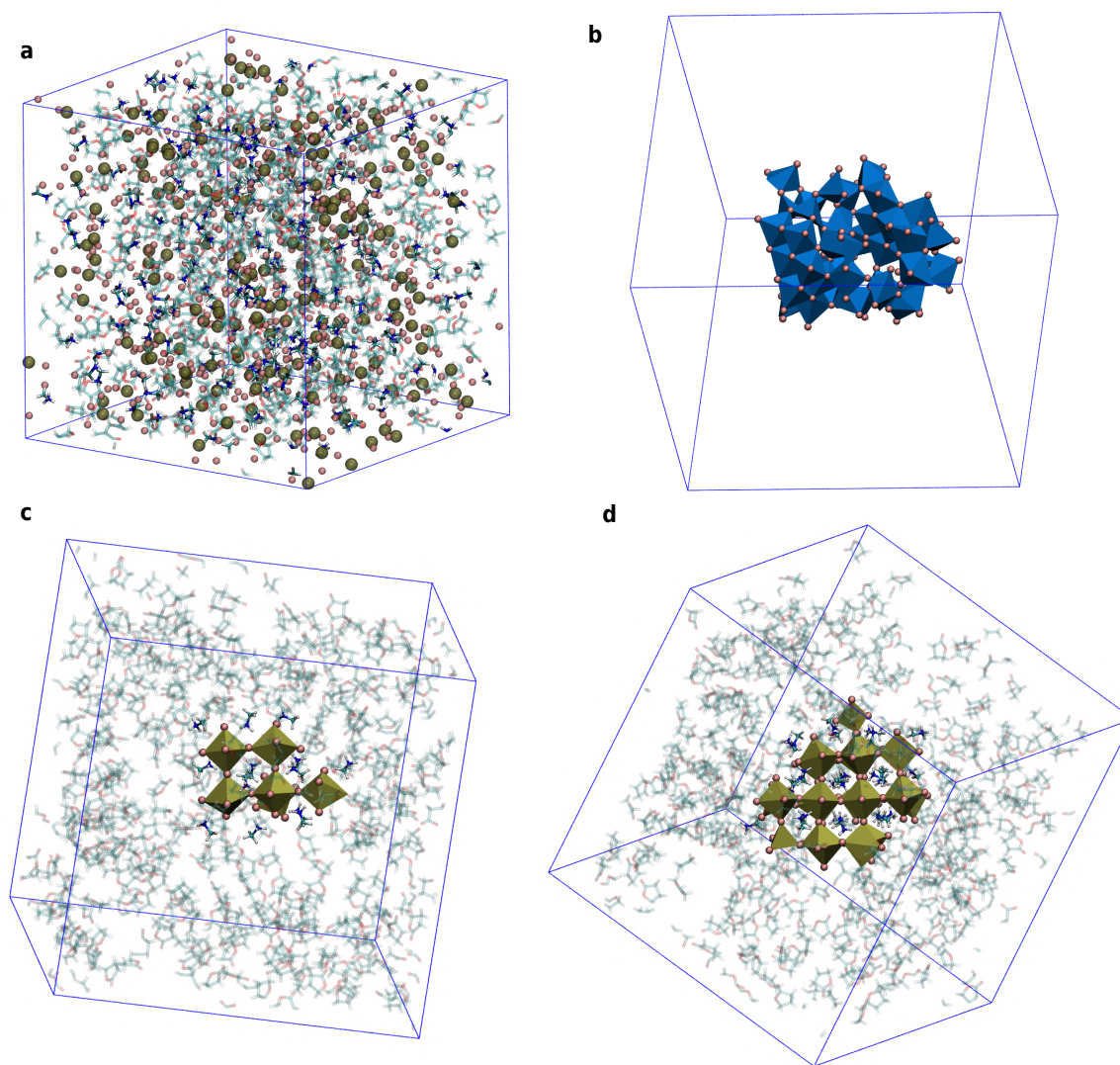


Figure A.1 – **Illustration of the full nucleation pathway for simulation-(B):**. Pb-I complexes are shown as golden and blue polyhedra with Pb²⁺ in the center and I⁻ on the corners. I⁻ is shown as pink spheres. MA⁺ ions are shown with ball and sticks. Snapshot (a) represents the initial solution of MA⁺, I⁻ and Pb²⁺ in GBL. GBL molecules are represented with ball and stick model and shown as semi-transparent to visualize the random distribution of Pb²⁺, I⁻ and MA⁺ in solution. Snapshot (b) represents the intermediate cluster formation of edge-sharing [PbI₆]⁴⁻ octahedra. Snapshot (c) shows the first perovskite nucleus observed in the solution. Snapshot (d) shows the largest perovskite crystal in this simulations. All the images of these snapshots are generated with VMD-1.9.2.[119]

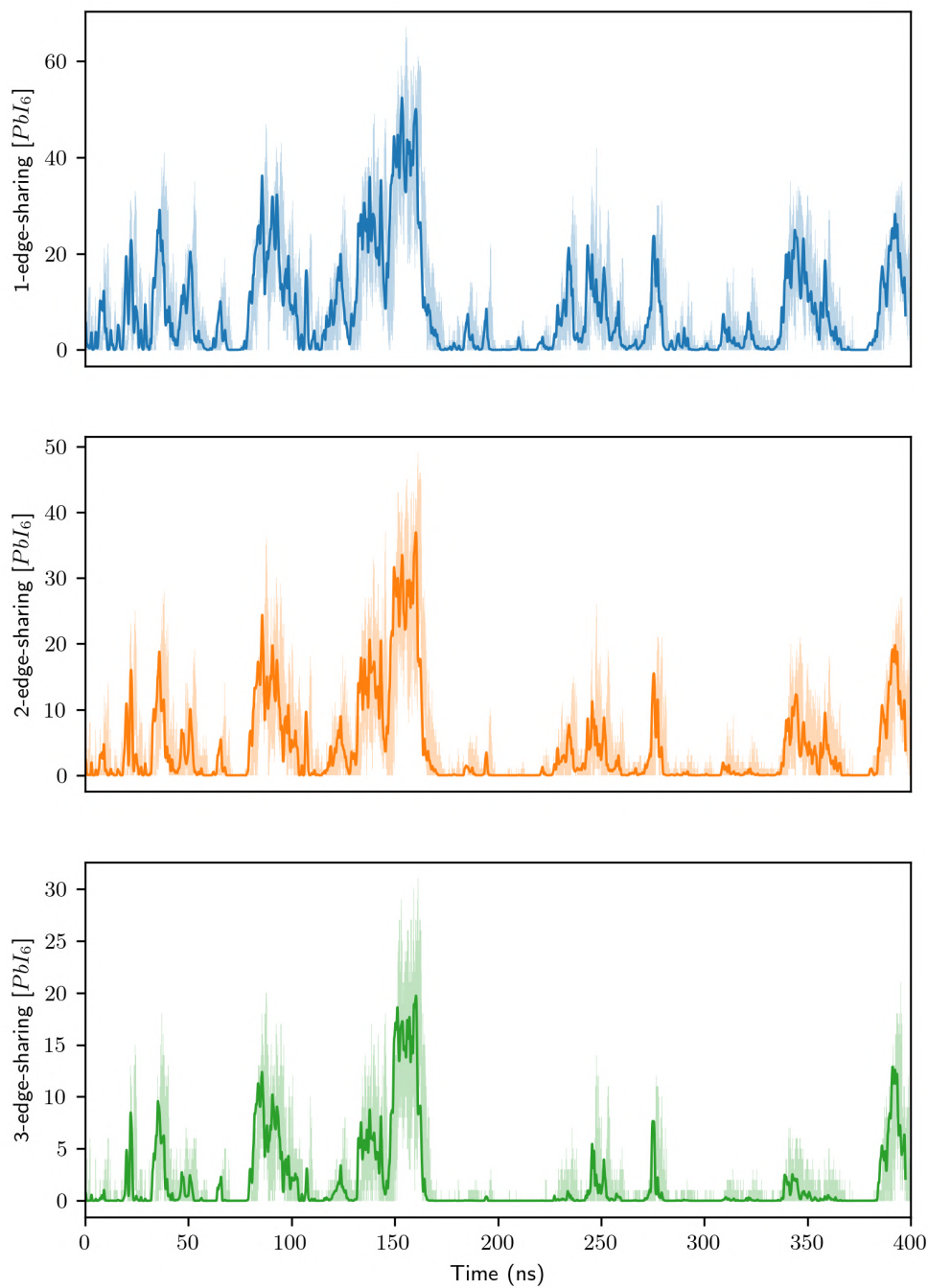


Figure A.2 – **Analysis of edge-sharing octahedra:** Number of edge-sharing octahedra as a function of simulation time in simulation (A)

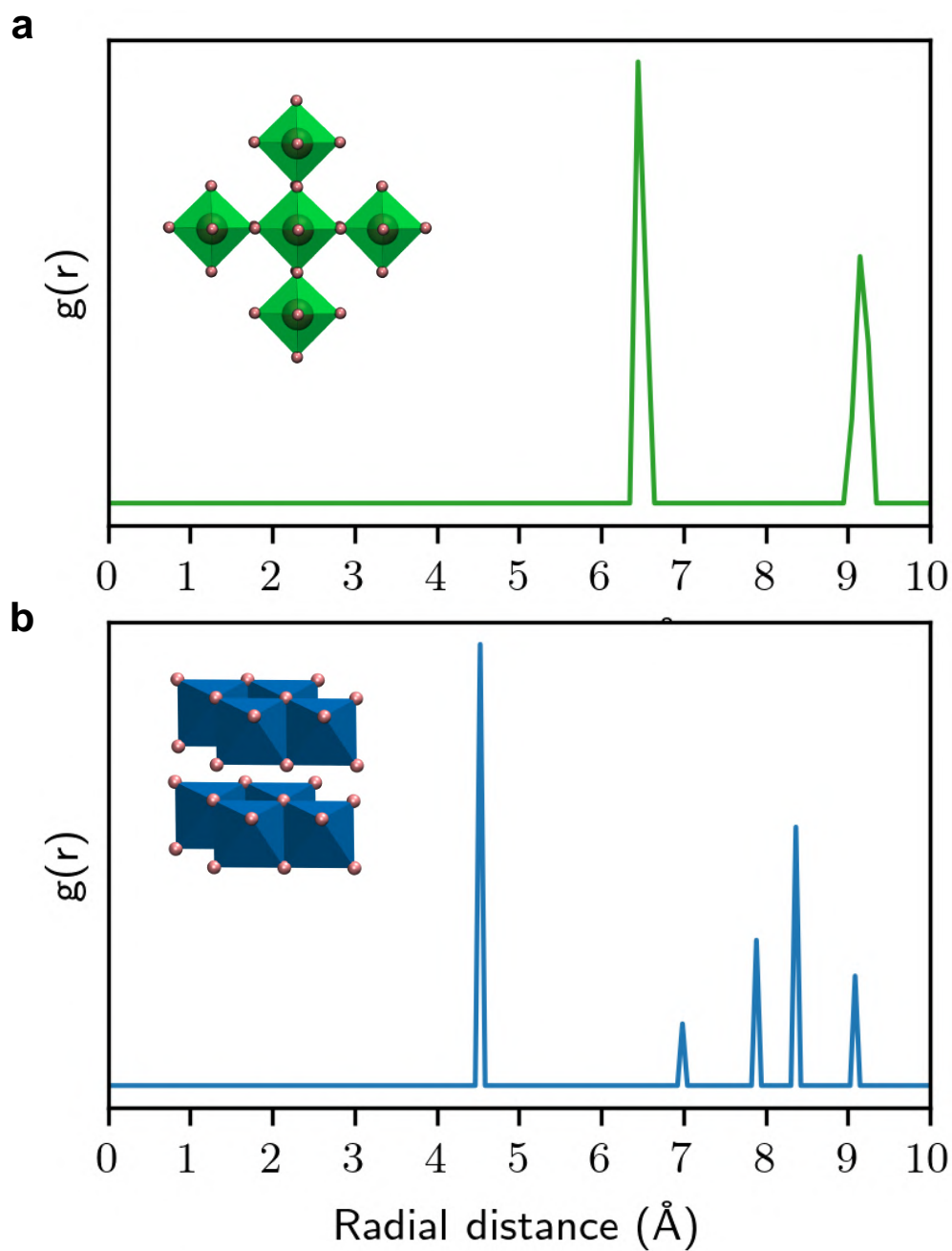


Figure A.3 – Top panel is the $g(r)$ of Pb^{2+} - Pb^{2+} in MAPI cubic perovskite and bottom panel is the $g(r)$ of Pb^{2+} - Pb^{2+} in crystalline PbI_2

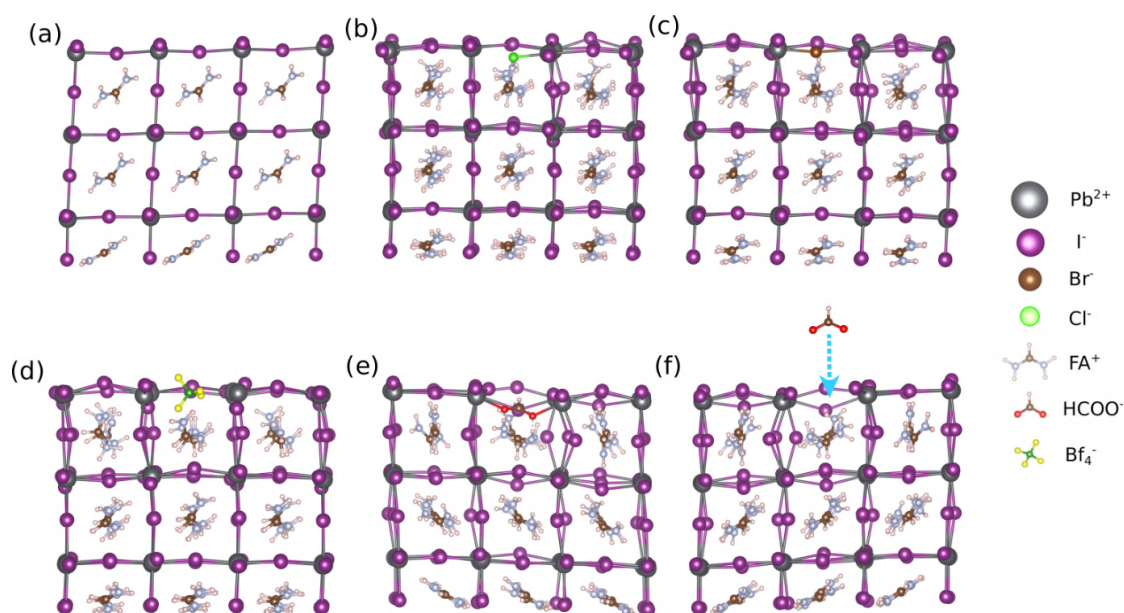


Figure A.4 – DFT relaxed slabs of FAPbI₃ with different anions adsorbed at the iodide vacancy site on the surface: (a) pure FAPbI₃ slab structure with Pb-I terminated surface on top and FA-I terminated surface on bottom side, (b) front view of the Cl⁻ passivated surface, (c) Br⁻ passivated surface, (d) BF₄⁻ passivated surface, (e) HCOO⁻ passivated. (f) illustrates the iodide vacancy passivation with HCOO⁻. All chemical species are shown with balls and sticks representation. Pb²⁺ ions are shown with the large brown coloured spheres, I⁻ with violet, oxygen atoms with red, carbon atoms with dark brown, nitrogen atoms with light blue, Br⁻ with reddish brown, Cl⁻ with light green, boron atoms with dark green, fluorine atoms with yellow and hydrogen atoms are represented with white spheres.

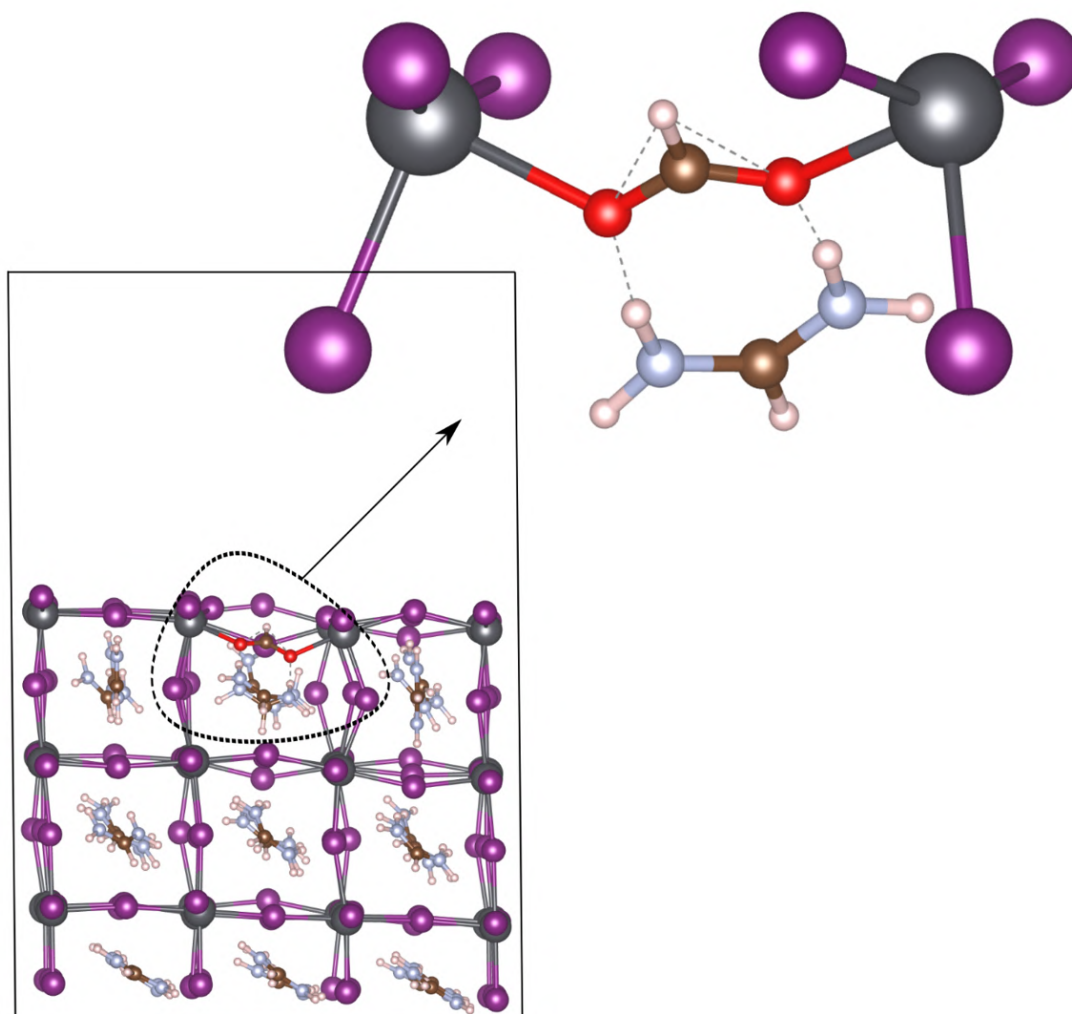


Figure A.5 – DFT relaxed FAPbI_3 slab HCOO^- adsorbed at the iodide vacancy site on the Pb-I terminated surface. All chemical species are shown with balls and sticks representation. Pb^{2+} ions are shown with the large brown coloured spheres, I^- with violet, oxygen atoms with red, carbon atoms with dark brown, nitrogen atoms with light blue and hydrogen atoms are represented with white spheres.

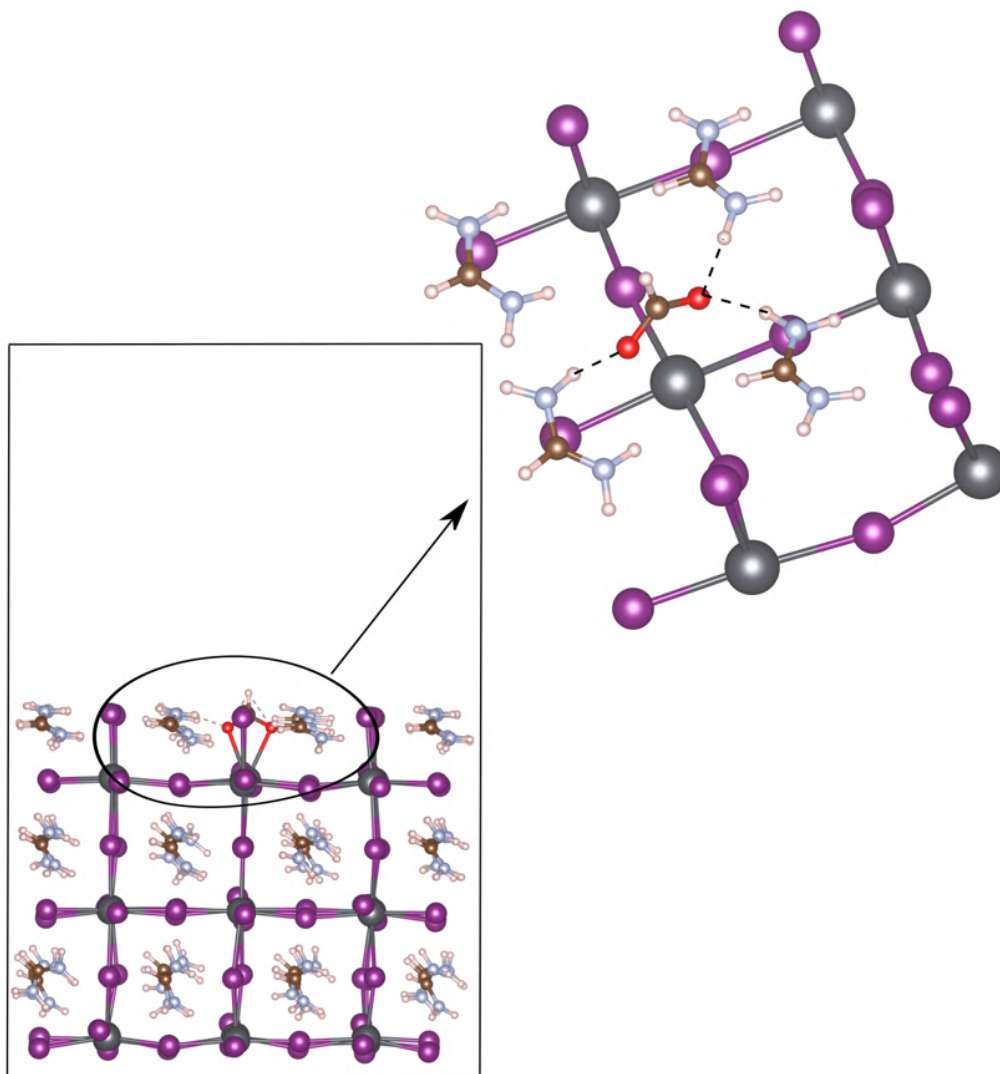


Figure A.6 – DFT relaxed FAPbI_3 slab HCOO^- adsorbed at the iodide vacancy site on with FA-I terminated surface. All chemical species are shown with balls and sticks representation.

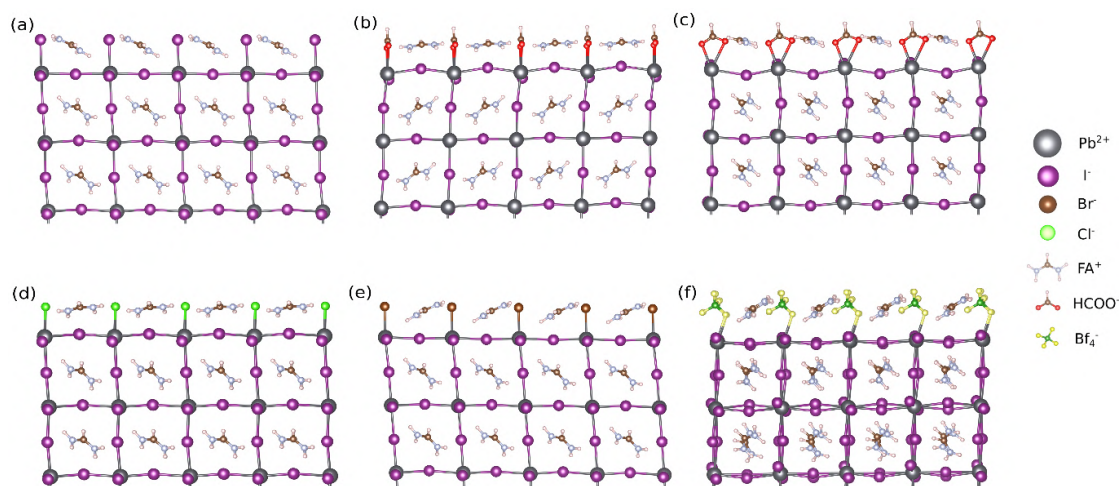


Figure A.7 – DFT relaxed slabs of FAPbI_3 with different anions on the surface: (a) pure FAPbI_3 slab structure with FA-I termination on top and Pb-I termination on bottom side, (b) front view of the COOH^- passivated surface, (c) side view of the COOH^- passivated surface, (d) Cl^- passivated surface, (e) Br^- passivated and (f) BF_4^- passivated surface.

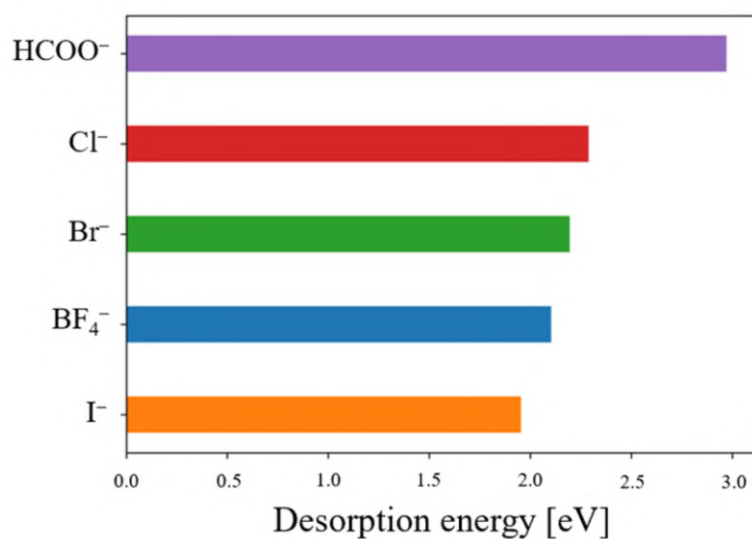


Figure A.8 – Desorption energies of FA^+ cations on different passivated surfaces.

A.2 Two-step process

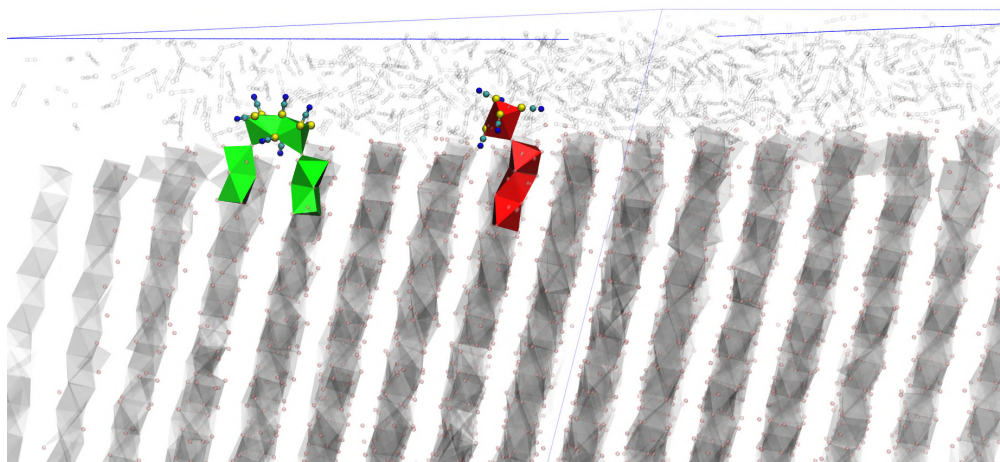


Figure A.9 – **Surface structures:** A zoomed-in view of the final configuration of corner-sharing structures on the interface.

A.3 Quasi-2D perovskites

A.3.1 Guanine

Methods:

Classical MD simulations: Supercells discussed in this work are made of 256 units of GA_2PbI_4 ($n=1$) and 216 units of $\text{GA}_2\text{FAPb}_2\text{I}_6$ ($n=2$). Systems used for electronic structure calculations constructed with 8 units of GA_2PbI_4 ($n=1$) and 16 units of $\text{GA}_2\text{FAPb}_2\text{I}_6$ ($n=2$). Initial DJ structures were build with VMD software by placing the guanine cations between layers of Pb-I octahedra and 3D structure of FAPbI_3 . An available interatomic potential[188] was chosen for Pb and I. We have selected this potential as it represents both edge-sharing phase of PbI_2 and corner-sharing perovskite structure. Generalized amber force fields (GAFF) were parameterized for the guanine cations and formamidinium cations. Heterogeneous inorganic-organic parameters were appropriately chosen from literature. A 1.0 nm cutoff for nonbonded interactions was selected with three-dimensional periodic boundary conditions. Long range electrostatic interactions were treated with the particle-particle-particle-mesh Ewald method. SHAKE algorithm[126] was applied to constrain the bond length of hydrogen atoms. All simulations are performed with a time step of 2fs with the Large-scale Atomic/Molecular Massively Parallel Simulator(LAMMPS) code (31 Mar 2017)[127]. Each system was first minimized with a conjugate gradient algorithm with a tolerance of maximum residual force of 10^{-3} kcal/molÅ. After equilibration I optimize the structures in an isothermal-isobaric ensemble. A velocity rescaling thermostat [128] was used with a relaxation time of 0.1 ps. Parrinello-Rahman barostat [129] was employed to keep the pressure equal to standard atmospheric pressure with a relaxation time of 10ps. Triclinic variable cell barostat was applied to freely optimize the

lattice parameters. For optimization, I slowly increase the temperature from 0K to 300K in 10 ns. Later, we perform 5 ns simulations at a constant temperature of 300 K. In the end I quench the system to 0K to extract the final structure and lattice parameters.

DFT calculations: Electronic structure calculations were performed based on Generalized Gradient Approximation (GGA) of density functional theory (DFT) using the Quantum Espresso package [156] and Perdew–Burke–Ernzerhof functional revised for solids (PBEsol)[212]. Ultra-soft pseudo-potentials were used for valence-core electron interactions with a plane wave basis set of 40 Ry kinetic energy cutoff and 280 Ry density cutoff. The Brillouin zone was sampled by a 3x3x1 k-point in both cases.

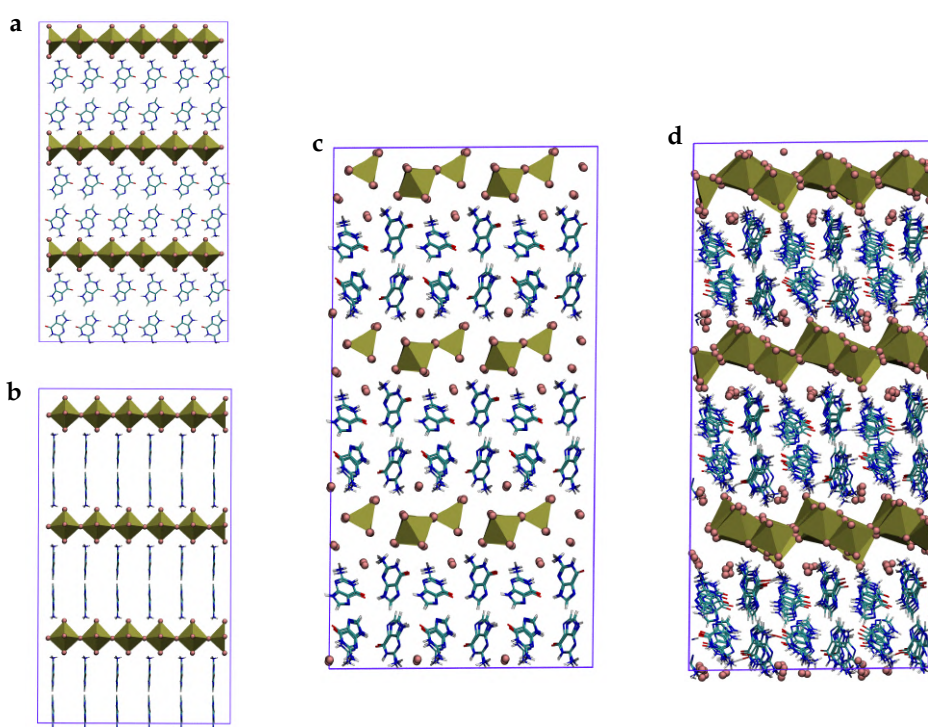


Figure A.10 – **Structure trial 1:** Images (a) and (b) are front and side view of initially estimated supercell for $n=1$. (c) illustrated the immediate structure after a few step after the start of classical MD simulations. (d) is the final structure. Lead (Pb^{2+}) ions are shown with golden balls, iodide (I^-) ions are displayed with pink spheres. Pb-I polyhedra are displayed in golden color. Guanine cations are illustrated with ball and sticks. Here we use the Gaussian optimized geometry of ligand.

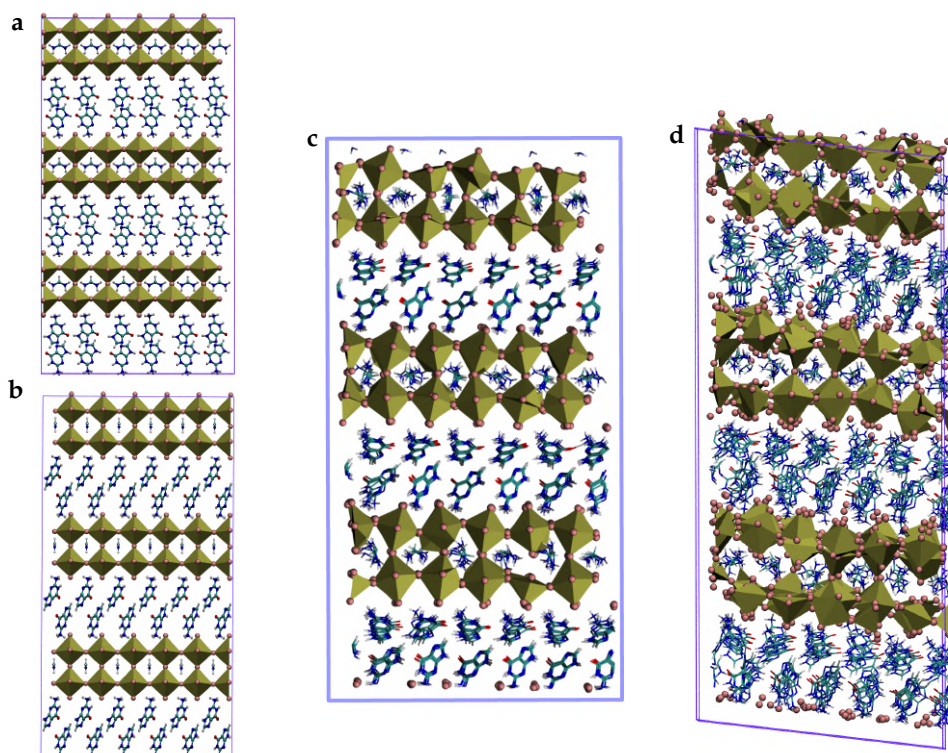


Figure A.11 – **Structure trial 2:** Images (a) and (b) are front and side view of initially estimated supercell for $n=2$. (c) illustrated the immediate structure after a few step after the start of classical MD simulations. (d) is the final structure. Lead (Pb^{2+}) ions are shown with golden balls, iodide (I^-) ions are displayed with pink spheres. Pb-I polyhedra are displayed in golden color.

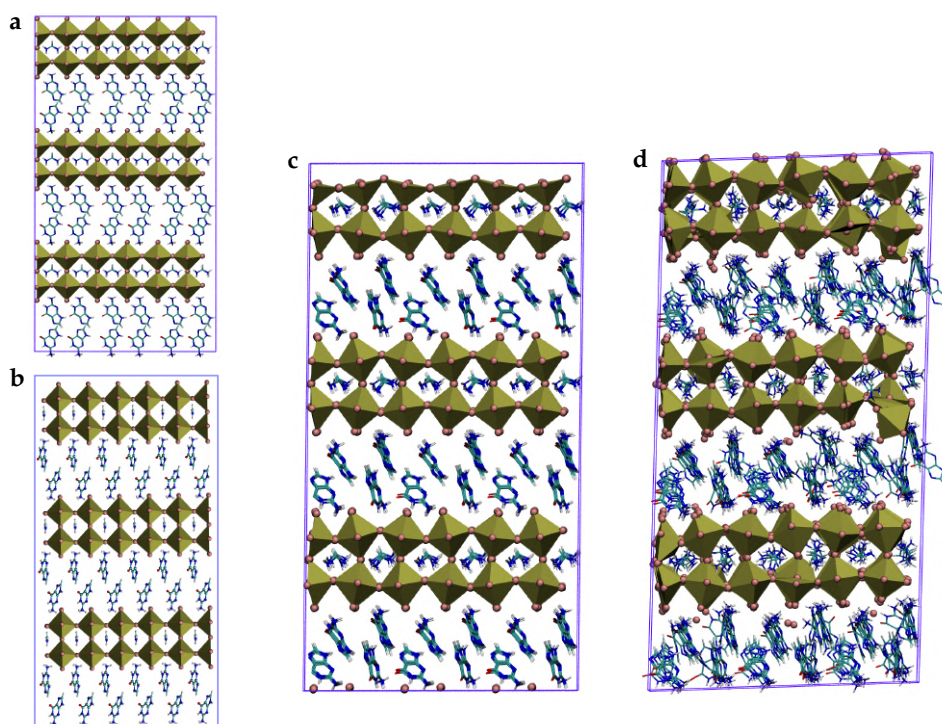


Figure A.12 – **Structure trial 3:** Images (a) and (b) are front and side view of initially estimated supercell for $n=2$. (c) illustrated the immediate structure after a few step after the start of classical MD simulations. (d) is the final structure. Lead (Pb^{2+}) ions are shown with golden balls, iodide (I^-) ions are displayed with pink spheres. Pb-I polyhedra are displayed in golden color. Guanine and formamidinium cations are illustrated with ball and sticks.

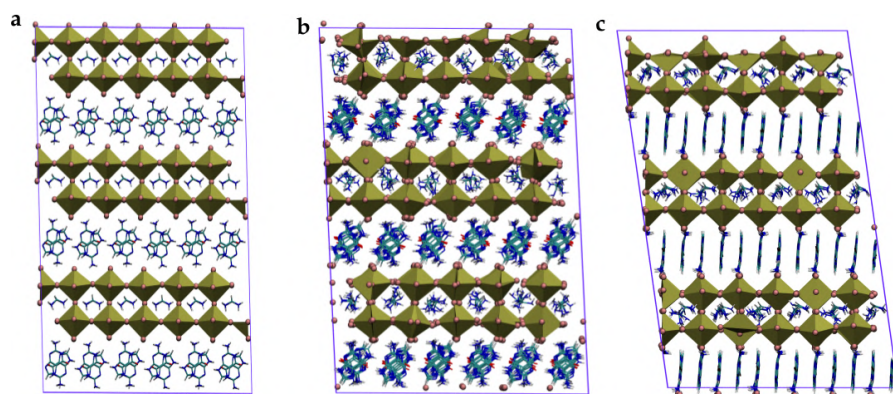


Figure A.13 – **Predicted structure:** (a) is the initially estimated supercell for $n=2$. (b) and (c) shows the finally optimized structure. Lead (Pb^{2+}) ions are shown with golden balls, iodide (I^-) ions are displayed with pink spheres. Pb-I polyhedra are displayed in golden color. Guanine and formamidinium cations are illustrated with ball and sticks.

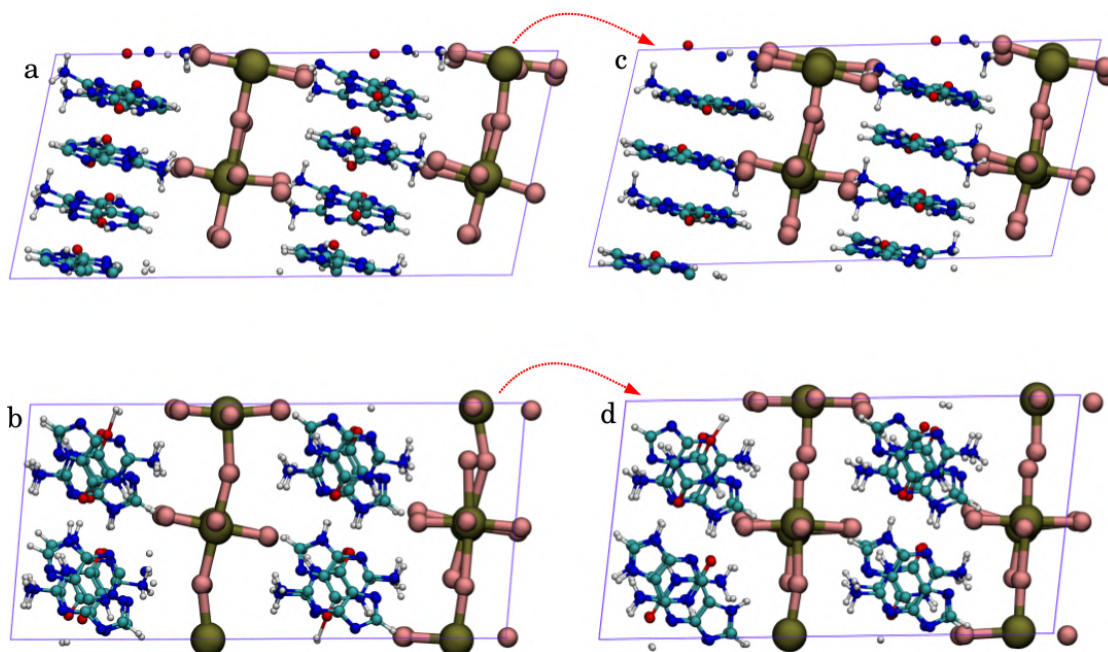


Figure A.14 – **DFT optimized structure for $n=1$** : Images (a) and (b) are front and side view of structures extracted from classical MD simulations. (c) and (d) show the front and side view of DFT optimized structures. Lead (Pb^{2+}) ions are shown with golden balls, iodide (I^-) ions are displayed with pink spheres. Guanine ions are illustrated with ball and sticks.

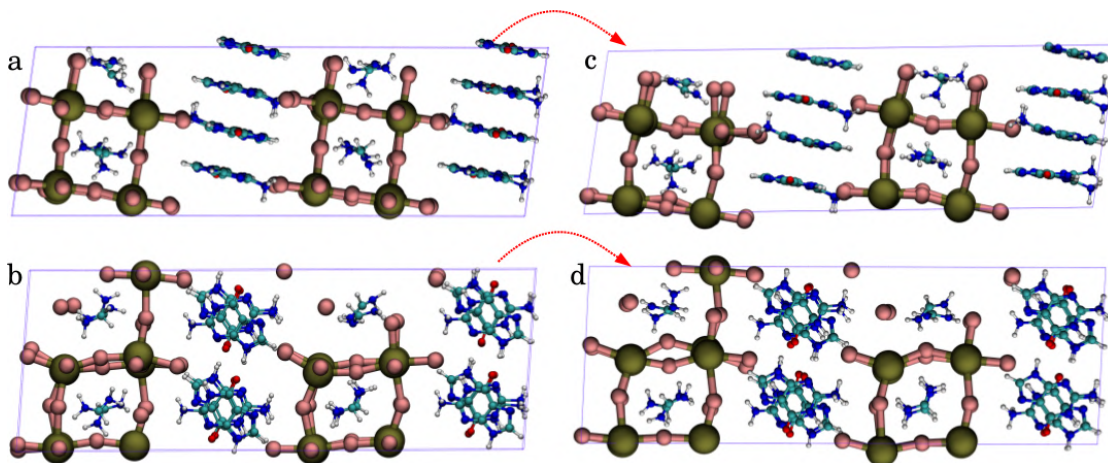


Figure A.15 – **DFT optimized structure for $n=2$** : Images (a) and (b) are front and side view of structures extracted from classical MD simulations. (c) and (d) show the front and side view of DFT optimized structures. Lead (Pb^{2+}) ions are shown with golden balls, iodide (I^-) ions are displayed with pink spheres. Guanine and formamidinium ions are illustrated with ball and sticks.

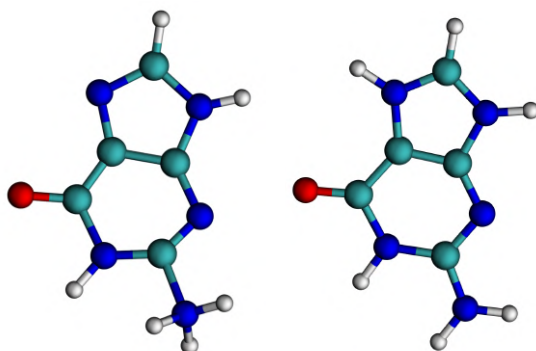


Figure A.16 – **Tautomers in DFT optimized structure for $n=1$** : Both molecules are illustrated with ball and sticks. Color coding of the balls is following: oxygen is red, carbons is greenish blue, nitrogens are dark blue and hydrogen are represented with white color smaller balls

A.3.2 PDMA

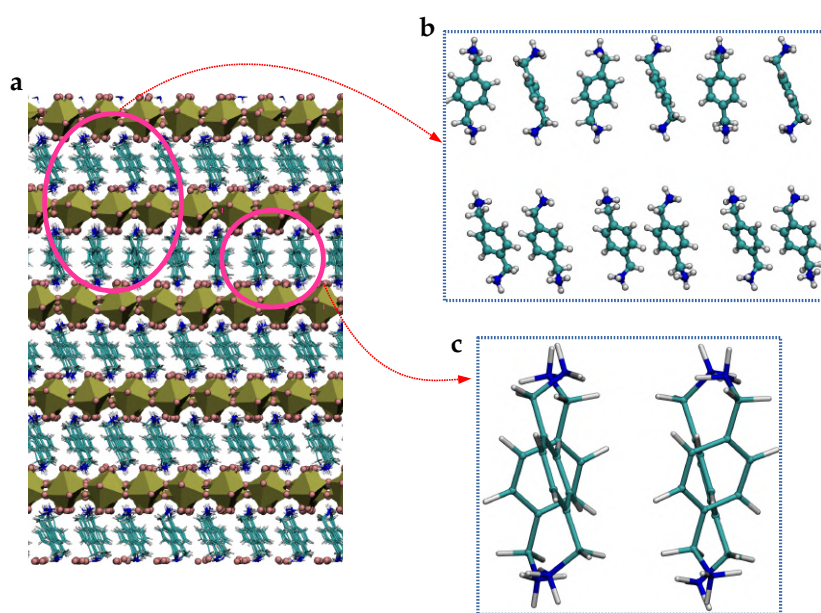


Figure A.17 – **Structrual analysis for ligand B**: (a) is the equilibrated geometry for $n=1$ (b) shows the arrangement of ligands between 2 layers. Image (c) highlights the T-shaped configuration in one of the layers in the 2D supercell. Ligand B is illustrated with balls and sticks. The images are generated with VMD.

A.3.3 (1-adamantyl)methan ammonium (A) & 1-adamantyl ammonium (A')

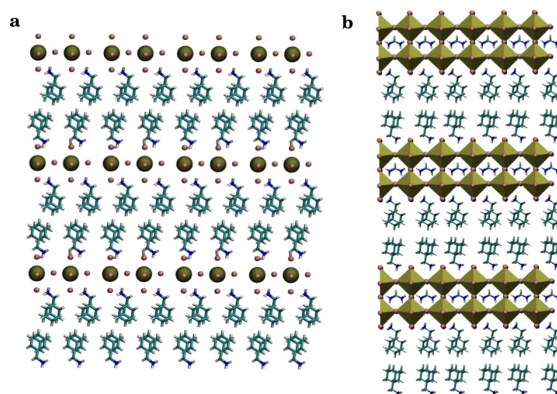


Figure A.18 – **Initial DJ structures with Ligand A:** Left panel shows the supercell for $n=1$ and right panel shows the initially build supercell for $n=2$. Lead (Pb^{2+}) ions are shown with golden balls, iodide (I^-) ions are displayed with pink spheres. Pb-I octahedra are displayed in golden color. Ligand A and formamidinium (FA^+) ions are illustrated with balls and sticks. The geometry for ligand A was obtained from DFT optimization with Gaussian software. Images are generated with VMD software.

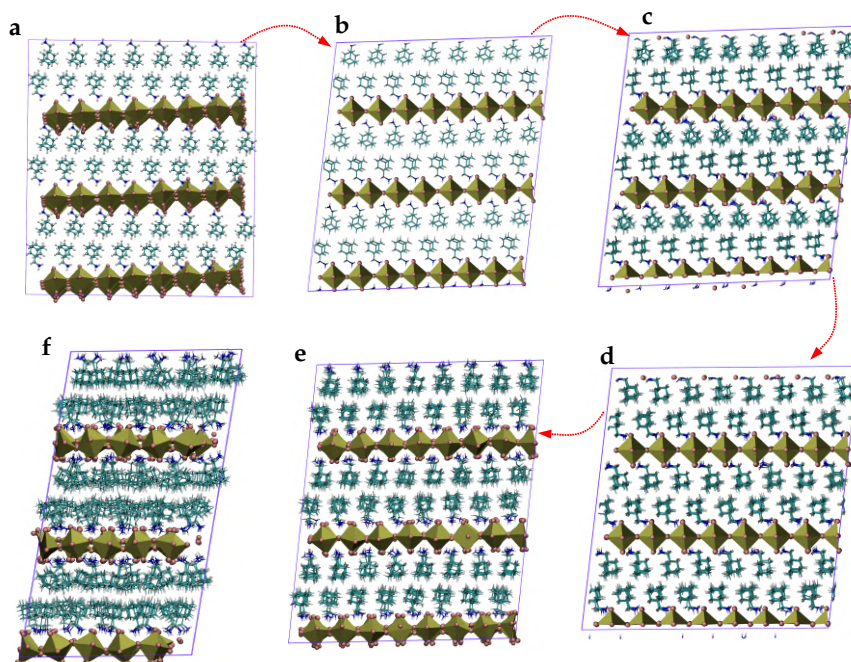


Figure A.19 – **Change in structure with increasing temperature:** Images (a) to (e) for $n=1$. Image (f) is the side view of image (e). Lead (Pb^{2+}) ions are shown with golden balls, iodide (I^-) ions are displayed with pink spheres. Pb-I octahedra are displayed in golden color. Ligand A is illustrated with balls and sticks. The images are generated with VMD.

Methods:

Supercells are made of 120 units of A_2PbI_4 , A'_2PbI_4 and $(PDMA)PbI_4$. Initial DJ structures were built with VMD by placing the ligands between layers of Pb-I octahedra. GAFF were parameterized for the ligands and formamidinium ions. I use the triclinic variable cell barostat in all of our simulations. With this setup, the temperature was slowly increased from 0K to T (temperature) in 10 ns. Then I perform 30 ns simulations at the constant temperature. To calculate ACF, MD simulations were performed for 5 different temperatures at 200K, 250K, 300K, 350K and 400K. These simulations were done to check the stability and calculations of rotational dynamics of ligands at different temperatures. In order to get the final structure, I quench the structure to 0K.

A.3.4 PEA and FEA mixtures

To propose possible trial arrangements for layered perovskites with PEA^+ , FEA^+ , and their mixtures, I first constructed different layered ($n = 1$) perovskite structures by placing PEA^+ and FEA^+ molecules between the layers of corner-sharing Pb-I octahedra. All of the initial mixed structures were built with VMD and based on previously published studies. In order to obtain relaxed geometries, I first performed classical molecular dynamics simulations followed by DFT calculations. For the classical MD simulations, I applied a similar methodology as presented in the section above. Generalized AMBER force fields (GAFF) were parameterized for PEA^+ and FEA^+ . I used 188 atoms supercells of $(FEA)_2PbI_4$ and $(PEA)_2PbI_4$ structures and 376 atoms supercells for mixed configurations. From these simulations we could observe many different configurations. However, I systematically classify the relevant configurations and select five different structures which take into account possible mixed configurations of PEA^+ and FEA^+ , as described in the chapter 4. The relative energies do not include finite temperature effects.

Bibliography

1. Kojima, A., Teshima, K., Shirai, Y. & Miyasaka, T. Organometal Halide Perovskites as Visible-Light Sensitizers for Photovoltaic Cells. en. *Journal of the American Chemical Society* **131**, 6050–6051. ISSN: 0002-7863, 1520-5126. <https://pubs.acs.org/doi/10.1021/ja809598r> (2022) (May 2009).
2. Lee, M. M., Teuscher, J., Miyasaka, T., Murakami, T. N. & Snaith, H. J. Efficient Hybrid Solar Cells Based on Meso-Superstructured Organometal Halide Perovskites. en. *Science* **338**, 643–647. ISSN: 0036-8075, 1095-9203. <https://www.science.org/doi/10.1126/science.1228604> (2022) (Nov. 2012).
3. Im, J.-H., Lee, C.-R., Lee, J.-W., Park, S.-W. & Park, N.-G. 6.5% efficient perovskite quantum-dot-sensitized solar cell. en. *Nanoscale* **3**, 4088. ISSN: 2040-3364, 2040-3372. <http://xlink.rsc.org/?DOI=c1nr10867k> (2022) (2011).
4. Kim, H.-S. *et al.* Lead Iodide Perovskite Sensitized All-Solid-State Submicron Thin Film Mesoscopic Solar Cell with Efficiency Exceeding 9%. en. *Scientific Reports* **2**, 591. ISSN: 2045-2322. <http://www.nature.com/articles/srep00591> (2022) (Dec. 2012).
5. Hao, F., Stoumpos, C. C., Cao, D. H., Chang, R. P. H. & Kanatzidis, M. G. Lead-free solid-state organic–inorganic halide perovskite solar cells. en. *Nature Photonics* **8**, 489–494. ISSN: 1749-4885, 1749-4893. <http://www.nature.com/articles/nphoton.2014.82> (2022) (June 2014).
6. Jeon, N. J. *et al.* Compositional engineering of perovskite materials for high-performance solar cells. en. *Nature* **517**, 476–480. ISSN: 0028-0836, 1476-4687. <http://www.nature.com/articles/nature14133> (2022) (Jan. 2015).
7. Saparov, B. & Mitzi, D. B. Organic–Inorganic Perovskites: Structural Versatility for Functional Materials Design. en. *Chemical Reviews* **116**, 4558–4596. ISSN: 0009-2665, 1520-6890. <https://pubs.acs.org/doi/10.1021/acs.chemrev.5b00715> (2022) (Apr. 2016).
8. Tan, Z.-K. *et al.* Bright light-emitting diodes based on organometal halide perovskite. en. *Nature Nanotechnology* **9**, 687–692. ISSN: 1748-3387, 1748-3395. <http://www.nature.com/articles/nnano.2014.149> (2022) (Sept. 2014).
9. Cao, Y. *et al.* Perovskite light-emitting diodes based on spontaneously formed submicrometre-scale structures. en. *Nature* **562**, 249–253. ISSN: 0028-0836, 1476-4687. <http://www.nature.com/articles/s41586-018-0576-2> (2022) (Oct. 2018).

10. Lin, K. *et al.* Perovskite light-emitting diodes with external quantum efficiency exceeding 20 per cent. en. *Nature* **562**, 245–248. ISSN: 0028-0836, 1476-4687. <http://www.nature.com/articles/s41586-018-0575-3> (2022) (Oct. 2018).
11. Rainò, G. *et al.* Superfluorescence from lead halide perovskite quantum dot superlattices. en. *Nature* **563**, 671–675. ISSN: 0028-0836, 1476-4687. <http://www.nature.com/articles/s41586-018-0683-0> (2022) (Nov. 2018).
12. Kagan, C. R., Mitzi, D. B. & Dimitrakopoulos, C. D. Organic-Inorganic Hybrid Materials as Semiconducting Channels in Thin-Film Field-Effect Transistors. en. *Science* **286**, 945–947. ISSN: 0036-8075, 1095-9203. <https://www.science.org/doi/10.1126/science.286.5441.945> (2022) (Oct. 1999).
13. Senanayak, S. P. *et al.* Understanding charge transport in lead iodide perovskite thin-film field-effect transistors. en. *Science Advances* **3**, e1601935. ISSN: 2375-2548. <https://www.science.org/doi/10.1126/sciadv.1601935> (2022) (Jan. 2017).
14. Luo, J. *et al.* Water photolysis at 12.3% efficiency via perovskite photovoltaics and Earth-abundant catalysts. en. *Science* **345**, 1593–1596. ISSN: 0036-8075, 1095-9203. <https://www.science.org/doi/10.1126/science.1258307> (2022) (Sept. 2014).
15. Wang, L., Xiao, H., Cheng, T., Li, Y. & Goddard, W. A. Pb-Activated Amine-Assisted Photocatalytic Hydrogen Evolution Reaction on Organic–Inorganic Perovskites. en. *Journal of the American Chemical Society* **140**, 1994–1997. ISSN: 0002-7863, 1520-5126. <https://pubs.acs.org/doi/10.1021/jacs.7b12028> (2022) (Feb. 2018).
16. Song, X. *et al.* Overall photocatalytic water splitting by an organolead iodide crystalline material. en. *Nature Catalysis* **3**, 1027–1033. ISSN: 2520-1158. <http://www.nature.com/articles/s41929-020-00543-4> (2022) (Dec. 2020).
17. Dou, L. *et al.* Solution-processed hybrid perovskite photodetectors with high detectivity. en. *Nature Communications* **5**, 5404. ISSN: 2041-1723. <http://www.nature.com/articles/ncomms6404> (2022) (Dec. 2014).
18. He, Y. *et al.* CsPbBr₃ perovskite detectors with 1.4% energy resolution for high-energy γ -rays. en. *Nature Photonics* **15**, 36–42. ISSN: 1749-4885, 1749-4893. <http://www.nature.com/articles/s41566-020-00727-1> (2022) (Jan. 2021).
19. Kim, G. *et al.* Impact of strain relaxation on performance of α -formamidinium lead iodide perovskite solar cells. en. *Science* **370**, 108–112. ISSN: 0036-8075, 1095-9203. <https://www.science.org/doi/10.1126/science.abc4417> (2022) (Oct. 2020).
20. Yoo, J. J. *et al.* Efficient perovskite solar cells via improved carrier management. en. *Nature* **590**, 587–593. ISSN: 0028-0836, 1476-4687. <http://www.nature.com/articles/s41586-021-03285-w> (2022) (Feb. 2021).
21. Jeong, J. *et al.* Pseudo-halide anion engineering for α -FAPbI₃ perovskite solar cells. en. *Nature* **592**, 381–385. ISSN: 0028-0836, 1476-4687. <http://www.nature.com/articles/s41586-021-03406-5> (2022) (Apr. 2021).

22. Kim, Y.-H. *et al.* Comprehensive defect suppression in perovskite nanocrystals for high-efficiency light-emitting diodes. en. *Nature Photonics* **15**, 148–155. ISSN: 1749-4885, 1749-4893. <http://www.nature.com/articles/s41566-020-00732-4> (2022) (Feb. 2021).
23. Mitzi, D. B., Feild, C. A., Harrison, W. T. A. & Guloy, A. M. Conducting tin halides with a layered organic-based perovskite structure. en. *Nature* **369**, 467–469. ISSN: 0028-0836, 1476-4687. <http://www.nature.com/articles/369467a0> (2022) (June 1994).
24. Im, J.-H., Chung, J., Kim, S.-J. & Park, N.-G. Synthesis, structure, and photovoltaic property of a nanocrystalline 2H perovskite-type novel sensitizer (CH₃CH₂NH₃)PbI₃. en. *Nanoscale Research Letters* **7**, 353. ISSN: 1556-276X. <https://nanoscalereslett.springeropen.com/articles/10.1186/1556-276X-7-353> (2022) (Dec. 2012).
25. Etgar, L. *et al.* Mesoscopic CH₃NH₃PbI₃/TiO₂ Heterojunction Solar Cells. en. *Journal of the American Chemical Society* **134**, 17396–17399. ISSN: 0002-7863, 1520-5126. <https://pubs.acs.org/doi/10.1021/ja307789s> (2022) (Oct. 2012).
26. Chung, I., Lee, B., He, J., Chang, R. P. H. & Kanatzidis, M. G. All-solid-state dye-sensitized solar cells with high efficiency. en. *Nature* **485**, 486–489. ISSN: 0028-0836, 1476-4687. <http://www.nature.com/articles/nature11067> (2022) (May 2012).
27. Stoumpos, C. C., Malliakas, C. D. & Kanatzidis, M. G. Semiconducting Tin and Lead Iodide Perovskites with Organic Cations: Phase Transitions, High Mobilities, and Near-Infrared Photoluminescent Properties. en. *Inorganic Chemistry* **52**, 9019–9038. ISSN: 0020-1669, 1520-510X. <https://pubs.acs.org/doi/10.1021/ic401215x> (2022) (Aug. 2013).
28. Protesescu, L. *et al.* Nanocrystals of Cesium Lead Halide Perovskites (CsPbX₃, X = Cl, Br, and I): Novel Optoelectronic Materials Showing Bright Emission with Wide Color Gamut. en. *Nano Letters* **15**, 3692–3696. ISSN: 1530-6984, 1530-6992. <https://pubs.acs.org/doi/10.1021/nl5048779> (2022) (June 2015).
29. Liang, K., Mitzi, D. B. & Prikas, M. T. Synthesis and Characterization of Organic-Inorganic Perovskite Thin Films Prepared Using a Versatile Two-Step Dipping Technique. en. *Chemistry of Materials* **10**, 403–411. ISSN: 0897-4756, 1520-5002. <https://pubs.acs.org/doi/10.1021/cm970568f> (2022) (Jan. 1998).
30. Burschka, J. *et al.* Sequential deposition as a route to high-performance perovskite-sensitized solar cells. en. *Nature* **499**, 316–319. ISSN: 0028-0836, 1476-4687. <http://www.nature.com/articles/nature12340> (2022) (July 2013).
31. Era, M., Hattori, T., Taira, T. & Tsutsui, T. Self-Organized Growth of PbI₂-Based Layered Perovskite Quantum Well by Dual-Source Vapor Deposition. en. *Chemistry of Materials* **9**, 8–10. ISSN: 0897-4756, 1520-5002. <https://pubs.acs.org/doi/10.1021/cm960434m> (2022) (Jan. 1997).
32. Liu, M., Johnston, M. B. & Snaith, H. J. Efficient planar heterojunction perovskite solar cells by vapour deposition. en. *Nature* **501**, 395–398. ISSN: 0028-0836, 1476-4687. <http://www.nature.com/articles/nature12509> (2022) (Sept. 2013).

33. Momblona, C. *et al.* Efficient vacuum deposited p-i-n and n-i-p perovskite solar cells employing doped charge transport layers. en. *Energy Environ. Sci.* **9**, 3456–3463. ISSN: 1754-5692, 1754-5706. <http://xlink.rsc.org/?DOI=C6EE02100J> (2022) (2016).
34. Borchert, J. *et al.* Large-Area, Highly Uniform Evaporated Formamidinium Lead Triiodide Thin Films for Solar Cells. en. *ACS Energy Letters* **2**, 2799–2804. ISSN: 2380-8195, 2380-8195. <https://pubs.acs.org/doi/10.1021/acsenergylett.7b00967> (2022) (Dec. 2017).
35. Sharenko, A. & Toney, M. F. Relationships between Lead Halide Perovskite Thin-Film Fabrication, Morphology, and Performance in Solar Cells. en. *Journal of the American Chemical Society* **138**, 463–470. ISSN: 0002-7863, 1520-5126. <https://pubs.acs.org/doi/10.1021/jacs.5b10723> (2022) (Jan. 2016).
36. Salim, T. *et al.* Perovskite-based solar cells: impact of morphology and device architecture on device performance. en. *Journal of Materials Chemistry A* **3**, 8943–8969. ISSN: 2050-7488, 2050-7496. <http://xlink.rsc.org/?DOI=C4TA05226A> (2022) (2015).
37. Bi, D. *et al.* Efficient luminescent solar cells based on tailored mixed-cation perovskites. en. *Science Advances* **2**, e1501170. ISSN: 2375-2548. <https://www.science.org/doi/10.1126/sciadv.1501170> (2022) (Jan. 2016).
38. Yang, W. S. *et al.* Iodide management in formamidinium-lead-halide-based perovskite layers for efficient solar cells. en. *Science* **356**, 1376–1379. ISSN: 0036-8075, 1095-9203. <https://www.science.org/doi/10.1126/science.aan2301> (2022) (June 2017).
39. Snaith, H. J. Present status and future prospects of perovskite photovoltaics. *Nat. Mater.* **17**, 372–376. ISSN: 1476-1122 (2018).
40. Huang, H. *et al.* Colloidal lead halide perovskite nanocrystals: synthesis, optical properties and applications. en. *NPG Asia Materials* **8**, e328–e328. ISSN: 1884-4049, 1884-4057. <http://www.nature.com/articles/am2016167> (2022) (Nov. 2016).
41. Akkerman, Q. A., Rainò, G., Kovalenko, M. V. & Manna, L. Genesis, challenges and opportunities for colloidal lead halide perovskite nanocrystals. en. *Nature Materials* **17**, 394–405. ISSN: 1476-1122, 1476-4660. <http://www.nature.com/articles/s41563-018-0018-4> (2022) (May 2018).
42. Ball, J. M. & Petrozza, A. Defects in perovskite-halides and their effects in solar cells. en. *Nature Energy* **1**, 16149. ISSN: 2058-7546. <http://www.nature.com/articles/nenergy2016149> (2022) (Nov. 2016).
43. Snaith, H. J. *et al.* Anomalous Hysteresis in Perovskite Solar Cells. *J. Phys. Chem. Lett.* **5**, 1511–1515. ISSN: 1948-7185 (2014).
44. Eperon, G. E., Burlakov, V. M., Docampo, P., Goriely, A. & Snaith, H. J. Morphological Control for High Performance, Solution-Processed Planar Heterojunction Perovskite Solar Cells. en. *Advanced Functional Materials* **24**, 151–157. ISSN: 1616301X. <https://onlinelibrary.wiley.com/doi/10.1002/adfm.201302090> (2022) (Jan. 2014).

45. Shi, D. *et al.* Low trap-state density and long carrier diffusion in organolead trihalide perovskite single crystals. en. *Science* **347**, 519–522. ISSN: 0036-8075, 1095-9203. <https://www.science.org/doi/10.1126/science.aaa2725> (2022) (Jan. 2015).
46. Correa-Baena, J.-P. *et al.* Unbroken Perovskite: Interplay of Morphology, Electro-optical Properties, and Ionic Movement. en. *Advanced Materials* **28**, 5031–5037. ISSN: 09359648. <https://onlinelibrary.wiley.com/doi/10.1002/adma.201600624> (2022) (July 2016).
47. Shao, Y. *et al.* Grain boundary dominated ion migration in polycrystalline organic–inorganic halide perovskite films. en. *Energy & Environmental Science* **9**, 1752–1759. ISSN: 1754-5692, 1754-5706. <http://xlink.rsc.org/?DOI=C6EE00413J> (2022) (2016).
48. Hoke, E. T. *et al.* Reversible photo-induced trap formation in mixed-halide hybrid perovskites for photovoltaics. en. *Chemical Science* **6**, 613–617. ISSN: 2041-6520, 2041-6539. <http://xlink.rsc.org/?DOI=C4SC03141E> (2022) (2015).
49. Yang, J., Siempelkamp, B. D., Liu, D. & Kelly, T. L. Investigation of CH₃NH₃PbI₃ Degradation Rates and Mechanisms in Controlled Humidity Environments Using *in Situ* Techniques. en. *ACS Nano* **9**, 1955–1963. ISSN: 1936-0851, 1936-086X. <https://pubs.acs.org/doi/10.1021/nn506864k> (2021) (Feb. 2015).
50. Leguy, A. M. A. *et al.* Reversible Hydration of CH₃NH₃PbI₃ in Films, Single Crystals, and Solar Cells. en. *Chemistry of Materials* **27**, 3397–3407. ISSN: 0897-4756, 1520-5002. <https://pubs.acs.org/doi/10.1021/acs.chemmater.5b00660> (2021) (May 2015).
51. Aristidou, N. *et al.* Fast oxygen diffusion and iodide defects mediate oxygen-induced degradation of perovskite solar cells. en. *Nature Communications* **8**, 15218. ISSN: 2041-1723. <http://www.nature.com/articles/ncomms15218> (2021) (Aug. 2017).
52. Vincent, B. R., Robertson, K. N., Cameron, T. S. & Knop, O. Alkylammonium lead halides. Part 1. Isolated PbI₆⁴⁻ ions in (CH₃NH₃)₄PbI₆ • 2H₂O. en. *Canadian Journal of Chemistry* **65**, 1042–1046. ISSN: 0008-4042, 1480-3291. <http://www.nrcresearchpress.com/doi/10.1139/v87-176> (2022) (May 1987).
53. Yuan, Y. & Huang, J. Ion migration in organometal trihalide perovskite and its impact on photovoltaic efficiency and stability. *Accounts of chemical research* **49**, 286–293 (2016).
54. Kim, G. Y., Senocrate, A., Wang, Y.-R., Moia, D. & Maier, J. Photo-Effect on Ion Transport in Mixed Cation and Halide Perovskites and Implications for Photo-Demixing. *Angewandte Chemie International Edition* **60**, 820–826 (2021).
55. Kim, G. Y. *et al.* Large tunable photoeffect on ion conduction in halide perovskites and implications for photodecomposition. en. *Nature Materials* **17**, 445–449. ISSN: 1476-1122, 1476-4660. <http://www.nature.com/articles/s41563-018-0038-0> (2021) (May 2018).
56. Meloni, S. *et al.* Ionic polarization-induced current–voltage hysteresis in CH₃NH₃PbX₃ perovskite solar cells. en. *Nature Communications* **7**, 10334. ISSN: 2041-1723. <http://www.nature.com/articles/ncomms10334> (2021) (Apr. 2016).

57. Brennan, M. C., Draguta, S., Kamat, P. V. & Kuno, M. Light-Induced Anion Phase Segregation in Mixed Halide Perovskites. *ACS Energy Letters* **3**, 204–213. eprint: <https://doi.org/10.1021/acsenerylett.7b01151>. <https://doi.org/10.1021/acsenerylett.7b01151> (2018).
58. Minns, J., Zajdel, P., Chernyshov, D., Van Beek, W & Green, M. Structure and interstitial iodide migration in hybrid perovskite methylammonium lead iodide. *Nature communications* **8**, 1–5 (2017).
59. Fu, F. *et al.* I₂ vapor-induced degradation of formamidinium lead iodide based perovskite solar cells under heat–light soaking conditions. en. *Energy & Environmental Science* **12**, 3074–3088. ISSN: 1754-5692, 1754-5706. <http://xlink.rsc.org/?DOI=C9EE02043H> (2021) (2019).
60. Weber, S. A. L. *et al.* How the formation of interfacial charge causes hysteresis in perovskite solar cells. *Energy Environ. Sci.* **11**, 2404–2413. <http://dx.doi.org/10.1039/C8EE01447G> (9 2018).
61. Quintero-Bermudez, R. *et al.* Compositional and orientational control in metal halide perovskites of reduced dimensionality. en. *Nature Materials* **17**, 900–907. ISSN: 1476-1122, 1476-4660. <http://www.nature.com/articles/s41563-018-0154-x> (2021) (Oct. 2018).
62. Aguiar, J. A. *et al.* In situ investigation of the formation and metastability of formamidinium lead tri-iodide perovskite solar cells. en. *Energy & Environmental Science* **9**, 2372–2382. ISSN: 1754-5692, 1754-5706. <http://xlink.rsc.org/?DOI=C6EE01079B> (2021) (2016).
63. Smith, I. C., Hoke, E. T., Solis-Ibarra, D., McGehee, M. D. & Karunadasa, H. I. A Layered Hybrid Perovskite Solar-Cell Absorber with Enhanced Moisture Stability. en. *Angewandte Chemie International Edition* **53**, 11232–11235. ISSN: 14337851. <https://onlinelibrary.wiley.com/doi/10.1002/anie.201406466> (2021) (Oct. 2014).
64. Lee, J.-W., Kim, H.-S. & Park, N.-G. Lewis Acid–Base Adduct Approach for High Efficiency Perovskite Solar Cells. en. *Accounts of Chemical Research* **49**, 311–319. ISSN: 0001-4842, 1520-4898. <https://pubs.acs.org/doi/10.1021/acs.accounts.5b00440> (2021) (Feb. 2016).
65. Jiang, Q. *et al.* Surface passivation of perovskite film for efficient solar cells. en. *Nature Photonics* **13**, 460–466. ISSN: 1749-4885, 1749-4893. <http://www.nature.com/articles/s41566-019-0398-2> (2021) (July 2019).
66. Min, H. *et al.* Efficient, stable solar cells by using inherent bandgap of α -phase formamidinium lead iodide. en. *Science* **366**, 749–753. ISSN: 0036-8075, 1095-9203. <https://www.sciencemag.org/lookup/doi/10.1126/science.aay7044> (2021) (Nov. 2019).
67. Bi, D. *et al.* Polymer-templated nucleation and crystal growth of perovskite films for solar cells with efficiency greater than 21%. en. *Nature Energy* **1**, 16142. ISSN: 2058-7546. <http://www.nature.com/articles/nenergy2016142> (2021) (Oct. 2016).

68. Bai, S. *et al.* Planar perovskite solar cells with long-term stability using ionic liquid additives. en. *Nature* **571**, 245–250. ISSN: 0028-0836, 1476-4687. <http://www.nature.com/articles/s41586-019-1357-2> (2021) (July 2019).
69. Turkevych, I. *et al.* Strategic advantages of reactive polyiodide melts for scalable perovskite photovoltaics. en. *Nature Nanotechnology* **14**, 57–63. ISSN: 1748-3387, 1748-3395. <http://www.nature.com/articles/s41565-018-0304-y> (2021) (Jan. 2019).
70. Jeon, N. J. *et al.* Solvent engineering for high-performance inorganic–organic hybrid perovskite solar cells. *Nat. Mater.* **13**, 897–903. ISSN: 1476-1122 (2014).
71. Lee, J.-W. *et al.* Formamidinium and Cesium Hybridization for Photo- and Moisture-Stable Perovskite Solar Cell. en. *Advanced Energy Materials* **5**, 1501310. ISSN: 16146832. <https://onlinelibrary.wiley.com/doi/10.1002/aenm.201501310> (2021) (Oct. 2015).
72. Kim, M. *et al.* Methylammonium Chloride Induces Intermediate Phase Stabilization for Efficient Perovskite Solar Cells. en. *Joule* **3**, 2179–2192. ISSN: 25424351. <https://linkinghub.elsevier.com/retrieve/pii/S2542435119303058> (2022) (Sept. 2019).
73. Dualeh, A. *et al.* Effect of Annealing Temperature on Film Morphology of Organic-Inorganic Hybrid Perovskite Solid-State Solar Cells. *Adv. Funct. Mater.* **24**, 3250–3258. ISSN: 1616301X (2014).
74. Lu, H. *et al.* Vapor-assisted deposition of highly efficient, stable black-phase FAPbI₃ perovskite solar cells. en. *Science* **370**, eabb8985. ISSN: 0036-8075, 1095-9203. <https://www.sciencemag.org/lookup/doi/10.1126/science.abb8985> (2021) (Oct. 2020).
75. Ummadisingu, A. *et al.* The effect of illumination on the formation of metal halide perovskite films. *Nature* **545**, 208–212. ISSN: 0028-0836 (2017).
76. Tsai, H. *et al.* Light-induced lattice expansion leads to high-efficiency perovskite solar cells. *Science* **360**, 67–70. ISSN: 1095-9203 (2018).
77. Hu, Q. *et al.* In situ dynamic observations of perovskite crystallisation and microstructure evolution intermediated from [PbI₆]⁴⁻ cage nanoparticles. en. *Nature Communications* **8**, 15688. ISSN: 2041-1723. <http://www.nature.com/articles/ncomms15688> (2021) (Aug. 2017).
78. Szostak, R. *et al.* Nanoscale mapping of chemical composition in organic-inorganic hybrid perovskite films. en. *Science Advances* **5**, eaaw6619. ISSN: 2375-2548. <https://advances.sciencemag.org/lookup/doi/10.1126/sciadv.aaw6619> (2021) (Oct. 2019).
79. Moore, D. T. *et al.* Crystallization Kinetics of Organic–Inorganic Trihalide Perovskites and the Role of the Lead Anion in Crystal Growth. *J. Am. Chem. Soc.* **137**, 2350–2358. ISSN: 0002-7863 (2015).
80. Manser, J. S., Reid, B. & Kamat, P. V. Evolution of Organic–Inorganic Lead Halide Perovskite from Solid-State Iodoplumbate Complexes. *J. Phys. Chem. C* **119**, 17065–17073. ISSN: 1932-7447 (2015).

81. Rahimnejad, S., Kovalenko, A., Forés, S. M., Aranda, C. & Guerrero, A. Coordination Chemistry Dictates the Structural Defects in Lead Halide Perovskites. *ChemPhysChem* **17**, 2795–2798. ISSN: 14394235 (2016).
82. Stewart, R. J., Grieco, C., Larsen, A. V., Doucette, G. S. & Asbury, J. B. Molecular Origins of Defects in Organohalide Perovskites and Their Influence on Charge Carrier Dynamics. *J. Phys. Chem. C* **120**, 12392–12402. ISSN: 1932-7447 (2016).
83. Manser, J. S., Reid, B. & Kamat, P. V. Evolution of Organic–Inorganic Lead Halide Perovskite from Solid-State Iodoplumbate Complexes. en. *The Journal of Physical Chemistry C* **119**, 17065–17073. ISSN: 1932-7447, 1932-7455. <https://pubs.acs.org/doi/10.1021/acs.jpcc.5b05898> (2021) (July 2015).
84. Yan, K. *et al.* Hybrid Halide Perovskite Solar Cell Precursors: Colloidal Chemistry and Coordination Engineering behind Device Processing for High Efficiency. *J. Am. Chem. Soc.* **137**, 4460–4468. ISSN: 0002-7863 (2015).
85. Nayak, P. K. *et al.* Mechanism for rapid growth of organic–inorganic halide perovskite crystals. en. *Nature Communications* **7**, 13303. ISSN: 2041-1723. <http://www.nature.com/articles/ncomms13303> (2021) (Dec. 2016).
86. Jo, Y. *et al.* High Performance of Planar Perovskite Solar Cells Produced from PbI_2 (DMSO) and PbI_2 (NMP) Complexes by Intramolecular Exchange. en. *Advanced Materials Interfaces* **3**, 1500768. ISSN: 21967350. <https://onlinelibrary.wiley.com/doi/10.1002/admi.201500768> (2021) (May 2016).
87. Guo, Y. *et al.* Chemical Pathways Connecting Lead(II) Iodide and Perovskite via Polymeric Plumbate(II) Fiber. en. *Journal of the American Chemical Society* **137**, 15907–15914. ISSN: 0002-7863, 1520-5126. <https://pubs.acs.org/doi/10.1021/jacs.5b10599> (2021) (Dec. 2015).
88. Xiao, S. *et al.* Unveiling a Key Intermediate in Solvent Vapor Postannealing to Enlarge Crystalline Domains of Organometal Halide Perovskite Films. en. *Advanced Functional Materials* **27**, 1604944. ISSN: 1616301X. <https://onlinelibrary.wiley.com/doi/10.1002/adfm.201604944> (2021) (Mar. 2017).
89. Bai, Y. *et al.* A pure and stable intermediate phase is key to growing aligned and vertically monolithic perovskite crystals for efficient PIN planar perovskite solar cells with high processibility and stability. en. *Nano Energy* **34**, 58–68. ISSN: 22112855. <https://linkinghub.elsevier.com/retrieve/pii/S2211285517300885> (2021) (Apr. 2017).
90. Petrov, A. A. *et al.* Crystal Structure of DMF-Intermediate Phases Uncovers the Link Between $\text{CH}_3\text{NH}_3\text{PbI}_3$ Morphology and Precursor Stoichiometry. en. *The Journal of Physical Chemistry C* **121**, 20739–20743. ISSN: 1932-7447, 1932-7455. <https://pubs.acs.org/doi/10.1021/acs.jpcc.7b08468> (2021) (Sept. 2017).
91. Pool, V. L. *et al.* Thermal engineering of FAPbI_3 perovskite material via radiative thermal annealing and in situ XRD. en. *Nature Communications* **8**, 14075. ISSN: 2041-1723. <http://www.nature.com/articles/ncomms14075> (2021) (Apr. 2017).

92. Meng, K. *et al.* In Situ Real-Time Study of the Dynamic Formation and Conversion Processes of Metal Halide Perovskite Films. en. *Advanced Materials* **30**, 1706401. ISSN: 09359648. <https://onlinelibrary.wiley.com/doi/10.1002/adma.201706401> (2021) (Mar. 2018).
93. Qin, M. *et al.* Manipulating the Mixed-Perovskite Crystallization Pathway Unveiled by In Situ GIWAXS. en. *Advanced Materials* **31**, 1901284. ISSN: 0935-9648, 1521-4095. <https://onlinelibrary.wiley.com/doi/10.1002/adma.201901284> (2021) (June 2019).
94. Kim, J. *et al.* Unveiling the Relationship between the Perovskite Precursor Solution and the Resulting Device Performance. en. *Journal of the American Chemical Society* **142**, 6251–6260. ISSN: 0002-7863, 1520-5126. <https://pubs.acs.org/doi/10.1021/jacs.0c00411> (2021) (Apr. 2020).
95. Szostak, R. *et al.* Exploring the formation of formamidinium-based hybrid perovskites by antisolvent methods: *in situ* GIWAXS measurements during spin coating. en. *Sustainable Energy & Fuels* **3**, 2287–2297. ISSN: 2398-4902. <http://xlink.rsc.org/?DOI=C9SE00306A> (2021) (2019).
96. Gratia, P. *et al.* The Many Faces of Mixed Ion Perovskites: Unraveling and Understanding the Crystallization Process. *ACS Energy Letters* **2**, 2686–2693. ISSN: 2380-8195. <http://pubs.acs.org/doi/10.1021/acsenergylett.7b00981> (2017).
97. Sanz, E. *et al.* Homogeneous Ice Nucleation at Moderate Supercooling from Molecular Simulation. en. *Journal of the American Chemical Society* **135**, 15008–15017. ISSN: 0002-7863, 1520-5126. <https://pubs.acs.org/doi/10.1021/ja4028814> (2022) (Oct. 2013).
98. Zimmermann, N. E. R., Vorselaars, B., Quigley, D. & Peters, B. Nucleation of NaCl from Aqueous Solution: Critical Sizes, Ion-Attachment Kinetics, and Rates. en. *Journal of the American Chemical Society* **137**, 13352–13361. ISSN: 0002-7863, 1520-5126. <https://pubs.acs.org/doi/10.1021/jacs.5b08098> (2022) (Oct. 2015).
99. Piana, S., Reyhani, M. & Gale, J. D. Simulating micrometre-scale crystal growth from solution. en. *Nature* **438**, 70–73. ISSN: 0028-0836, 1476-4687. <http://www.nature.com/articles/nature04173> (2022) (Nov. 2005).
100. Torrie, G. & Valleau, J. Nonphysical sampling distributions in Monte Carlo free-energy estimation: Umbrella sampling. en. *Journal of Computational Physics* **23**, 187–199. ISSN: 00219991. <https://linkinghub.elsevier.com/retrieve/pii/0021999177901218> (2022) (Feb. 1977).
101. Wolde, P. R. t. & Frenkel, D. Enhancement of Protein Crystal Nucleation by Critical Density Fluctuations. en. *Science* **277**, 1975–1978. ISSN: 0036-8075, 1095-9203. <https://www.science.org/doi/10.1126/science.277.5334.1975> (2022) (Sept. 1997).
102. Auer, S. & Frenkel, D. Prediction of absolute crystal-nucleation rate in hard-sphere colloids. en. *Nature* **409**, 1020–1023. ISSN: 0028-0836, 1476-4687. <http://www.nature.com/articles/35059035> (2022) (Feb. 2001).

103. Bolhuis, P. G., Chandler, D., Dellago, C. & Geissler, P. L. TRANSITION PATH SAMPLING: Throwing Ropes Over Rough Mountain Passes, in the Dark. en. *Annual Review of Physical Chemistry* **53**, 291–318. ISSN: 0066-426X, 1545-1593. <https://www.annualreviews.org/doi/10.1146/annurev.physchem.53.082301.113146> (2022) (Oct. 2002).
104. Lechner, W., Dellago, C. & Bolhuis, P. G. Role of the Prestructured Surface Cloud in Crystal Nucleation. en. *Physical Review Letters* **106**, 085701. ISSN: 0031-9007, 1079-7114. <https://link.aps.org/doi/10.1103/PhysRevLett.106.085701> (2022) (Feb. 2011).
105. Laio, A. & Parrinello, M. Escaping free-energy minima. *Proc. Natl. Acad. Sci. U. S. A.* **99**, 12562–6. ISSN: 0027-8424 (2002).
106. Wang, F. & Landau, D. P. Efficient, Multiple-Range Random Walk Algorithm to Calculate the Density of States. en. *Physical Review Letters* **86**, 2050–2053. ISSN: 0031-9007, 1079-7114. <https://link.aps.org/doi/10.1103/PhysRevLett.86.2050> (2022) (Mar. 2001).
107. Salvalaglio, M., Mazzotti, M. & Parrinello, M. Urea homogeneous nucleation mechanism is solvent dependent. *Faraday Discuss.* **179**, 291–307. ISSN: 1359-6640 (2015).
108. Zahn, D. Atomistic Mechanism of NaCl Nucleation from an Aqueous Solution. en. *Physical Review Letters* **92**, 040801. ISSN: 0031-9007, 1079-7114. <https://link.aps.org/doi/10.1103/PhysRevLett.92.040801> (2022) (Jan. 2004).
109. Chakraborty, D. & Patey, G. Evidence that crystal nucleation in aqueous NaCl solution Occurs by the two-step mechanism. en. *Chemical Physics Letters* **587**, 25–29. ISSN: 00092614. <https://linkinghub.elsevier.com/retrieve/pii/S000926141301227X> (2022) (Nov. 2013).
110. Lanaro, G. & Patey, G. N. Birth of NaCl Crystals: Insights from Molecular Simulations. en. *The Journal of Physical Chemistry B* **120**, 9076–9087. ISSN: 1520-6106, 1520-5207. <https://pubs.acs.org/doi/10.1021/acs.jpcc.6b05291> (2022) (Sept. 2016).
111. Jiang, H., Haji-Akbari, A., Debenedetti, P. G. & Panagiotopoulos, A. Z. Forward flux sampling calculation of homogeneous nucleation rates from aqueous NaCl solutions. en. *The Journal of Chemical Physics* **148**, 044505. ISSN: 0021-9606, 1089-7690. <http://aip.scitation.org/doi/10.1063/1.5016554> (2022) (Jan. 2018).
112. Raiteri, P. & Gale, J. D. Water Is the Key to Nonclassical Nucleation of Amorphous Calcium Carbonate. en. *Journal of the American Chemical Society* **132**, 17623–17634. ISSN: 0002-7863, 1520-5126. <https://pubs.acs.org/doi/10.1021/ja108508k> (2022) (Dec. 2010).
113. Shore, J. D., Perchak, D. & Shnidman, Y. Simulations of the nucleation of AgBr from solution. en. *The Journal of Chemical Physics* **113**, 6276–6284. ISSN: 0021-9606, 1089-7690. <http://aip.scitation.org/doi/10.1063/1.1308517> (2022) (Oct. 2000).
114. High-quality bulk hybrid perovskite single crystals within minutes by inverse temperature crystallization. *Nat. Commun.* **6**, 7586. ISSN: 2041-1723 (2015).

115. Heo, J. H. *et al.* Efficient inorganic–organic hybrid heterojunction solar cells containing perovskite compound and polymeric hole conductors. *Nat. Photonics* **7**, 486–491. ISSN: 1749-4885 (2013).
116. Kadro, J. M., Nonomura, K., Gachet, D., Grätzel, M. & Hagfeldt, A. Facile route to free-standing $\text{CH}_3\text{NH}_3\text{PbI}_3$ crystals using inverse solubility. *Sci. Rep.* **5**, 11654. ISSN: 2045-2322 (2015).
117. Zhang, F. *et al.* Colloidal Synthesis of Air-Stable $\text{CH}_3\text{NH}_3\text{PbI}_3$ Quantum Dots by Gaining Chemical Insight into the Solvent Effects. *Chem. Mater.* **29**, 3793–3799. ISSN: 0897-4756 (2017).
118. Salvalaglio, M., Perego, C., Giberti, F., Mazzotti, M. & Parrinello, M. Molecular-dynamics simulations of urea nucleation from aqueous solution. *Proc. Natl. Acad. Sci. U. S. A.* **112**, E6–14. ISSN: 1091-6490 (2015).
119. Humphrey, W., Dalke, A. & Schulten, K. VMD: Visual molecular dynamics. *J. Mol. Graph.* **14**, 33–38. ISSN: 0263-7855 (1996).
120. Ummadisingu, A. & Grätzel, M. Revealing the detailed path of sequential deposition for metal halide perovskite formation. *Science Advances* **4** (2018).
121. Ahn, N. *et al.* Highly Reproducible Perovskite Solar Cells with Average Efficiency of 18.3% and Best Efficiency of 19.7% Fabricated via Lewis Base Adduct of Lead(II) Iodide. *J. Am. Chem. Soc.* **137**, 8696–8699. ISSN: 0002-7863 (2015).
122. Li, B., Isikgor, F. H., Coskun, H. & Ouyang, J. The Effect of Methylammonium Iodide on the Supersaturation and Interfacial Energy of the Crystallization of Methylammonium Lead Triiodide Single Crystals. *Angewandte Chemie International Edition* **56**, 16073–16076 (2017).
123. Mattoni, A., Filippetti, A., Saba, M. I. & Delugas, P. Methylammonium Rotational Dynamics in Lead Halide Perovskite by Classical Molecular Dynamics: The Role of Temperature. *J. Phys. Chem. C* **119**, 17421–17428. ISSN: 1932-7447 (2015).
124. Wang, J., Wolf, R. M., Caldwell, J. W., Kollman, P. A. & Case, D. A. Development and testing of a general amber force field. *Journal of Computational Chemistry* **25**, 1157–1174 (2004).
125. Gutierrez-Sevillano, J. J., Ahmad, S., Calero, S. & Anta, J. A. Molecular dynamics simulations of organohalide perovskite precursors: solvent effects in the formation of perovskite solar cells. *Phys. Chem. Chem. Phys.* **17**, 22770–22777. ISSN: 1463-9076 (2015).
126. Ryckaert, J.-P., Ciccotti, G. & Berendsen, H. J. Numerical integration of the cartesian equations of motion of a system with constraints: molecular dynamics of n-alkanes. *J. Comput. Phys.* **23**, 327–341. ISSN: 0021-9991 (1977).
127. Plimpton, S. Fast Parallel Algorithms for Short-Range Molecular Dynamics. *J. Comput. Phys.* **117**, 1–19. ISSN: 0021-9991 (1995).
128. Bussi, G., Donadio, D. & Parrinello, M. Canonical sampling through velocity rescaling. *J. Chem. Phys.* **126**, 014101. ISSN: 0021-9606 (2007).

129. Parrinello, M. & Rahman, A. Polymorphic transitions in single crystals: A new molecular dynamics method. *J. Appl. Phys.* **52**, 7182–7190. ISSN: 0021-8979 (1981).
130. Tribello, G. A., Bonomi, M., Branduardi, D., Camilloni, C. & Bussi, G. PLUMED 2: New feathers for an old bird. *Comput. Phys. Commun.* **185**, 604–613. ISSN: 0010-4655 (2014).
131. Barducci, A., Bussi, G. & Parrinello, M. Well-Tempered Metadynamics: A Smoothly Converging and Tunable Free-Energy Method. *Phys. Rev. Lett.* **100**, 020603. ISSN: 0031-9007 (2008).
132. Tribello, G. A., Giberti, F., Sosso, G. C., Salvalaglio, M. & Parrinello, M. Analyzing and Driving Cluster Formation in Atomistic Simulations. *J. Chem. Theory Comput.* **13**, 1317–1327. ISSN: 1549-9618 (2017).
133. Park, N.-G. & Zhu, K. Scalable fabrication and coating methods for perovskite solar cells and solar modules. en. *Nature Reviews Materials* **5**, 333–350. ISSN: 2058-8437. <http://www.nature.com/articles/s41578-019-0176-2> (2021) (May 2020).
134. Park, N.-G. Green solvent for perovskite solar cell production. en. *Nature Sustainability* **4**, 192–193. ISSN: 2398-9629. <http://www.nature.com/articles/s41893-020-00647-6> (2021) (Mar. 2021).
135. Vidal, R. *et al.* Assessing health and environmental impacts of solvents for producing perovskite solar cells. en. *Nature Sustainability* **4**, 277–285. ISSN: 2398-9629. <http://www.nature.com/articles/s41893-020-00645-8> (2021) (Mar. 2021).
136. Frisch, M. J. *et al.* *Gaussian~16 Revision C.01* Gaussian Inc. Wallingford CT. 2016.
137. Becke, A. D. Density-functional thermochemistry. I. The effect of the exchange-only gradient correction. en. *The Journal of Chemical Physics* **96**, 2155–2160. ISSN: 0021-9606, 1089-7690. <http://aip.scitation.org/doi/10.1063/1.462066> (2021) (Feb. 1992).
138. Lee, C., Yang, W. & Parr, R. G. Development of the Colle-Salvetti correlation-energy formula into a functional of the electron density. *Phys. Rev. B* **37**, 785–789. <https://link.aps.org/doi/10.1103/PhysRevB.37.785> (2 1988).
139. Hay, P. J. & Wadt, W. R. *Ab initio* effective core potentials for molecular calculations. Potentials for the transition metal atoms Sc to Hg. en. *The Journal of Chemical Physics* **82**, 270–283. ISSN: 0021-9606, 1089-7690. <http://aip.scitation.org/doi/10.1063/1.448799> (2021) (Jan. 1985).
140. Hehre, W. J., Ditchfield, R. & Pople, J. A. Self—Consistent Molecular Orbital Methods. XII. Further Extensions of Gaussian—Type Basis Sets for Use in Molecular Orbital Studies of Organic Molecules. en. *The Journal of Chemical Physics* **56**, 2257–2261. ISSN: 0021-9606, 1089-7690. <http://aip.scitation.org/doi/10.1063/1.1677527> (2021) (Mar. 1972).
141. Perdew, J. P., Burke, K. & Ernzerhof, M. Generalized gradient approximation made simple. *Physical review letters* **77**, 3865 (1996).
142. Grimme, S. Semiempirical GGA-type density functional constructed with a long-range dispersion correction. *Journal of computational chemistry* **27**, 1787–1799 (2006).

143. VandeVondele, J. & Hutter, J. Gaussian basis sets for accurate calculations on molecular systems in gas and condensed phases. *The Journal of Chemical Physics* **127**, 114105. eprint: <https://doi.org/10.1063/1.2770708>. <https://doi.org/10.1063/1.2770708> (2007).
144. Goedecker, S., Teter, M. & Hutter, J. Separable dual-space Gaussian pseudopotentials. *Phys. Rev. B* **54**, 1703–1710. <https://link.aps.org/doi/10.1103/PhysRevB.54.1703> (3 1996).
145. VandeVondele, J. *et al.* Quickstep: Fast and accurate density functional calculations using a mixed Gaussian and plane waves approach. *Computer Physics Communications* **167**, 103–128. ISSN: 0010-4655. <https://www.sciencedirect.com/science/article/pii/S0010465505000615> (2005).
146. Hutter, J., Iannuzzi, M., Schiffmann, F. & VandeVondele, J. cp2k: Atomistic Simulations of Condensed Matter Systems: cp2k Simulation Software. en. *Wiley Interdisciplinary Reviews: Computational Molecular Science* **4**, 15–25. ISSN: 17590876. <https://onlinelibrary.wiley.com/doi/10.1002/wcms.1159> (2022) (Jan. 2014).
147. Nosé, S. A unified formulation of the constant temperature molecular dynamics methods. en. *The Journal of Chemical Physics* **81**, 511–519. ISSN: 0021-9606, 1089-7690. <http://aip.scitation.org/doi/10.1063/1.447334> (2021) (July 1984).
148. Hoover, W. G. Canonical dynamics: Equilibrium phase-space distributions. *Phys. Rev. A* **31**, 1695–1697. <https://link.aps.org/doi/10.1103/PhysRevA.31.1695> (3 1985).
149. Martyna, G. J., Klein, M. L. & Tuckerman, M. Nose-Hoover chains: The canonical ensemble via continuous dynamics. en. *The Journal of Chemical Physics* **97**, 2635–2643. ISSN: 0021-9606, 1089-7690. <http://aip.scitation.org/doi/10.1063/1.463940> (2021) (1992).
150. Martyna, G. J., Tobias, D. J. & Klein, M. L. Constant pressure molecular dynamics algorithms. en. *The Journal of Chemical Physics* **101**, 4177–4189. ISSN: 0021-9606, 1089-7690. <http://aip.scitation.org/doi/10.1063/1.467468> (2021) (1994).
151. Mączka, M. *et al.* Perovskite Metal Formate Framework of [NH₂-CH⁺-NH₂]Mn(HCOO)₃: Phase Transition, Magnetic, Dielectric, and Phonon Properties. en. *Inorganic Chemistry* **53**, 5260–5268. ISSN: 0020-1669, 1520-510X. <https://pubs.acs.org/doi/10.1021/ic500479e> (2021) (May 2014).
152. Kieslich, G., Sun, S. & Cheetham, A. K. An extended Tolerance Factor approach for organic–inorganic perovskites. en. *Chemical Science* **6**, 3430–3433. ISSN: 2041-6520, 2041-6539. <http://xlink.rsc.org/DOI=C5SC00961H> (2021) (2015).
153. Zhou, Z. *et al.* Synthesis, microwave spectra, x-ray structure, and high-level theoretical calculations for formamidinium formate. *The Journal of Chemical Physics* **150**, 094305. eprint: <https://doi.org/10.1063/1.5081683>. <https://doi.org/10.1063/1.5081683> (2019).
154. Petrov, A. A. *et al.* Formamidinium iodide: crystal structure and phase transitions. *Acta Crystallographica Section E Crystallographic Communications* **73**, 569–572. ISSN: 2056-9890. <http://scripts.iucr.org/cgi-bin/paper?S205698901700425X> (2021) (Apr. 2017).

155. Lanza, A. *et al.* Re-investigation of lead(II) formate. *Acta Crystallographica Section C Crystal Structure Communications* **69**, 41–43. ISSN: 0108-2701. <http://scripts.iucr.org/cgi-bin/paper?S010827011204913X> (2021) (Jan. 2013).
156. Giannozzi, P. *et al.* QUANTUM ESPRESSO: a modular and open-source software project for quantum simulations of materials. *Journal of Physics: Condensed Matter* **21**, 395502. ISSN: 0953-8984. <http://stacks.iop.org/0953-8984/21/i=39/a=395502?key=crossref.c21336c286fa6d3db893262ae3f6e151> (2009).
157. Jiang, Q. *et al.* Surface passivation of perovskite film for efficient solar cells. *Nature Photonics* **13**, 460–466. ISSN: 1749-4885. <http://www.nature.com/articles/s41566-019-0398-2> (2019).
158. Yang, W. S. *et al.* Iodide management in formamidinium-lead-halide-based perovskite layers for efficient solar cells. en. *Science* **356**, 1376–1379. ISSN: 0036-8075, 1095-9203. <https://www.science.org/doi/10.1126/science.aan2301> (2022) (June 2017).
159. Razza, S. *et al.* Perovskite solar cells and large area modules (100 cm²) based on an air flow-assisted PbI₂ blade coating deposition process. *Journal of Power Sources* **277**, 286–291 (2015).
160. Li, P. *et al.* Inkjet manipulated homogeneous large size perovskite grains for efficient and large-area perovskite solar cells. *Nano Energy* **46**, 203–211 (2018).
161. Park, N.-G. & Zhu, K. Scalable fabrication and coating methods for perovskite solar cells and solar modules. *Nature Reviews Materials*, 1–18 (2020).
162. Minemawari, H. *et al.* Inkjet printing of single-crystal films. *Nature* **475**, 364–367. ISSN: 0028-0836. <http://www.nature.com/articles/nature10313> (2011).
163. Bi, D. *et al.* Polymer-templated nucleation and crystal growth of perovskite films for solar cells with efficiency greater than 21%. *Nature Energy* **1**. ISSN: 20587546 (2016).
164. Brenner, T. M. *et al.* Conversion of single crystalline PbI₂ to CH₃NH₃PbI₃: Structural relations and transformation dynamics. *Chemistry of Materials* **28**, 6501–6510 (2016).
165. Guo, Y. *et al.* Chemical pathways connecting lead (II) iodide and perovskite via polymeric plumbate (II) fiber. *Journal of the American Chemical Society* **137**, 15907–15914 (2015).
166. Patel, J. B., Milot, R. L., Wright, A. D., Herz, L. M. & Johnston, M. B. Formation Dynamics of CH₃NH₃PbI₃ Perovskite Following Two-Step Layer Deposition. *Journal of Physical Chemistry Letters* **7**, 96–102. ISSN: 19487185 (2016).
167. Barrit, D. *et al.* Impact of the Solvation State of Lead Iodide on Its Two-Step Conversion to MAPbI₃: An In Situ Investigation. *Advanced Functional Materials* **29**, 1807544. eprint: <https://onlinelibrary.wiley.com/doi/pdf/10.1002/adfm.201807544>. <https://onlinelibrary.wiley.com/doi/abs/10.1002/adfm.201807544> (2019).
168. Sanches, A. W., Da Silva, M. A., Cordeiro, N. J., Urbano, A. & Lourenço, S. A. Effect of intermediate phases on the optical properties of PbI₂-rich CH₃NH₃PbI₃ organic-inorganic hybrid perovskite. *Physical Chemistry Chemical Physics* **21**, 5253–5261. ISSN: 14639076 (2019).

169. Liu, J. *et al.* High-Quality Mixed-Organic-Cation Perovskites from a Phase-Pure Non-stoichiometric Intermediate (FAI)_{1-x}PbI₂ for Solar Cells. *Advanced Materials* **27**, 4918–4923. ISSN: 15214095 (2015).
170. Xu, X. *et al.* Air-processed mixed-cation Cs_{0.15}FA_{0.85}PbI₃ planar perovskite solar cells derived from a PbI₂-CsI-FAI intermediate complex. *Journal of Materials Chemistry A* **6**, 7731–7740. ISSN: 20507496 (2018).
171. Sanchez, S., Steiner, U. & Hua, X. Phase Evolution during Perovskite Formation - Insight from Pair Distribution Function Analysis. *Chemistry of Materials* **31**, 3498–3506. ISSN: 15205002 (2019).
172. Pradeesh, K., Baumberg, J. J. & Prakash, G. V. In situ intercalation strategies for device-quality hybrid inorganic-organic self-assembled quantum wells. *Applied Physics Letters* **95**, 033309 (2009).
173. Jain, S. M. *et al.* Vapor phase conversion of PbI₂ to CH₃NH₃PbI₃: spectroscopic evidence for formation of an intermediate phase. *Journal of Materials Chemistry A* **4**, 2630–2642. ISSN: 2050-7488. <http://xlink.rsc.org/?DOI=C5TA08745G> (2016).
174. Que, C. J. *et al.* Perovskite-Like Organic-Inorganic Hybrid Lead Iodide with a Large Organic Cation Incorporated within the Layers. *Inorganic Chemistry* **56**, 2467–2472. ISSN: 1520510X (2017).
175. Kamminga, M. E., de Wijs, G. A., Havenith, R. W. A., Blake, G. R. & Palstra, T. T. The Role of Connectivity on Electronic Properties of Lead Iodide Perovskite-Derived Compounds. *Inorganic Chemistry* **56**, 8408–8414. ISSN: 0020-1669. <http://pubs.acs.org/doi/10.1021/acs.inorgchem.7b01096> (2017).
176. Lermer, C. *et al.* Completing the Picture of 2-(Aminomethylpyridinium) Lead Hybrid Perovskites: Insights into Structure, Conductivity Behavior, and Optical Properties. *Chemistry of Materials* **30**, 6289–6297. ISSN: 0897-4756. <http://pubs.acs.org/doi/10.1021/acs.chemmater.8b01840> (2018).
177. Stoumpos, C. C., Mao, L., Malliakas, C. D. & Kanatzidis, M. G. Structure–Band Gap Relationships in Hexagonal Polytypes and Low-Dimensional Structures of Hybrid Tin Iodide Perovskites. *Inorganic Chemistry* **56**, 56–73. ISSN: 0020-1669. <http://pubs.acs.org/doi/10.1021/acs.inorgchem.6b02764> (2017).
178. Noël, H & Padiou, J. Structure cristalline de FeUS₃. *Acta Crystallographica Section B: Structural Crystallography and Crystal Chemistry* **32**, 1593–1595 (1976).
179. Daub, M. & Hillebrecht, H. Tailoring the Band Gap in 3D Hybrid Perovskites by Substitution of the Organic Cations: (CH₃NH₃)_{1-2y}(NH₃(CH₂)₂NH₃)_{2y}Pb_{1-y}I₃ (0 ≤ y ≤ 0.25). *Chemistry – A European Journal* **24**, 9075–9082. eprint: <https://onlinelibrary.wiley.com/doi/pdf/10.1002/chem.201800244>. <https://onlinelibrary.wiley.com/doi/abs/10.1002/chem.201800244> (2018).

180. Warren, R. F. & Liang, W. Y. Raman spectroscopy of new lead iodide intercalation compounds. *Journal of Physics: Condensed Matter* **5**, 6407–6418. <https://doi.org/10.1088%2F0953-8984%2F5%2F35%2F006> (1993).
181. Pellegrino, G. *et al.* From PbI₂ to MAPbI₃ through Layered Intermediates. *The Journal of Physical Chemistry C* **120**, 19768–19777. ISSN: 1932-7447. <http://pubs.acs.org/doi/10.1021/acs.jpcc.6b03798> (2016).
182. Beckmann, P. A. A review of polytypism in lead iodide. *Crystal Research and Technology* **45**, 455–460. ISSN: 02321300. <http://doi.wiley.com/10.1002/crat.201000066> (2010).
183. Khilji, M. Y., Sherman, W. F. & Wilkinson, G. R. Raman study of three polytypes of PbI₂. *Journal of Raman Spectroscopy* **13**, 127–133. eprint: <https://onlinelibrary.wiley.com/doi/pdf/10.1002/jrs.1250130206>. <https://onlinelibrary.wiley.com/doi/abs/10.1002/jrs.1250130206> (1982).
184. Ahlawat, P. *et al.* A combined molecular dynamics and experimental study of two-step process enabling low-temperature formation of phase-pure -FAPbI₃. en. *Science Advances* **7**, eabe3326. ISSN: 2375-2548. <https://www.science.org/doi/10.1126/sciadv.abe3326> (2022) (Apr. 2021).
185. Zhang, T. *et al.* Spontaneous low-temperature crystallization of α -FAPbI₃ for highly efficient perovskite solar cells. *Science Bulletin* **64**, 1608–1616 (2019).
186. Dutta, N. S., Noel, N. K. & Arnold, C. B. The Crystalline Nature of Colloids in Methylammonium Lead Halide Perovskite Precursor Inks Revealed by Cryo-Electron Microscopy. *The Journal of Physical Chemistry Letters* (2020).
187. Coleman, C. *et al.* Intercalation of hydrazines in lead iodide. *Journal of Physics and Chemistry of Solids* **57**. Proceeding of the 8th International Symposium on Intercalation Compounds, 1153 –1158. ISSN: 0022-3697. <http://www.sciencedirect.com/science/article/pii/0022369795004149> (1996).
188. Caddeo, C., Saba, M. I., Meloni, S., Filippetti, A. & Mattoni, A. Collective Molecular Mechanisms in the CH₃NH₃PbI₃ Dissolution by Liquid Water. *ACS Nano* **11**, 9183–9190. ISSN: 1936-0851. <https://pubs.acs.org/doi/10.1021/acsnano.7b04116> (2017).
189. Ryckaert, J.-P., Ciccotti, G. & Berendsen, H. J. Numerical integration of the cartesian equations of motion of a system with constraints: molecular dynamics of n-alkanes. *Journal of Computational Physics* **23**, 327–341. ISSN: 0021-9991. <https://www.sciencedirect.com/science/article/pii/0021999177900985> (1977).
190. Niu, H., Piaggi, P. M., Invernizzi, M. & Parrinello, M. Molecular dynamics simulations of liquid silica crystallization. *Proceedings of the National Academy of Sciences of the United States of America* **115**, 5348–5352. ISSN: 10916490 (2018).
191. Debye, P. Zerstreuung von Röntgenstrahlen. *Annalen der Physik* **351**, 809–823. ISSN: 00033804. <http://doi.wiley.com/10.1002/andp.19153510606> (1915).
192. Ahlawat, P. *et al.* Atomistic Mechanism of the Nucleation of Methylammonium Lead Iodide Perovskite from Solution. *Chemistry of Materials* **32**, 529–536 (2019).

193. Oganov, A. R. & Ono, S. Theoretical and experimental evidence for a post-perovskite phase of MgSiO_3 in Earth's D" layer. *Nature* **430**, 445–448. ISSN: 0028-0836. <http://www.nature.com/articles/nature02701> (2004).
194. Li, Y. *et al.* A Perovskite Electrolyte That Is Stable in Moist Air for Lithium-Ion Batteries. *Angewandte Chemie International Edition* **57**, 8587–8591. ISSN: 14337851. <http://doi.wiley.com/10.1002/anie.201804114> (2018).
195. Alharbi, E. A. *et al.* Atomic-level passivation mechanism of ammonium salts enabling highly efficient perovskite solar cells. *Nature communications* **10**, 1–9 (2019).
196. Alharbi, E. A. *et al.* Perovskite solar cells yielding reproducible photovoltage of 1.20 V. *Research* **2019**, 8474698 (2019).
197. Lee, J.-W. *et al.* Formamidinium and cesium hybridization for photo- and moisture-stable perovskite solar cell. *Advanced Energy Materials* **5**, 1501310 (2015).
198. Saliba, M. *et al.* Incorporation of rubidium cations into perovskite solar cells improves photovoltaic performance. *Science* **354**, 206–209 (2016).
199. Abdi-Jalebi, M. *et al.* Maximizing and stabilizing luminescence from halide perovskites with potassium passivation. *Nature* **555**, 497–501 (2018).
200. McMeekin, D. P. *et al.* A mixed-cation lead mixed-halide perovskite absorber for tandem solar cells. *Science* **351**, 151–155 (2016).
201. Eperon, G. E. *et al.* Formamidinium lead trihalide: a broadly tunable perovskite for efficient planar heterojunction solar cells. *Energy & Environmental Science* **7**, 982–988 (2014).
202. Noh, J. H., Im, S. H., Heo, J. H., Mandal, T. N. & Seok, S. I. Chemical management for colorful, efficient, and stable inorganic–organic hybrid nanostructured solar cells. *Nano letters* **13**, 1764–1769 (2013).
203. Ono, L. K., Juarez-Perez, E. J. & Qi, Y. Progress on perovskite materials and solar cells with mixed cations and halide anions. *ACS applied materials & interfaces* **9**, 30197–30246 (2017).
204. Juarez-Perez, E. J., Hawash, Z., Raga, S. R., Ono, L. K. & Qi, Y. Thermal degradation of $\text{CH}_3\text{NH}_3\text{PbI}_3$ perovskite into NH_3 and CH_3I gases observed by coupled thermogravimetry–mass spectrometry analysis. en. *Energy & Environmental Science* **9**, 3406–3410. ISSN: 1754-5692, 1754-5706. <http://xlink.rsc.org/?DOI=C6EE02016J> (2022) (2016).
205. Lee, J.-W. *et al.* 2D perovskite stabilized phase-pure formamidinium perovskite solar cells. en. *Nature Communications* **9**, 3021. ISSN: 2041-1723. <http://www.nature.com/articles/s41467-018-05454-4> (2022) (Dec. 2018).
206. Fu, Y. *et al.* Stabilization of the Metastable Lead Iodide Perovskite Phase via Surface Functionalization. en. *Nano Letters* **17**, 4405–4414. ISSN: 1530-6984, 1530-6992. <https://pubs.acs.org/doi/10.1021/acs.nanolett.7b01500> (2022) (July 2017).

207. Cordero, F. *et al.* Influence of Temperature, Pressure, and Humidity on the Stabilities and Transition Kinetics of the Various Polymorphs of FAPbI₃. *The Journal of Physical Chemistry C* **124**, 22972–22980 (2020).
208. Cordero, F. *et al.* Stability of Cubic FAPbI₃ from X-ray Diffraction, Anelastic, and Dielectric Measurements. en. *The Journal of Physical Chemistry Letters* **10**, 2463–2469. ISSN: 1948-7185, 1948-7185. <https://pubs.acs.org/doi/10.1021/acs.jpclett.9b00896> (2022) (May 2019).
209. Lai, M. *et al.* Phase transition dynamics in one-dimensional halide perovskite crystals. *MRS Bulletin*, 1–7 (2021).
210. Hong, L. *et al.* Guanine-Stabilized Formamidinium Lead Iodide Perovskites. *Angewandte Chemie International Edition* **59**, 4691–4697. eprint: <https://onlinelibrary.wiley.com/doi/pdf/10.1002/anie.201912051>. <https://onlinelibrary.wiley.com/doi/abs/10.1002/anie.201912051> (2020).
211. Tesei, G., Aspelin, V. & Lund, M. Specific Cation Effects on SCN[−] in Bulk Solution and at the Air–Water Interface. *The Journal of Physical Chemistry B* **122**, 5094–5105 (2018).
212. Perdew, J. P. *et al.* Restoring the Density-Gradient Expansion for Exchange in Solids and Surfaces. *Phys. Rev. Lett.* **100**, 136406. <https://link.aps.org/doi/10.1103/PhysRevLett.100.136406> (13 2008).
213. Ruddlesden, S. N. & Popper, P. The compound Sr₃Ti₂O₇ and its structure. *Acta Crystallographica* **11**, 54–55. ISSN: 0365-110X. <http://scripts.iucr.org/cgi-bin/paper?S0365110X58000128> (2021) (Jan. 1958).
214. Dion, M., Ganne, M. & Tournoux, M. Nouvelles familles de phases MIMII₂Nb₃O₁₀ a feuillets “perovskites”. fr. *Materials Research Bulletin* **16**, 1429–1435. ISSN: 00255408. <https://linkinghub.elsevier.com/retrieve/pii/0025540881900635> (2021) (Nov. 1981).
215. Jacobson, A. J., Johnson, J. W. & Lewandowski, J. T. Interlayer chemistry between thick transition-metal oxide layers: synthesis and intercalation reactions of K[Ca₂Nan-3Nb_nO_{3n+1}] (3 .ltoreq. n .ltoreq. 7). en. *Inorganic Chemistry* **24**, 3727–3729. ISSN: 0020-1669, 1520-510X. <https://pubs.acs.org/doi/abs/10.1021/ic00217a006> (2021) (Nov. 1985).
216. Mitzi, D. B. Templating and structural engineering in organic–inorganic perovskites. *Journal of the Chemical Society, Dalton Transactions*, 1–12. ISSN: 14727773, 13645447. <http://xlink.rsc.org/?DOI=b007070j> (2021) (2001).
217. Gélvez-Rueda, M. C. *et al.* Formamidinium-Based Dion-Jacobson Layered Hybrid Perovskites: Structural Complexity and Optoelectronic Properties. *Advanced Functional Materials* **30**, 2003428 (2020).
218. Jahanbakhshi, F. *et al.* Unravelling the structural complexity and photophysical properties of adamantyl-based layered hybrid perovskites. *Journal of Materials Chemistry A* **8**, 17732–17740 (2020).

219. Hope, M. A. *et al.* Nanoscale Phase Segregation in Supramolecular π -Templating for Hybrid Perovskite Photovoltaics from NMR Crystallography. *Journal of the American Chemical Society* **143**, 1529–1538 (2021).
220. Du, K.-z. *et al.* Two-Dimensional Lead(II) Halide-Based Hybrid Perovskites Templated by Acene Alkylamines: Crystal Structures, Optical Properties, and Piezoelectricity. en. *Inorganic Chemistry* **56**, 9291–9302. ISSN: 0020-1669, 1520-510X. <https://pubs.acs.org/doi/10.1021/acs.inorgchem.7b01094> (2021) (Aug. 2017).

**Personal information:**

Nationality: India

OrcID: 0000-0003-2355-3663

Google Scholar ID: [gs_lib_7479173117442601281](https://scholar.google.com/citations?user=gs_lib_7479173117442601281)

Education:

Ph.D. studies, school of chemistry and chemical Engineering at EPFL, Switzerland 07/2016 – 02/2022

Computational Material Chemistry PhD studies with experience in atomistic simulations of crystallization, solid-solid phase transitions and surface chemistry of semi-conducting interfaces. Strong drive towards accurate simulations.

- Thesis: “Molecular dynamics simulations of nucleation and phase transitions in metal halide perovskites”
- Conducted research towards the main goal of understanding phase transition in halide perovskites, resulting in first author and collaborative published papers.
- Designed and performed simulations of homogeneous nucleation and seeded growth of perovskites.
- DFT simulations of solid-solid phase transitions and kinetic barrier calculations.
- Developing force fields of perovskite crystals and their solute-solvent clusters.
- Structure predictions of perovskites from a combined DFT and finite temperature MD simulations.
- Collaborations with Prof. Michael Graetzel, Prof. Anders Hagfeldt and Prof. Michele Parrinello

KTH Royal institute of technology, Stockholm, Sweden 09/2012 – 10/2014

- Master’s studies in chemical science and engineering,
- Thesis research conducted on chromatography at ETH Zurich, group of Prof. Massimo Morbidelli

National Institute of technology, Rourkela, India 05/2005 - 07/2009

- Bachelor of technology in chemical engineering

Employment history:

Process engineer at crude oil refinery, Essar oil, Jamnagar, India 09/2009 - 08/2012

- Team member for commissioning a new sulfur recover unit in oil refinery

Research assistant at KTH Stockholm, Group of Prof. Mathias Babler 11/2014 - 05/2015

- Conducted research on meso-scale simulations of turbulence

Prizes, awards, fellowships:

- Full tuition fee waiver for master’s studies at KTH Stockholm
- Erasmus Mundus scholarship to conduct master’s thesis at ETH Zurich
- Best poster award in conference "Mainz Materials Simulation Days 2019", at Max Plack Institute for Polymer Research.

Personal skills:

- Programming experience: C++, Fortran and Python
- Independent research skills: Encouraged to conceive research projects and publish
- Collaborations and communication skills: Working with different experimental groups around the world to prove theoretical findings with experiments and designing new simulation driven experimental techniques to make high efficiency and stable perovskite solar cells.

Career breaks:

USI Lugano, Switzerland

06/2015 – 03/2016

Research student in group of Prof. Michele Parrinello

- Conducted research to study crystal growth of Aspirin from solution

Contributions to conferences:

- Oral presentation, International conference on Hybrid and Organic Photovoltaics (HOPV), Rome, 02/2017
- Oral presentation, International conference on solar materials, nanoGE Fall Meeting, Berlin, 11/2019
- Poster presentation, Mainz Materials Simulation Days, Max Plack Institue for Polymer Research, Mainz, 06/2019
- Poster presentation, Molecular and materials simulation at the turn of the decade, Cecam 50 years of celebrations, Lausanne, 09/2019

Publications in peer-reviewed scientific journals in chronological order via importance:

1. **Paramvir Ahlawat**, Hinderhofer A, Alharbi EA, Lu H, Ummadisingu A, Niu H, Invernizzi M, Zakeeruddin SM, Dar MI, Schreiber F, Hagfeldt A., Graetzel M, Rothlisberger U, Parrinello M. A combined molecular dynamics and experimental study of two-step process enabling low-temperature formation of phase-pure α -FAPbI₃. *Science Advances*. 2021 Apr 1;7(17):eabe3326. doi.org/10.1126/sciadv.abe3326
2. **Paramvir Ahlawat**, Dar MI, Piaggi P, Graetzel M, Parrinello M, Rothlisberger U. Atomistic mechanism of the nucleation of methylammonium lead iodide perovskite from solution. *Chemistry of Materials*. 2019 Dec 19;32(1):529-36. doi.org/10.1021/acs.chemmater.9b04259
3. Lu H, Liu Y, **Paramvir Ahlawat**, Mishra A, Tress WR, Eickemeyer FT, Yang Y, Fu F, Wang Z, Avalos CE, Carlsen BI, Agarwalla A, Zhang X, Li X, Zhan Y, Zakeeruddin SM, Emsley L, Rothlisberger U, Zheng L, Hagfeldt A, Graetzel M. Vapor-assisted deposition of highly efficient, stable black-phase FAPbI₃ perovskite solar cells. *Science*. 2020 Oct 2;370(6512). doi.org/10.1126/science.abb8985
4. Jeong J, Kim M, Seo J, Lu H, **Paramvir Ahlawat**, Mishra A, Yang Y, Hope MA, Eickemeyer FT, Kim M, Yoon YJ, Choi IW, Darwich BP, Choi SJ, Jo Y, Lee JH, Walker B, Zakeeruddin SM, Emsley L, Rothlisberger U, Hagfeldt A, Kim DS, Graetzel M, Kim JY. Pseudo-halide anion engineering for α -FAPbI₃ perovskite solar cells. *Nature*. 2021 Apr;592(7854):381-5. doi.org/10.1038/s41586-021-03406-5
5. Hong L, Milic JV, **Paramvir Ahlawat**, Mladenovic M, Kubicki DJ, Jahanabkhshi F, Ren D, Gélvez-Rueda MC, Ruiz-Preciado MA, Ummadisingu A, Liu Y, Tian C, Pan L, Zakeeruddin SM, Hagfeldt A, Grozema FC, Rothlisberger U, Emsley L, Han H, Graetzel M. Guanine-Stabilized Formamidinium Lead Iodide Perovskites. *Angewandte Chemie International Edition*. 2020 Mar 16;59(12):4691-7. doi.org/10.1002/anie.201912051
6. Gélvez-Rueda MC*, **Paramvir Ahlawat***, Merten L*, Jahanbakhshi F, Mladenovic M, Hinderhofer A, Dar MI, Li Y, Ducinkas A, Carlsen B, Tress W., Ummadisingu A, Zakeeruddin SM, Schreiber F, Hagfeldt A, Rothlisberger U, Grozema FC, Milic JV, Graetzel M. Formamidinium-Based Dion-Jacobson Layered Hybrid Perovskites: Structural Complexity and Optoelectronic Properties. *Advanced Functional Materials*. 2020 Sep;30(38):2003428. doi.org/10.1002/adfm.202003428

7. Hope MA*, Nakamura T*, **Paramvir Ahlawat***, Mishra A*, Cordova M, Jahanbakhshi F, Mladenović M, Runjhun R, Merten L, Hinderhofer A, Carlsen BI, Kubicki DJ, Poranne RG, Schneeberger T, Carbone LC, Liu Y, Zakeeruddin SM, Lewinski J, Hagfeldt A, Schreiber F, Rothlisberger U, Graetzel M, Milic JV, Emsley M. Nanoscale Phase Segregation in Supramolecular π -Templating for Hybrid Perovskite Photovoltaics from NMR Crystallography. *Journal of the American Chemical Society*. 2021 Jan 14;143(3):1529-38 doi.org/10.1021/jacs.0c11563
8. Zhang H, Darabi K, Nia NY, Krishna A, **Paramvir Ahlawat**, Guo B, Almalki SM, Su TS, Bolnykh V, Castriotta L, Ren D, Zendejdel M, Pan L, Alonso S, Li R, Zakeeruddin S, Hagfeldt A, Rothlisberger U, Carlo AD, Amassian A, Graetzel M. A universal co-solvent dilution strategy enables facile, eco-friendly and cost-effective fabrication of perovskite photovoltaics. *Nature Communications* 13, 89 (2022). <https://doi.org/10.1038/s41467-021-27740-4>
9. Zhang H, Eickemeyer FT, Zhou Z, Mladenovic M, Jahanbakhshi F, Merten L, Hinderhofer A, Hope MA, Ouellette O, Mishra A, **Paramvir Ahlawat**, Ren D, Su TS, Krishna A, Wang Z, Dong Z, Guo J, Zakeeruddin SM, Schreiber F, Hagfeldt A, Emsley L, Rothlisberger U, Milic JV, Graetzel M Multimodal host–guest complexation for efficient and stable perovskite photovoltaics. *Nature communications*. 2021 Jun 7;12(1):1-1. doi.org/10.1038/s41467-021-23566-2
10. Jahanbakhshi F, Mladenović M, Kneschaurek E, Merten L, Gélvez-Rueda MC, **Paramvir Ahlawat**, Li Y, Dučinskas A, Hinderhofer A, Dar MI, Tress W, Carlsen B, Ummadisingu A, Zakeeruddin SM, Hagfeldt A, Schreiber F, Grozema FC, Rothlisberger U, Milic JV, Graetzel M. Unravelling the structural complexity and photophysical properties of adamantyl-based layered hybrid perovskites. *Journal of Materials Chemistry A*. 2020;8(34):17732-40. [10.1039/D0TA05022A](https://doi.org/10.1039/D0TA05022A)
11. Mishra A*, **Paramvir Ahlawat***, Fish G*, Jahanbakhshi F*, Mladenovic M, Almalki M, Ruiz-Preciado M, Gelvez-Rueda M, Kubicki D, Schouwink P, Dufoulon V, Schneeberger T, Aslanzadeh A, Grozema F, Zakeeruddin S, Moser JE, Rothlisberger U, Emsley L, Milic J, Graetzel M. Naphthalenediimide/ Formamidinium-Based Low-Dimensional Perovskites. *Chemistry of Materials* 2021, 33, 16, 6412–6420, <https://doi.org/10.1021/acs.chemmater.1c01635>
12. Alharbi EA, Krishna A, Baumeler T, Dankl M, Fish GC, Eickemeyer F, Ouellette O, **Paramvir Ahlawat**, Skorjanc V, Pfeifer L, Avalos CE, Yang B, Pan L, Mensi M, Schouwink PA, Moser JE, Hagfeldt A, Rothlisberger U, Zakeeruddin SM & Graetzel M. Methylammonium triiodide for holistic defect engineering of α -FAPbI₃ perovskite solar cells, *ACS Energy Letter* 2021, 6, 10, 3650–3660 <https://doi.org/10.1021/acsenergylett.1c01754>
13. Jahanbakhshi F, Mladenović M, Dankl M, Boziki A, **Paramvir Ahlawat**, Rothlisberger U. Organic Spacers in 2D Perovskites: General Trends and Structure-Property Relationships from Computational Studies. *Helvetica Chimica Acta*. 2021 Apr;104(4):e2000232. doi.org/10.1002/hlca.202000232

Outreach activities:

I have been constantly trying to propagate my research activities to the general public via scientific and general media personnel. Here I outline a few media stories:

- Low-temperature crystallization of phase-pure α -formamidinium lead iodide enabled by study: <https://nccr-marvel.ch/highlights/2021-05-LTC>, <https://www.eurekalert.org/news-releases/690427>, story covered by Carey Sargent, NCCR MARVEL, EPFL

- Molecular dynamics simulations play key role in manufacturing high efficiency solar cells: <https://www.cscs.ch/science/chemistry-materials/2020/molecular-dynamics-simulations/>, story covered by Simone Ulmer, ETH Zurich
- Computer simulations on piz-daint further boost efficiency of perovskite solar cells: <https://www.cscs.ch/science/chemistry-materials/2021/computer-simulations-on-piz-daint-further-boost-efficiency-of-perovskite-solar-cells/>, story covered by Simone Ulmer, ETH Zurich
- Molecular simulations contribute to the research on perovskite solar cells with world record efficiency: http://www.nccr-must.ch/highlights/jeong_542021.html , story covered by NCCR MUST